Nonlinear dynamics of exciton-polariton condensates

Xuekai Ma

(born on 06.03.1986, Hebei, China)

Department of Physics
Universität Paderborn

This dissertation is submitted for the degree of
Doctor rerum naturalium (Dr. rer. nat.)

April 2017

Promotionskommission

Vorsitzender: Prof. Dr. Thomas Zentgraf
Erstgutachter: Prof. Dr. Stefan Schumacher
Zweitgutachter: Prof. Dr. Torsten Meier
Beisitzer: Dr. Uwe Gerstmann

Submitted on April 19, 2017

To my wife Ping
and my daughter Lingxi (Isabella)

Abstract

Exciton-polaritons are quasiparticles that are found in semiconductor microcavities and are composed of quantum well excitons strongly coupled to cavity photons. These quasiparticles possess both photonic and excitonic nature. They have a small effective mass and short lifetime, both inherited from the photonic part. Through their excitonic part their interaction leads to an effective optical nonlinearity. Being composite bosons polaritons can undergo a condensation process, similar to Bose-Einstein condensation. Theoretically, in many aspects the dynamics of polariton condensates can be described by a Gross-Pitaevskii (GP) equation coupled to an incoherent reservoir.

The main aim of this thesis is to theoretically investigate the dynamics of polariton condensates in semiconductor microcavities under nonresonant (incoherent) excitation. First, in uniform semiconductor microcavities, modulational instability, spiraling waves, and vortices of condensates are studied under homogeneous excitation. The motion of vortices are turbulent due to their repulsion and attraction. However, an incoherent periodic pump is used to stabilize the turbulent vortices. This periodic pump also supports stable dark solitons, which can be created and annihilated by coherent pulses. Under localized ring-shaped pumps, crater-shaped vortices are found, while their rotation directions, the signs of topological charges, are uncertain due to noisy initial conditions. Two simpler methods are introduced for the vortex control: elliptical pump control and vortex-vortex control. One thing that they have in common is breaking the radial symmetry of the system such that the vortex charges can be controlled. Second, in nonuniform semiconductor microcavities with periodic potentials, a clear band-gap structure is observed. In weak-contrast lattices a simplified model, which has very good agreement with the full GP model, is developed. In tight-trapping lattices, collective state transitions of condensates are studied under narrow pumps. Under a broader pump a Talbot pattern is observed. Last, besides the dynamics of condensates in the scalar model, the dynamics of condensates in the spinor model are also studied considering the polarization effect. The binary condensates show both intra-species repulsion and cross-species interaction, resulting in the appearance of both defocusing and focusing nonlinearities in the polariton system. In a certain parameter range it is shown that the interplay of two nonlinearities supports stable symbiotic solitons and vortices.

Zusammenfassung

Als Exziton-Polaritonen bezeichnet man in Halbleitermikrokavitäten angeregte Quasiteilchen, bestehend aus Quantenfilm-Exzitonen, die stark an die Photonen innerhalb der Kavität gekoppelt sind. Diese Quasiteilchen sind von sowohl photonischer als auch exzitonischer Natur. Durch ihren photonischen Teil haben sie eine kleine effektive Masse und eine kurze Lebenszeit. Über ihren exzitonischen Teil führt ihre Wechselwirkung zu einer effektiven optischen Nichtlinearität. Als zusammengesetzte Bosonen können Polaritonen einen Kondensationsprozess erfahren, ähnlich einer Bose-Einstein-Kondensation. Die Dynamik der Polaritonkondensate kann in vielen Aspekten theoretisch durch eine Gross-Pitaevskii (GP) – Gleichung beschrieben werden, die zusätzlich an ein inkohärentes Reservoir gekoppelt ist.

Die theoretische Untersuchung dieser Dynamik unter nichtresonanter (inkohärenter) Anregung ist das Hauptziel dieser Arbeit. Hierbei werden in gleichförmigen Halbleitermikrokavitäten zuerst Modulationsinstabilität, spiralförmige Wellen und Wirbel von Kondensaten unter homogener Anregung untersucht. Die Bewegung der Wirbel ist durch ihre Abstoßung und Anziehung turbulent. Jedoch wird ein inkohärenter periodischer Pump verwendet, um die turbulenten Wirbel zu stabilisieren. Dieser periodische Pump unterstützt auch stabile dunkle Solitonen, die durch kohärente Impulse erzeugt und vernichtet werden können. Unter lokalisierten ringförmigen Pumpfeldern werden kraterförmige Wirbel gefunden, wobei ihre Rotationsrichtungen, die Vorzeichen ihrer topologischen Ladungen, aufgrund der zufälligen Anfangsbedingungen beliebig sind. Für die Wirbelkontrolle werden zwei einfachere Methoden eingeführt: Elliptische Pumpsteuerung und Wirbel-Wirbel-Steuerung. Beide führen zu einem Bruch der radialen Symmetrie des Systems, sodass die Wirbelladungen kontrolliert werden können. Zweitens wird bei ungleichförmigen Halbleiter-Mikrokavitäten mit periodischen Potentialen eine klare Bandlückenstruktur beobachtet. Bei schwach kontrastierenden Gittern wird ein vereinfachtes Modell entwickelt, das mit dem vollen GP-Modell sehr gut übereinstimmt. Bei starken Potentialgittern werden kollektive Zustandsübergänge von Kondensaten unter einem spektral schmalen Pump untersucht. Unter einem breiteren Pump wird ein Talbot-Muster beobachtet. Letztendlich wird neben der Dynamik der Kondensate im Skalarmodell auch die Dynamik von Kondensaten im Spinor-Modell unter Berücksichtigung der Polarisationseffekte untersucht. Die Binärkondensate zeigen sowohl eine Abstoßung von Polaritonen gleichen Spins als auch eine Wechselwirkung von verschiedener Spins, was zu dem Auftreten von fokussierender und defokussierender Nichtlinearitäten im Polaritonsystem führt. In einem bestimmten Parameterbereich wird gezeigt, dass das Zusammenspiel zweier Nichtlinearitäten stabile symbiotische Solitonen und Wirbel unterstützt.

Table of contents

Chapter 1

Introduction

Light-matter interaction has been widely studied in the recent decades. In a semiconductor an electron can be optically excited from the valence band to the conduction band leaving a positively charged "hole" in the valence band. The "escaped" electron still experiences attraction to the hole by the Coulomb force, forming a new bound state. This state is known as an exciton state, which is an electrically neutral quasiparticle. The term exciton was firstly coined by Frenkel in 1936 [1]. Frenkel excitons were widely studied in organic materials, and the binding energy of Frenkel excitons is typically of the order of 100-300 meV. Later, Wannier and Mott developed the concept of excitons in semiconductor crystals. Unlike Frenkel excitons, the Wannier-Mott excitons have a typical size of the order of tens of lattice constants and a small binding energy (a few meV). Therefore, the binding energy of excitons are strongly related to the materials.

In the mid-1950s, scientists found that the spectra of excitons are strongly influenced by optical excitation due to the coupling of excitons and light. The term "additional wave" was mentioned by the physicist Pekar when he studied the change of the exciton energy spectrum in 1957. The term "polariton" was then presented for the description of the exciton-photon coupling by Agranovich in 1957 [2]. To enhance the coupling of photons and excitons, one or more quantum wells (QWs), which are used to confine the motion of excitons in a plane (quasi 2D motion), are embedded in a planar semiconductor Fabry-Pérot microcavity with distributed Bragg reflectors (DBRs). The semiconductor microcavity can be fabricated by classical growth techniques. In such a semiconductor microcavity, in-plane excitons have more opportunity to interact with the near-resonant photons until they escape from the cavity. If the quality factor (Q-factor) of a microcavity is not too high, cavity photons escape from the cavity if they are absorbed and emitted only once by excitons. In other words, the photons leave the mirrors much faster than the typical reabsorption time by excitons, which is known as weak-coupling. In the weak-coupling regime, a low-threshold laser, the so-called

vertical-cavity surface-emitting laser (VCSEL), can be formed [3], and various technological application of the VCSELs have been found. In a high quality microcavity, photons can be confined in the cavity for a longer time, so that a emitted photon by an exciton can still stay in the cavity and be reabsorbed and re-emitted many times before leaving the structure, which is known as strong-coupling.

In the strong-coupling regime, the eigenmodes of the system are a combination of cavity photons and excitons, a mixed state. The quasi-particles are called "exciton-polaritons" or "polaritons" for short, and they exhibit a unique set of properties [4–7]. In 1992, the strong-coupling regime was first experimentally demonstrated by Weisbuch *et al* [8]. They found that the energy splitting, also known as the Rabi-splitting, leading to the formation of two polariton branches, the upper polariton branch (UPB) and the lower polariton branch (LPB). This property has been observed in different semiconductor materials in the following years. The Rabi-splitting of polaritons is related to the detuning of cavity photon modes and QW excitons. The detuning also influences the composition of polaritons around the center of the LPB. For positive detunings, where there are no crossing of the cavity photon mode and the exciton mode, polaritons are composed of a greater fraction of excitons, and therefore less photons. For negative detunings, one finds that the proportion of photons is more than half that of the excitons. For zero detuning, polaritons are composed of almost exactly half excitons and half photons. It is known that the UPB is more photonic with a parabolic dispersion curve, while the LPB is nonparabolic. This behaviour attracts more attentions for the investigation of polaritons in the lower branch.

The half-light half-matter property results in polaritons having a very small effective mass, about 10^{-4} of the free electron mass in vacuum, and a short lifetime, in the picosecond scale. The effective mass is strongly related to the photon-exciton detuning. When the detuning is more negative, or a polariton is more photon-like, the effective mass is smaller. Conversely, a polariton has larger effective mass if it is more exciton-like. The lifetime of polaritons dependents on the quality of the microcavity. A microcavity with high quality supports polaritons with lifetimes of several or tens of picoseconds [9–11], while a microcavity with extremely high quality ($Q \sim 320000$) results in polaritons with lifetimes which can be up to hundreds of picoseconds [12–15]. The thermalization time of more exciton-like polaritons is at least 40 ps, and even longer for the more photon-like polaritons [16]. Therefore, the polariton system can be in either thermal nonequilibrium or thermal equilibrium depending on their lifetime, that is, the quality of the microcavity.

The mixed quasiparticles have both photonic and excitonic nature. Due to the excitonic nature, polaritons repulsively interact with each other resulting in the strong defocusing nonlinearity, which leads to the polaritons exhibiting some interesting nonlinear phenomena.

Due to the photonic nature, polaritons can be excited by an optical beam, which can be either resonant or nonresonant, and probed by measuring the emitted photons.

Under resonant excitation, when the excitation pump has the same or similar frequency as the polaritons, a broad range of novel phenomena had been investigated and observed such as parametric scattering [17–21], bistability [22–26], superfluidity [27–29], vortices [30–34], and solitons [35–41]. One of the main aims in a nonlinear system is to find out the solitary solutions, *viz.*, solitons. Solitons have been widely studied in many physical systems including nonlinear optical systems [42–48], atomic condensates [49–55], superconductors [56–59], magnetic materials [60, 61], plasmas[62–65], and molecular systems [66–68], because they have potential applications in, for example, all-optical control, logic gate devices, information transmission. It is known that bright solitons can exist if the system shows focusing nonlinearity; in contrast, defocusing nonlinearity supports the existence of dark solitons. However, in polariton systems exhibiting defocusing nonlinearity, bright solitons were also found theoretically and experimentally due to the non-parabolic dispersion of the LPB [36, 40]. In the bottleneck region of the LPB, polaritons have negative effective mass and defocusing nonlinearity, which can be qualitatively regarded as being similar to a system with positive effective mass and focusing nonlinearity. The bottleneck region has finite momentum which results in the in-plane moving of bright solitons. Another important nonlinear phenomenon is the bistability. Bistability means that two possible stable states and is useful for optical logic devices. Under resonant excitation the bistability of polaritons were studied. This kind of bistability shows a S-shape relation between the population of polaritons and the pump intensity [22]. One can obtain the bistable states by increasing the pump from a smaller intensity or decreasing the pump from a larger intensity to the bistability region. Furthermore, an additional coherent pulse can be used for switching between them. For different parameters there also exist instability in polariton systems. Under homogeneous excitation, modulated patterns were found due to the instability [69, 70]. The profiles of those patterns depend strongly on the detuning of the pump frequency from the system's resonances, and the instability region appears always in the middle of the existence of homogeneous solutions. For a localized coherent pump with a finite momentum, superfluidity was observed theoretically and experimentally when the pump intensity is above some threshold. Due to the existence of defects and polariton flow, vortex and antivortex pairs were observed in polariton superfluids.

Bosonic polaritons can also be excited by nonresonant (incoherent) pumps with the frequencies far above the excitonic resonance. Under the nonresonant excitation, excitons are pumped to the higher unstable energy states through heating mechanism. They then relax very quickly to the upper and lower polariton branches through the emission of phonons.

At cryogenic temperatures, polaritons in the higher energy levels are unstable, leading to a situation where most of the polaritons occupy the LPB in the vicinity of the bottleneck region. In this region, two polaritons interact with each other, with one of them jumping to the ground ($k = 0$) state and the other one jumping to the higher state with larger momentum because of the conservation of momentum. Meanwhile, the carriers in the bottleneck region form an exciton reservoir providing the direct source for polaritons in the ground state. Besides the gain of polaritons from the reservoir excitons, polaritons in the ground state spontaneously decay in a short time due to the recombination of excitons and emit coherent photons. When the gain is larger than the decay, massive coherent polaritons occupy the ground state undergoing Bose-Einstein condensation (BEC) [71–74]. The polariton BEC had been achieved at low temperatures (~ 10 K) in several semiconductor materials such as GaAs and CdTe. Unlike the conventional BECs of cold atom or liquid helium, the nonequilibrium polariton BEC can even achieve room temperature condensation if the excitons have very large binding energy such as in GaN, ZnO, and organic semiconductors [75–84]. The polariton BEC can be used to design a polariton laser because of the fact that during the excitation a large amount coherent photons are emitted and escape from the microcavity due to the finite lifetime of polaritons [85–87]. The polariton laser is different from conventional semiconductor lasers. They do not need the population inversion of particles, which results in the polariton laser having a lower threshold.

In the past decade, scientists paid a lot of attention to the investigation of the dynamics of polariton condensates in semiconductor microcavities excited by incoherent pumps [88], mainly in the nonequilibrium case, when the polariton lifetime is shorter than 10 ps. The study showed that an incoherent pump creates an incoherent reservoir which, on the one hand, provides the direct source of polariton condensates. On the other hand, the distribution of reservoir excitons, like a potential, strongly influences the distribution of polariton condensates. These reservoir-created potentials, or optically induced potentials, have been exploited to a large extent for the realization of various trapping geometries. Under one-spot pumps, condensates localize in the reservoir region forming a fundamental mode with energy flowing from the center to the surroundings [89]. A two-spot pump can create a quasi-one-dimensional parabolic potential supporting spontaneous quantum oscillations of polariton condensates (the simple harmonic oscillator state) [90]. It was also noted that when two or more fundamental modes of polariton condensates are close to each other they become a phase-locked state with the phase difference of 0 or π depending on both the separation distance and outflow velocity of condensates [91]. This for example can be exploited in polariton simulators [92].

When the pump includes more spots, a phase-locked state is formed due to the 2D confinement [93]. This also happens under ring-shaped pumps where a 2D parabolic reservoir-created potential is generated. The 2D ring-shaped potential can confine all condensates inside the ring forming a localized fundamental mode [94]. Moreover, a precise adjustment of the polariton condensate flow under incoherent excitation condition has been demonstrated [95]. It turned out that both the steady-state and condensate flow directions can be controlled by means of optically induced potentials which are naturally realized under nonresonant pumping.

It is worth noting that vortices, or phase singularities, were observed and studied in polariton condensates due to the circular energy flow of polaritons. Phase singularities, corresponding to dark solitons in the 1D case and vortices in the 2D case, have been studied in many physical systems including superconductors [96–100], magnetic system [101–105], atomic condensates [49, 50, 106–110], and nonlinear optical systems [111–117]. In the past decade there was remarkable progress in the study of vortices in polariton condensates. In polariton condensates vortices can be roughly classified into two types: cyclone-like vortices and crater-like vortices. Cyclone-like vortices are mainly generated by broader pumps [118–122] due to the thermal fluctuation of the polaritons during excitation. This type of vortex has a cyclone profile in density and a 2π dislocation in phase. Generally, these vortices are formed spontaneously and randomly due to the initial phase defects, so that their location and number are uncertain. Crater-like vortices can be created by a ring-shaped pump [123] or a pump with circled intensity [124]. These pumps generate a 2D parabolically optical induced potential, which limits the condensates having a ring-shaped density and phase dislocation in the center of the density ring. These vortices are not very sensitive to noise and their location are determined by the pumps. However, the sign of the topological charge is uncertain due to the initial noise and the radial symmetry of the system. To break the radial symmetry, that is, to control the rotation directions of vortices, several methods were introduced in previous studies, such as by chiral polaritonic lenses [124] and external potentials [123]. The 1D phase defects, or dark solitons, under homogeneous excitation are unstable and can only persist for short times. They then disappear as the system transitions into the stable homogeneous phase in 1D [125]. In 2D, unstable dark solitons split up into several vortex-antivortex pairs [126].

It is known that a free propagating particle can be trapped into a special state by an external potential which influences the dynamics of the particle. In matter waves, periodic potentials were suggested to study their dynamics in the conventional BEC [127–131], which offers an opportunity to build quantum simulators and quantum information processing system. A variety of fabrication techniques of periodic potentials in microcavity semiconductors

had been introduced such as reaction ion etching [11], mirror thickness variation [132], stress application [73], metal surface deposition [133–135], surface acoustical wave modulation [136, 137], deep etching of micropillars [138], local application of crystal strain [73], deposition of semiconductor microrods on a silicon grating [139], or the microstructuring of buried mesa traps [140]. Due to different techniques, potential depth can range from hundreds of μeV to several meV. Generally speaking, the kinetic energy of a free polariton is around 1 meV. When a potential depth is weaker than the kinetic energy of free polaritons, the band-gap structure cannot be observed in the photoluminescence spectra when the pump intensity is below the condensation threshold. For larger pump intensity, however, polaritons spontaneously condensate at in-phase (zero-momentum) and anti-phase (π-momentum) states [133].

In the tight-trapping periodic potentials, a band-gap structure was observed [140]. The band structure in other geometric distribution of potentials is also studied [135, 141] including the graphene-like band spectra (including Dirac cones) [134, 138]. A gap soliton state is formed when the pump intensity is above the threshold because of the nonlinearity induced blue shift [137, 142]. Formation and fragmentation of the condensates into an array of wires moving with the surface acoustic waves had been observed [136]. The existence of novel spatially localized states of coherent polariton condensates in semiconductor microcavities with fabricated periodic in-plane potentials has been predicted [143].

In general, the natural interaction in the underlying physical system are repulsive, hence they do not support regular bright solitons, although it is possible to generate moving solitons and gap solitons in repulsive polariton condensates as mentioned above. The overall interaction, however, may be switched into attraction due to a Feshbach resonance in spinor atomic condensates [144–147]. The Feshbach resonance applies to the inter-component interaction in spinor (or pseudo-spinor) condensates, which induces attractive interaction between them [148, 149], while each component still features self-repulsion. The attraction between the two components can overcome the intrinsic repulsion and support symbiotic solitons [150, 151].

Polaritons possess an internal degree of freedom due to the polarization effect, which is called 'pseudospin', which has two possible projections on the structural growth axis of the microcavity, analogous to the spin of electrons. They inherit the spin from QW excitons and cavity photons. Of note is that the longitudinal exciton is coupled with the transverse magnetically (TM) polarised cavity photon mode, while the transverse exciton is coupled with the transverse electrically (TE) polarised cavity photon mode. The energy splitting of TE and TM light polarizations leads to the observation of the TE-TM splitting of polaritons [152–154]. In the spinor case, the optical spin Hall effect [155, 156] and the spin switching [157] in

polaritons have been observed and studied. The two spin components of polariton condensates also shows attractive interaction by means of a Feshbach resonance [158–160], which leads to the existence of focusing nonlinearity in the polariton system. In a narrow spectral range, close to the two-particle resonance associated with the formation of a bound biexciton state, the role of the attractive cross-component interaction can be finely tuned so that it may dominate over the repulsive inter-component interaction.

Theoretically, the dynamics of polaritons under coherent excitation can be described by two coupled equations denoting photonic component and excitonic component, respectively [36, 28, 40]. Under incoherent excitation, however, a simple mean-field Gross-Pitaevskii equation (GPE) coupled with an incoherent reservoir density [161, 162] is widely used for the study of polariton condensates in the LPB [119, 121, 122, 156, 143]. It has been proven that in many aspects the GP approach has good agreement with the experiments in both scalar [119, 121, 122] and spinor [156, 163] cases, as well as including external potentials [142].

1.1 Aim and structure of this theses

Before this thesis, there were still some questions on the dynamics of polariton condensates under incoherent excitation that needed to be solved in order to understand the whole picture of the polariton system. For example, the dynamics of condensates under homogeneous excitation, including modulational instability, theoretical study of vortices and their topological control, detailed theoretical investigation of condensates in periodic potentials, and the solutions of binary condensates concerning the attractive cross-species interaction.

To answer these questions, based on the GPE, we firstly investigate the excitation dynamics of polariton condensates in uniform semiconductor microcavities using different pumps, including homogeneous and localized pumps. It is known that under coherent homogeneous excitation a modulated pattern is formed due to the instability [69]. It is worth determining whether the modulational instability exists under incoherent homogeneous excitation. Experimental observations showed the existence of stable vortex-antivortex pairs under a ring-shaped (localized) pump. Therefore, it is necessary to investigate theoretically the dynamics of vortices under ring-shaped pumps and other localized modes. Moreover, to realize incoherent control of topological charges of vortices is very important since the manipulation of the binary topological states opens the possibility of a new type of information processing using vortices as topologically protected memory components. Furthermore, incoherent control of vortices is easier than coherent control because a wide range of frequency can be chosen for the control pump. The bright and dark solitons under coherent excitation are stable [35, 36].

It will be incredibly useful to find stable solitons under incoherent pumps, because dark solitons are demonstrably unstable and transit into the stable homogeneous solution in the 1D case. In the 2D case unstable dark solitons split up into several vortex-antivortex pairs.

The second main aim of this theses is to theoretically investigate the dynamics of condensates loaded into periodic potentials. Several experimental groups observed and studied the band-gap structure and the formation of coherence for polaritons in different energy bands. The theoretical investigation, however, was very limited so that some experimental findings cannot be perfectly explained. Therefore, it is worth theoretically studying the influence of different lattices, including weak-contrast and tight-trapping potentials, on the dynamics of condensates. The theoretical investigation can be used, on the one hand, to understand the fundamental properties of polariton condensates and explain the experimental observation. On the other hand, the study is useful for resulting further novel properties of polaritons and designing polaritonic devices.

In the polariton system there also exists attractive interaction between the two components of condensates if considering the polarization (spin) effect [158–160]. This property is promising for the existence of stable bright solitons in polariton condensates. The third aim of this theses is to find symbiotic solitons in binary condensates with repulsive intra-species and attractive cross-species interactions. This will open a way to investigate the dynamics of polaritons under both focusing and defocusing nonlinearities.

This thesis is composed of four main parts. The first part, Chapter 2, is the theoretical derivation of the equations of motion of polaritons and the GPE. In the second part, containing Chapter 3 and Chapter 4, we investigate the excitation dynamics of polaritons in uniform semiconductor microcavities under different pump profiles. In Chapter 3, we concentrate in detail on the dynamics of condensates under homogeneous and periodic pumps to study the phase defects, dark solitons in 1D and vortices in 2D. The excitation under localized pumps are presented in Chapter 4, where steady state vortices are created by ring-shaped pumps, and two methods are found to control the topological charges of vortices. In the third part, we consider nonuniform semiconductor microcavities containing periodic potentials, which is presented in Chapter 5. The dynamics of polaritons in both weaker and stronger periodic potentials are studied in this section. In the last part of this thesis, Chapter 6, we consider the spin effect of condensates with cubic attraction between the two components and intra-species repulsion. In this part, the steady-state solutions, symbiotic solitons and vortices, are addressed.

Chapter 2

Theoretical model

As introduced in Chapter 1, many theoretical and experimental results have shown that the dynamics of polariton condensates can be described by the GPE under the mean-field approximation and a coupled equation to the reservoir. In this chapter, we start from Maxwell's macroscopic equations and the definitions of the auxiliary fields for the approximate derivation of the GPE in semiconductor microcavities. Microcavity polaritons are made of QW excitons strongly coupled to cavity photons, and the strong coupling generates two anticrossing dispersion branches, the LPB and the UPB. The LPB is nonparabolic, suffering a sudden drop around the center of the zero momentum region. The Rabi-splitting of the two branches are related to the detuning of the cavity photon mode and the QW exciton mode. For positive detunings the center of the LPB is shallow and the polaritons are more excitonic, while for negative detuning the LPB is sharper and the corresponding polaritons are more photonic. For zero detuning the polaritons at the LPB are composed of almost exactly half excitons and half photons. Using Maxwell's equations, under coherent excitation the dynamics of polaritons can be written into two coupled equations describing the photonic and excitonic components. Under nonresonant excitation and with the pump frequency far above the excitonic resonance, excitons are heated to higher unstable states and relax very fast to the lower energy states at cryogenic temperatures. At this point, almost all of the polaritons condense to the ground state of the lower branch by scattering, forming spontaneous macroscopic quantum coherence. The dynamics of polariton condensates in the vicinity of the bottom of the lower polariton branch can be described by a widely accepted GPE including a coupling term with an incoherent reservoir. The reservoir is the source of coherent condensates. The reservoir-condensate interaction provides a defocusing nonlinearity together with condensate-condensate interactions. The density of the reservoir is time-dependent and directly excited by an incoherent pump. The parameters in the GPE are determined by the semiconductor materials and the structure of the cavities.

2.1 Equations of motion of exciton-polaritons

It is known that the propagation of an electromagnetic wave can be described by Maxwell's equations. To theoretically investigate the dynamics of polaritons in the semiconductor microcavity we seek two coupled equations describing their photonic and excitonic components, respectively. The equations of motion for the photonic component of polaritons starts from Maxwell's equations in matter, or Maxwell's macroscopic equations,

$$\nabla \times \mathbf{E}(\mathbf{r},t) = -\frac{\partial \mathbf{B}(\mathbf{r},t)}{\partial t}, \quad \nabla \times \mathbf{H}(\mathbf{r},t) = \mathbf{J}_f + \frac{\partial \mathbf{D}(\mathbf{r},t)}{\partial t}, \tag{2.1}$$

where $\mathbf{E}(\mathbf{r},t)$ is the electric field, $\mathbf{B}(\mathbf{r},t)$ is the magnetic field, $\mathbf{H}(\mathbf{r},t)$ is the magnetizing field, $\mathbf{D}(\mathbf{r},t)$ is the displacement field, and $\mathbf{J}_f$ is the free current density. In a semiconductor microcavity there is no free current, with $\mathbf{J}_f = 0$. According to Eq. (2.1), one can obtain

$$\nabla \times (\nabla \times \mathbf{E}(\mathbf{r},t)) = -\frac{\partial}{\partial t}(\nabla \times \mathbf{B}(\mathbf{r},t)). \tag{2.2}$$

Under the polarization of an optical beam, the electric displacement in a cavity reads [164]

$$\mathbf{D}(\mathbf{r},t) = \varepsilon_0 n_s^2 \mathbf{E}(\mathbf{r},t) - \hbar t_c \mathbf{E}_{\text{cav}}(x,y,t)\delta(z), \tag{2.3}$$

where ε_0 is the vacuum permittivity, n_s is the refractive index of the substrate out of the cavity, $\mathbf{E}(\mathbf{r},t)$ represents the light field, including incident, reflected, and transmitted waves, outside the cavity, $\mathbf{E}_{\text{cav}}(x,y,t)$ represents the cavity field confined in an infinitely thin plane, t_c is the coupling strength of the cavity field and the light field out of the cavity. The function $\delta(z)$ denotes that the cavity is infinitely thin and placed at $z = 0$. Applying the following constitutive relation

$$\mathbf{H}(\mathbf{r},t) = \frac{1}{\mu_0}\mathbf{B}(\mathbf{r},t), \tag{2.4}$$

where μ_0 is the magnetic permeability in vacuum, a wave propagation equation for the electric field radiation $\mathbf{E}(\mathbf{r},t)$ is obtained

$$\nabla(\nabla \cdot \mathbf{E}(\mathbf{r},t)) - \nabla^2 \mathbf{E}(\mathbf{r},t) = -\mu_0 \varepsilon_0 n_s^2 \frac{\partial^2 \mathbf{E}(\mathbf{r},t)}{\partial t^2} + \mu_0 \hbar t_c \frac{\partial^2 \mathbf{E}_{\text{cav}}(x,y,t)}{\partial t^2}\delta(z). \tag{2.5}$$

The total current density is zero resulting in $\nabla \cdot \mathbf{E}(\mathbf{r},t) = 0$. Replacing $\varepsilon_0 \mu_0$ by $1/c^2$, one obtains

$$\frac{n_s^2}{c^2}\frac{\partial^2 \mathbf{E}(\mathbf{r},t)}{\partial t^2} - \nabla^2 \mathbf{E}(\mathbf{r},t) = \frac{\hbar t_c}{\varepsilon_0 c^2}\frac{\partial^2 \mathbf{E}_{\text{cav}}(x,y,t)}{\partial t^2}\delta(z). \tag{2.6}$$

Transferring the electric fields $\mathbf{E}(\mathbf{r},t)$ and $\mathbf{E}_{\text{cav}}(x,y,t)$ from real space to momentum space by Fourier transform, namely, $E_{\mathbf{k}}$ and $E_{\mathbf{k},\text{eff}}$, respectively, and neglecting the coupling to QW excitons, the equation of motion of the cavity field now reads [164–166]

$$i\hbar\frac{\partial}{\partial t}E_{\mathbf{k}} = \hbar\omega_k^c E_{\mathbf{k}} + \hbar t_c E_{\mathbf{k},\text{eff}}, \tag{2.7}$$

where the energy $\hbar\omega_k^c \simeq \hbar\omega_0^c + \frac{\hbar^2 k^2}{2m_c}$. The relations between the incident $E_{\mathbf{k},\text{inc}}$, reflected $E_{\mathbf{k},\text{refl}}$, and transmitted $E_{\mathbf{k},\text{trans}}$ light fields in the momentum space satisfy [164]

$$E_{\mathbf{k},\text{eff}} = E_{\mathbf{k},\text{inc}} - E_{\mathbf{k},\text{refl}}, \tag{2.8}$$

$$E_{\mathbf{k},\text{refl}} = -\frac{\hbar t_c}{2\varepsilon_0 c n_c}\frac{\partial}{\partial t}E_{\mathbf{k}}. \tag{2.9}$$

We assume that the electric field involves a slowly varying envelope, so that $\frac{\partial}{\partial t}E_{\mathbf{k}} \simeq -i\omega_p E_{\mathbf{k}}$, where ω_p is the eigenfrequency. Substituting Eqs. (2.8) and (2.9) into Eq. (2.7), one can obtain

$$i\hbar\frac{\partial}{\partial t}E_{\mathbf{k}} = (\hbar\omega_k^c - i\gamma_{ph})E_{\mathbf{k}} + E_{\mathbf{k},\text{pump}}, \tag{2.10}$$

where $\gamma_{ph} = \frac{\hbar^2 t_c^2 \omega_p}{2\varepsilon_0 c n_c}$ represents the loss rate and $E_{\mathbf{k},\text{pump}} = \hbar t_c E_{\mathbf{k},\text{inc}}$ represents the pump field.

Considering the coupling of the cavity photon modes and the QW exciton mode, a coupling term should be included into Eqs. (2.10) [164] as

$$i\hbar\frac{\partial}{\partial t}E_{\mathbf{k}} = (\hbar\omega_k^c - i\gamma_{ph})E_{\mathbf{k}} - \Omega_R p_{\mathbf{k}} + E_{\mathbf{k},\text{pump}}, \tag{2.11}$$

where $p_{\mathbf{k}}$ is the exciton field with the exciton density $|p_{\mathbf{k}}|^2$ in momentum space and the Rabi frequency Ω_R represents the coupling strength. To deduce the equation of motion of excitons in a 2D QW coupled to an external electromagnetic field, the Hamiltonian of the many-particle system reads [158, 167]

$$\begin{aligned}
H =& H_1 + H_2 + H_{\text{field}} \\
=& \sum_{\mathbf{k}}\varepsilon_v(\mathbf{k})v_{\mathbf{k}}^\dagger v_{\mathbf{k}} + \sum_{\mathbf{k}}\varepsilon_c(\mathbf{k})c_{\mathbf{k}}^\dagger c_{\mathbf{k}} \\
&+ \frac{1}{2}\sum_{\mathbf{k},\mathbf{k}',\mathbf{q}\neq 0}V_{\mathbf{q}}\left(v_{\mathbf{k}+\mathbf{q}}^\dagger v_{\mathbf{k}'-\mathbf{q}}^\dagger v_{\mathbf{k}'}v_{\mathbf{k}} + c_{\mathbf{k}+\mathbf{q}}^\dagger c_{\mathbf{k}'-\mathbf{q}}^\dagger c_{\mathbf{k}'}c_{\mathbf{k}} + 2c_{\mathbf{k}+\mathbf{q}}^\dagger v_{\mathbf{k}'-\mathbf{q}}^\dagger v_{\mathbf{k}'}c_{\mathbf{k}}\right) \\
&- \sum_{\mathbf{k}}\mathbf{E}\cdot\left(\mu c_{\mathbf{k}}^\dagger v_{\mathbf{k}} + h.c.\right)
\end{aligned} \tag{2.12}$$

where $c_{\mathbf{k}}^{\dagger}$ and $c_{\mathbf{k}}$ are the creation and annihilation operators of the conduction band, respectively, and $v_{\mathbf{k}}^{\dagger}$ and $v_{\mathbf{k}}$ are the creation and annihilation operators of the valence band, respectively, ε_c (ε_v) is the band-model single electron (hole) energy. The microscopic interband polarization has the form

$$p_{\mathbf{k}} = \langle v_{\mathbf{k}}^{\dagger} c_{\mathbf{k}} \rangle. \tag{2.13}$$

In the Heisenberg picture, the polarization satisfies

$$\frac{\partial}{\partial t} p_{\mathbf{k}} = \langle \frac{i}{\hbar} \left[H, v_{\mathbf{k}}^{\dagger} c_{\mathbf{k}} \right] \rangle, \tag{2.14}$$

where $[*,*]$ denotes the commutator of two operators. Substituting Eq. (2.12) into Eq. (2.14), one can obtain

$$\begin{aligned} i\hbar \frac{\partial}{\partial t} p_{\mathbf{k}} = {} & \left[\varepsilon_c(\mathbf{k}) - \varepsilon_v(\mathbf{k}) \right] p_{\mathbf{k}} - \mu \cdot \mathbf{E} \left[n_c(\mathbf{k}) - n_v(\mathbf{k}) \right] \\ & + \sum_{\mathbf{k}',\mathbf{q} \neq 0} v_{\mathbf{q}} \left(\langle v_{\mathbf{k}'+\mathbf{q}}^{\dagger} v_{\mathbf{k}-\mathbf{q}}^{\dagger} v_{\mathbf{k}'} c_{\mathbf{k}} \rangle - \langle v_{\mathbf{k}+\mathbf{q}}^{\dagger} c_{\mathbf{k}'-\mathbf{q}}^{\dagger} c_{\mathbf{k}'} c_{\mathbf{k}} \rangle \right. \\ & \left. - \langle v_{\mathbf{k}}^{\dagger} c_{\mathbf{k}'+\mathbf{q}}^{\dagger} c_{\mathbf{k}+\mathbf{q}} c_{\mathbf{k}'} \rangle + \langle v_{\mathbf{k}}^{\dagger} v_{\mathbf{k}'+\mathbf{q}}^{\dagger} v_{\mathbf{k}'} c_{\mathbf{k}+\mathbf{q}} \rangle \right), \end{aligned} \tag{2.15}$$

where n_c and n_v are the numbers of the band-model electrons and holes, respectively.

The single-pair electron-hole basis includes only one parabolic valence band and one parabolic conduction band, known as the heavy-hole band. Thus, the exciton field $p_{\mathbf{k}}$ in the $1s$ heavy-hole exciton contribution to the interband polarization in the QW has the form [167]

$$p_{\mathbf{k}} = \Phi_{1s}^*(0) \langle a_h(-\mathbf{k},t) a_e(\mathbf{k},t) \rangle. \tag{2.16}$$

where $a_e(\mathbf{k},t)$ is the Heisenberg-picture annihilation operator of a conduction band electron and $a_h(-\mathbf{k},t)$ is the corresponding operator for a hole in the valence band. According to Eqs. (2.12)-(2.14) and under the limit of the $1s$ electron-hole single pair state, the exciton field $p_{\mathbf{k}}$ is derived up to third order in the light field amplitude on the Hartree-Fock-level [168], starting from the electron-hole vacuum as the initial state. In the mean-field approach and the coherent limit with $n_c \approx n_v \approx p^* p$, $p_{\mathbf{k}}$ satisfies [158, 164–167]

$$i\hbar \frac{\partial}{\partial t} p_{\mathbf{k}} = (\varepsilon_{\mathbf{k}}^x - i\gamma_x) p_{\mathbf{k}} - \Omega_{\mathrm{R}} E_{\mathbf{k}} + \frac{1}{L^2} \sum_{\mathbf{k}'\mathbf{k}''} p_{\mathbf{k}'+\mathbf{k}''-\mathbf{k}}^* p_{\mathbf{k}'} (\alpha_{\mathrm{PSF}} \Omega_{\mathbf{k}''} E_{\mathbf{k}''} + V_{\mathrm{HF}} p_{\mathbf{k}''}), \tag{2.17}$$

where $\varepsilon_{\mathbf{k}}^x$ is the free energy of excitons, γ_x is the exciton decay rate, L^2 is the normalized amplitude, the third-order term $p^* p E$ results from phase-space filling (PSF) among the

fermionic components of the excitons that are created by photon absorption and those of excitons with the strength $\alpha_{\mathrm{PSF}} = 4\pi a_0^2/7$, where a_0 is the exciton Bohr radius. The other third-order term p^*pp is due to mean-field, or Hartree-Fock (HF), Coulomb interaction among the excitons, with strength $V_{\mathrm{HF}} \approx 1.52 E_b a_0^2$, where E_b is the 2D exciton Rydberg energy. When considering only the linear parts of the coupled Eqs. (2.11) and (2.17), they can be written in a matrix form,

$$i\hbar \frac{\partial}{\partial t} \begin{pmatrix} E_{\mathbf{k}} \\ p_{\mathbf{k}} \end{pmatrix} = \begin{pmatrix} \hbar \omega_{\mathbf{k}}^c - i\gamma_{ph} & -\Omega_R \\ -\Omega_R & \varepsilon_{\mathbf{k}}^x - i\gamma_x \end{pmatrix} \begin{pmatrix} E_{\mathbf{k}} \\ p_{\mathbf{k}} \end{pmatrix} + \begin{pmatrix} E_{\mathbf{k},\text{pump}} \\ 0 \end{pmatrix}. \tag{2.18}$$

The eigenstates can be obtained by solving the coefficient matrix of Eq. (2.18), assuming that losses can be neglected

$$E_{U(L)}(\mathbf{k}) = \frac{E_C(\mathbf{k}) + E_X(\mathbf{k})}{2} \pm \frac{1}{2}\sqrt{[E_C(\mathbf{k}) - E_X(\mathbf{k})]^2 + 4\hbar^2\Omega_R^2}, \tag{2.19}$$

where $E_C(\mathbf{k}) = \hbar\omega_{\mathbf{k}}^c$ and $E_X(\mathbf{k}) = \varepsilon_{\mathbf{k}}^x$. The above eigenvalues indicate that there are two dispersion branches in polariton systems, the lower polariton branch $E_L(\mathbf{k})$ and the upper polariton branch $E_U(\mathbf{k})$, where the energy splitting between them is $2\hbar\Omega_R \approx \frac{d}{\pi a_B}\sqrt{\frac{NE_X}{\hbar^2 n_c \lambda}}$, d is the matrix element of the optical excitonic transition, a_B is the 2D exciton Bohr radius, and N is the number of QWs within the cavity [169].

The relation between each component of the polaritons and the two polariton branches can be described by a couple of unitary transformations

$$\Psi_{L,\mathbf{k}} = X_{\mathbf{k}} p_{\mathbf{k}} + C_{\mathbf{k}} E_{\mathbf{k}}, \tag{2.20}$$

$$\Psi_{U,\mathbf{k}} = -C_{\mathbf{k}} p_{\mathbf{k}} + X_{\mathbf{k}} E_{\mathbf{k}}. \tag{2.21}$$

where $\Psi_{L,\mathbf{k}}$ and $\Psi_{U,\mathbf{k}}$ are the wavefunctions of the lower polaritons and the upper polaritons in the momentum space, respectively. The coefficients, known as Hopfield coefficients [170], satisfy

$$|C_{\mathbf{k}}|^2 = \frac{1}{2}\left(1 + \frac{\Delta E(\mathbf{k})}{\sqrt{\Delta E(\mathbf{k})^2 + 4\hbar^2\Omega^2}}\right), \tag{2.22}$$

$$|X_{\mathbf{k}}|^2 = \frac{1}{2}\left(1 - \frac{\Delta E(\mathbf{k})}{\sqrt{\Delta E(\mathbf{k})^2 + 4\hbar^2\Omega^2}}\right), \tag{2.23}$$

with $\Delta E(\mathbf{k}) = E_X(\mathbf{k}) - E_C(\mathbf{k})$ and the normalization relation $|X_{\mathbf{k}}|^2 + |C_{\mathbf{k}}|^2 = 1$.
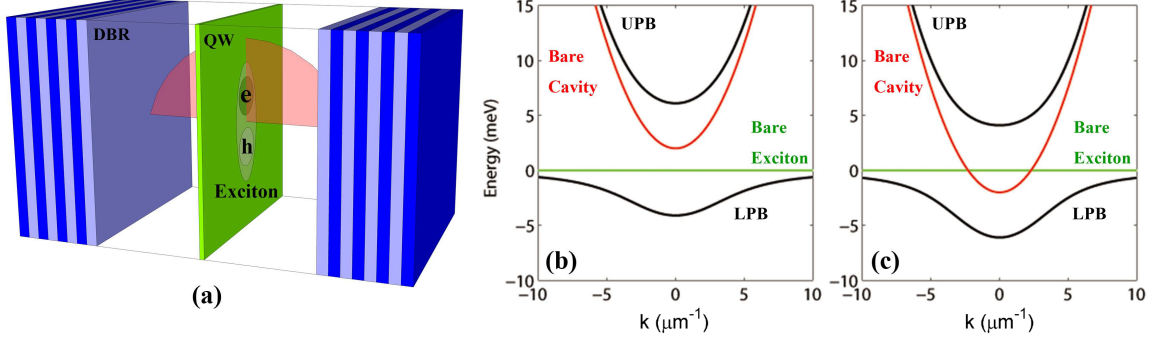
Fig. 2.1 (a) Sketch of a semiconductor microcavity consisting of a semiconductor quantum well (QW) sandwiched between two distributed Bragg reflectors (DBRs). Dispersion of polaritons at $m = 10^{-4}m_e$ and $\Omega_R = 5$ meV for (b) a positive exciton-photon detuning, $\delta = 2$ meV and (c) a negative exciton-photon detuning, $\delta = -2$ meV.

The shapes of the two branches are related to the exciton-photon detuning, $\delta = E_C(0) - E_X(0)$. Figures 1(b) and 1(c) show the dependence of the two polariton branches on the detuning. For a positive detuning $\delta = 2$ meV, there is no crossing of the cavity photon mode and the QW exciton mode [Fig. 2.1(b)]. In this case, the strong coupling of the LPB generate a shallow concave which leads to a high condensation density in the thermodynamic limit, but a short kinetic relaxation time. A positive detuning, $\delta > 0$ or $\Delta E(0) < 0$, leads to the lower polaritons containing more excitons than photons around $k = 0$, according to the Eqs. (2.20)-(2.23), where $|C_0|^2 < |X_0|^2$. The excitonic part of the LPB ground state increases with a higher detuning. This means that the greater the positive detuning, the more excitonic-like of the LPB is. For a negative detuning, $\delta = -2$ meV for instance, the two branches of bare excitons and cavity photons share the same energy states, which are undistinguishable, at the two crossing points [Fig. 2.1(c)]. The strong coupling, however, leads to Rabi-splitting, resulting in the generation of a sharp LPB which favours a low condensation density in the thermodynamic limit, but a long kinetic relaxation time. The more negative the detuning is, the sharper the LPB is. Note that the UPBs are always parabolic-like, while the LPBs are nonparabolic, instead showing an inflection point. Under negative detuning Eqs. (2.20)-(2.23) show that the lower polaritons at around $k = 0$ are composed of more photons, where $|C_0|^2 > |X_0|^2$. If the fundamental cavity mode that exists at normal incidence is resonant with the QW excitons with $\delta = 0$, the Hopfield coefficients satisfy the relation $|X_0|^2 = |C_0|^2 = \frac{1}{2}$. In this condition the lower polaritons are composed of half photons and half excitons.

Transforming Eqs. (2.11) and (2.17) back to the real space, one can obtain the coupled equations of motion

$$i\hbar\frac{\partial}{\partial t}E(\mathbf{r},t) = (H_{\text{cav}} - i\gamma_{ph})E(\mathbf{r},t) - \Omega_R p(\mathbf{r},t) + E_{\text{pump}}(\mathbf{r},t), \tag{2.24}$$

$$i\hbar\frac{\partial}{\partial t}p(\mathbf{r},t) = (H_{\text{exc}} - i\gamma_x)p(\mathbf{r},t) - \Omega_R(1 - \alpha_{\text{PSF}}|p(\mathbf{r},t)|^2)E(\mathbf{r},t) + V_{\text{HF}}|p(\mathbf{r},t)|^2 p(\mathbf{r},t). \tag{2.25}$$

where the Hamiltonian is $H_{\text{cav}} = \hbar\omega_{\mathbf{k}}^c$ and $H_{\text{exc}} = \varepsilon_{\mathbf{k}}^x$. These coherent equations are used to describe the dynamics of polaritons under coherent excitation with the pump field E_{pump} in the real space. The wavefunctions $E(\mathbf{r},t)$ and $p(\mathbf{r},t)$ represent the photonic and excitonic components, respectively, of polaritons in the real space.

2.2 The Gross-Pitaevskii equation

To describe the dynamics of polariton condensates in the bottom of the LPB, the coupled equations of motion for each component of polaritons can be combined into one equation according to Eqs. (2.20) and (2.21). We assume the cavity photon mode is almost resonant with the QW excitons around normal incident $k \approx 0$ with the photon-exciton detuning $\delta \approx 0$, which gives the following relations of each polariton branch and each component of them according to Eqs. (2.20)-(2.23) with $\Delta E = 0$:

$$E = \frac{1}{\sqrt{2}}(\Psi_L + \Psi_U), \quad p = \frac{1}{\sqrt{2}}(\Psi_L - \Psi_U), \quad \Psi_L = \frac{1}{\sqrt{2}}(E + p). \tag{2.26}$$

where Ψ_L and Ψ_U represent the wavefunctions of lower polaritons and upper polaritons in real space, respectively. It is known that under incoherent excitation polaritons undergo a condensation where almost all of them occupy the ground state of the LPB with $\Psi_L \gg \Psi_U \simeq 0$. According to Eqs. (2.24)-(2.26), the wavefunction of the lower polaritons reads

$$i\hbar\frac{\partial}{\partial t}\Psi_L = H_{\text{pol}}\Psi_L - \frac{i}{2}(\gamma_{ph} + \gamma_x)\Psi_L + \frac{1}{4}(\alpha_{\text{PSF}}\Omega_R + V_{\text{HF}})|\Psi_L|^2\Psi_L + \frac{1}{\sqrt{2}}E_{\text{pump}}, \tag{2.27}$$

where the Hamiltonian of polaritons $H_{\text{pol}} = \frac{1}{2}(H_{\text{cav}} + H_{\text{exc}}) - \Omega_R$. We assume that the dispersion of polariton condensates is parabolic in the vicinity of the bottom of the LPB, so the Hamiltonian of polaritons reads $H_{\text{pol}} \simeq \hbar\omega_0 - \frac{\hbar^2}{2m}\nabla_\perp^2$, where m is the effective mass of polariton condensates. In the theoretical study, we set the ground energy state of the LPB

$\hbar\omega_0 = 0$. One can obtain the simplified GPE

$$i\hbar\frac{\partial}{\partial t}\Psi(\mathbf{r},t) = -\frac{\hbar^2}{2m}\nabla_\perp^2\Psi(\mathbf{r},t) - i\gamma_c\Psi(\mathbf{r},t) + g_c|\Psi(\mathbf{r},t)|^2\Psi(\mathbf{r},t) + E_c(\mathbf{r},t), \qquad (2.28)$$

where the loss rate of polariton $\gamma_c \equiv \frac{1}{2}(\gamma_{ph} + \gamma_x)$, the nonlinear strength $g_c \equiv \frac{1}{4}(\alpha_{PSF}\Omega_x + V_{HF})$, and the coherent pump field $E_c \equiv \frac{1}{\sqrt{2}}E_{pump}$.
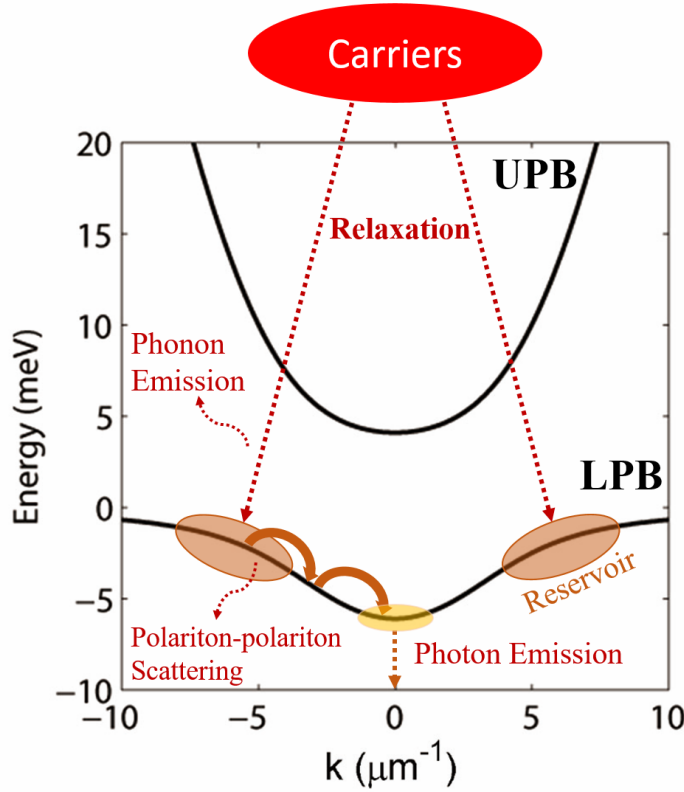

Fig. 2.2 Sketch of condensate formation scheme under an incoherent pump.

The mechanism of how to create the polariton condensates in experiments is sketched in Fig. 2.2. Free carriers are excited by an incoherent pump and relax to the so-called bottleneck region by phonon emission, forming an incoherent reservoir of excitons in the QWs. Due to the finite lifetime of polaritons, condensates are compensated by the incoherent exciton reservoir through scattering mechanisms. This reservoir not only provides the direct source of condensates but also interacts with condensates, which can be regarded as an internal potential affecting the distribution of condensates. Additionally, in a nonuniform semiconductor microcavity an external potential caused by fabrication is also important for the dynamics of condensates. Therefore, in a simple phenomenological model the GPE

(2.28) can be expanded to [161]

$$i\hbar\frac{\partial\Psi(\mathbf{r},t)}{\partial t} = \left[-\frac{\hbar^2}{2m}\nabla_\perp^2 - i\hbar\frac{\gamma_c}{2} + g_c|\Psi(\mathbf{r},t)|^2\right.$$
$$\left. + \left(g_r + i\hbar\frac{R}{2}\right)n(\mathbf{r},t) + V(\mathbf{r},t)\right]\Psi(\mathbf{r},t) + E_c(\mathbf{r},t), \qquad (2.29)$$

where the term $V\Psi$ represents the coupling of condensates and an external potential, the term $n\Psi$ represents the coupling of reservoir and condensates, with the real part being the reservoir-condensate interaction and the imaginary part being the gain of condensates, g_r is the interaction strength, and R is the condensation rate. The incoherent reservoir is created by a nonresonant pump P, and its density satisfies [161]

$$\frac{\partial n(\mathbf{r},t)}{\partial t} = \left[-\gamma_r - R|\Psi(\mathbf{r},t)|^2\right]n(\mathbf{r},t) + P(\mathbf{r},t). \qquad (2.30)$$

The dynamics of reservoir density is also related to the loss rate of exciton, including the recombination of excitons, represented by γ_r, and the condensation with the rate R corresponding to the gain in Eq. (2.29). This model, Eqs. (2.29) and (2.30), is a simple approximation to the true and highly complicated dynamics in the many-particle system.

One can understand Fig. 2.2 and the coupled Eqs. (2.29) and (2.30) as follows. In a semiconductor microcavity, an incoherent pump P with the frequency far above the excitonic resonance excites the electrons in the QW out of the conduction band forming "hot" excitons in the excited states. At cryogenic temperatures, the "hot" unstable excitons relax very fast towards the lower energy states of the lower polariton branch by phonon emission and form an exciton cloud in the bottleneck region. In this region, some of them disappear with a loss rate γ_r, caused by the recombination of electrons and holes. Due to the interaction of massive excitons, however, some of the excitons are scattered to the ground state of the lower polaritons forming a macroscopic quantum coherence (condensates) with the condensation rate R. Due to the finite life time of excitons and cavity photons, the condensates disappear with a loss rate γ_c. When the loss is compensated by the gain one can observe the polariton condensation, otherwise, there exists only the trivial solution for Eq. (2.29). The strong repulsive nonlinearity in our model is caused by two kinds of interactions, the polariton-polariton interaction represented by g_c and the interaction between polaritons and reservoir excitons represented by g_r. The polariton-exciton interaction can be regarded as a reservoir-induced potential or an optical-induced potential. Therefore, the distribution of the reservoir, which is related to the incoherent pump, strongly influences the dynamics of polaritons. In other words, the solutions of the condensates depends strongly on the shape of the excitation

pump. In Chapter 3 and Chapter 4, different pump profiles will be discussed for the generation of different solutions. Another type of potential is described by $V(\mathbf{r})$ which is caused by the fabrication of microcavity samples to change the cavity photon modes. In experiments the external potentials can be either time-independent or time-dependent. This type of potential will be discussed in detail in Chapter 5. The dynamics of polariton condensates can also be affected by a coherent pump field E_c, which will be introduced in Chapter 3.

It has been demonstrated that the coupled GPE can be used not only for the case $\delta \simeq 0$ but also for other photon-exciton detunings [122, 124, 156, 171], they are widely acceptable in a large range of semiconductor microcavity samples. Of course, for different microcavities the parameters may be different. For example, the effective mass of polariton condensates are related to the shape of the LPB which depends on the photon-exciton detuning. A positive detuning gives a larger mass, while a negative detuning leads to the condensates having a small mass. Roughly speaking, the effective mass has the range of $10^{-5} \sim 10^{-4} m_e$. The loss rate of condensates are strongly determined by the cavity photon lifetime which is decided by the quality of the microcavity. A higher quality can confine cavity photons inside the cavity for a longer time resulting in longer lifetimes, or smaller γ_c, for the polaritons, and vice versa. In previous observations the lifetimes of polaritons can be several picoseconds to hundreds of picoseconds [11–16, 72, 73, 90].

2.3   Chapter summary and concluding remarks

In this chapter, the polariton modes are theoretically investigated. The model used consists of the cavity photon mode, the QW exciton mode, and includes a term for their coupling. Due to the strong coupling, the two polariton branches become anticrossing where the splitting of the energy is related to the exciton-photon detuning. For a positive detuning, polaritons around the center of the LPB are composed primarily of excitons according to the Hopfield coefficients. For a negative detuning, however, the polaritons around the center of the LPB are more photonic-like with a smaller effective mass. To study the dynamics of polaritons, the coupled equations of motion are derived. The main aim of this thesis is to investigate the dynamics of polariton condensates governed by the GPE, from which approximate solutions are derived from the equations of motion. The GP model is the theoretical core of this thesis. Based on this model, the dynamics of polariton condensates are addressed in the following chapters under different pumps and different sample parameters.

Chapter 3

Phase defects of polariton condensates

The mean-field GPE is derived in Chapter 2. From this chapter we begin to investigate the nonlinear dynamics of polariton condensates based on the GPE and a coupled equation for the incoherent reservoirs created by incoherent pumps. Under the defocusing nonlinearity (the repulsive interaction) and the influence of reservoir dynamics, nonequilibrium polariton condensates show some novel properties. In this chapter, we start from the simplest case, the homogeneous excitation, and introduce a method how to find the stationary solutions and the stability analysis for general solutions, including both homogeneous and localized solutions. Under homogeneous excitation, the homogeneous pump creates a reservoir of "hot" excitons, which forms polariton condensates through a stimulated scattering mechanism. The linear instability of homogeneous condensates breaks the translational symmetry into spatial modulations forming a spatial pattern due to the nonlinear evolution. The instability-induced patterns are irregular and move randomly because the polariton condensate has a strong feedback effect on the reservoir, in the form of reservoir decay caused by stimulated scattering of reservoir excitons into polariton condensates. Above the modulational instability (MI) region, we find that the homogeneous solution breaks its translational symmetry and forms a turbulent state of phase defects (vortices). Considering the mechanism of the vortex formation, the result of the MI development, combined with the transition to BEC, we show that the presence of the incoherent reservoir affects substantially both the collective dynamics of vortices and homogeneous backgrounds. As a consequence, the vortices can lose their radial symmetry and develop either into spatially localized rotating phase defects or into nonlocalized spiraling waves, depending on the density of the reservoir.

To stabilize the turbulent motion of vortices under homogeneous excitation in the 2D case, we create a new periodically modulated pump by four coherent homogeneous optical beams. The periodic pump generates an optically induced lattice. In the presence of a periodic lattice, vortices are fixed in certain cells without the ability to move freely. Interestingly,

a coherent pulse can be used to move a vortex to a neighbouring cell, thereby achieving spatial manipulation. The vortices can also be incoherently controlled by switching the pump structure from two-dimensional (lattice) to one-dimensional (stripes). In the 1D case, dark solitons are demonstrated to be unstable [125, 126] under homogeneous excitation. Under periodic excitation, we demonstrate the existence, controlled creation, annihilation, and manipulation of stable dark solitons.

3.1 Homogeneous excitation

3.1.1 Homogeneous solutions

We investigate the dynamics of polariton condensates using the GP model, Eqs. (2.29) and (2.30), starting from the simplest case, without external potentials ($V = 0$) or coherent excitation ($E_c = 0$). A steady-state homogeneous solution (HS) of Eqs. (2.29) and (2.30) is formed under an incoherent homogeneous pump, that is, $P = P_0 = \text{constant}$. To theoretically seek the general stationary solutions, we assume the HSs, $\Psi_{\text{HS}}(x,t)$, with nonzero transversal momenta, $k \neq 0$, having the form in the one-dimensional (1D) case

$$\Psi_{\text{HS}}(x,t) = \Psi_0 e^{-i\omega t} e^{ikx}, \tag{3.1}$$

where Ψ_0 is the amplitude and ω is the chemical potential or eigenfrequency of the HSs. According to Eqs. (2.29), (2.30), and (3.1), a set of relevant formulas for the HSs are obtained, including the energy of condensates ($\hbar\omega$), the threshold pump intensity (P_{th}) for the condensation of polaritons, and the densities of coherent condensates ($|\Psi_0|^2$) and incoherent reservoir (n) as

$$\hbar\omega = \frac{\hbar k^2}{2m} + g_c|\Psi_0|^2 + g_r n, \tag{3.2}$$

$$P_{\text{th}} = \frac{\gamma_c \gamma_r}{R}, \tag{3.3}$$

$$|\Psi_0|^2 = \frac{P_0 - P_{th}}{\gamma_c}, \tag{3.4}$$

$$n = \frac{\gamma_c}{R}. \tag{3.5}$$

The relevant parameters under homogeneous excitations in uniform microcavities are: $m = 10^{-4}m_e$, $\gamma_c = 0.33$ ps$^{-1}\mu$m^2, $\gamma_r = 1.5\gamma_c$, $g_c = 6 \times 10^{-3}$ meVμm^2, $g_r = 2g_c$, and $R = 0.01$ ps$^{-1}\mu$m^2 taken from the experiments in Ref. [119]. Through these relations one can easily calculate the dependence of the density, $|\Psi_0|^2$, of HSs on the pump intensity, as well as

the nonlinearity-induced blue-shift in Eq. (3.2). Note that in Eq. (3.5), the density of the incoherent reservoir is independent of the pump intensity in this case.

To numerically find the general stationary solutions of condensates, including HSs and localized solutions for the later chapters, we assume a typical standard ansatz in polar coordinates in the form

$$\Psi(r,\varphi,t) = \Psi(r)e^{iM\varphi}e^{-i\omega t}, \tag{3.6}$$

where $\Psi(r)$ is the stationary amplitude and the integer M is the topological charge or vorticity corresponding to vortices, while $M = 0$ corresponding to nonvortex solutions. The stationary solution can be reached when the reservoir is time-independent with the condition $\partial n/\partial t = 0$,

$$n(r) = \frac{P}{\gamma_r + R|\Psi|^2}. \tag{3.7}$$

Substituting Eqs. (3.6) and (3.7) into the model, Eqs. (2.29) and (2.30), yields a time-independent equation for the stationary amplitude using the Laplacian in polar coordinates $\nabla^2 \equiv \frac{1}{r}\frac{\partial}{\partial r} + \frac{\partial^2}{\partial r^2} + \frac{1}{r^2}\frac{\partial^2}{\partial \varphi^2}$,

$$\omega\Psi = \left[-\frac{\hbar}{2m}\frac{\partial^2}{\partial r^2} - \frac{\hbar}{2mr}\frac{\partial}{\partial r} + \frac{\hbar M^2}{2mr^2} - i\frac{\gamma_c}{2} + \frac{g_c}{\hbar}|\Psi|^2 + \left(\frac{g_r}{\hbar} + i\frac{R}{2}\right)\frac{P}{\gamma_r + R|\Psi|^2} \right]\Psi. \tag{3.8}$$

One can discretize the partial derivatives in Eq. (3.8) using the finite difference method into a discrete equation, then solve the discrete equation using Newton's iteration method. This method is also known as the Newton-Raphson method from an initial guess, for obtaining the stationary solutions. It is worth noting that the initial guess should be close to the accurate solution, at least not too far away from it, otherwise the initial guess will not converge, or it will converge very quickly to the trivial solution.

After finding a stationary solution, it is necessary to find out whether it is stable. The method to study the stability of a stationary solution is to add a relatively small perturbation into the stationary solution and determine whether the perturbation will vanish or increase after a short time. If it increases with time, the stationary solution will be destroyed such that the solution is unstable. The perturbation should be added into both the stationary ansatzes for condensates and reservoir excitons,

$$\Psi(r,\varphi,t) = [\Psi(r) + \delta\Psi(r,\varphi,t)]e^{iM\varphi}e^{-i\omega t}, \tag{3.9}$$

$$n(r,\varphi,t) = n(r) + \delta n(r,\varphi,t), \tag{3.10}$$

where $\delta\Psi(r,\varphi,t) = \delta\Psi(r)e^{iM'\varphi}e^{\lambda t}$ is the perturbation in the amplitude of condensates and $\delta n(r,\varphi,t) = \delta n(r)e^{iM'\varphi}e^{\lambda t}$ is the perturbation in the density of the reservoir, $\delta\Psi(r)$ and $\delta n(r)$ are the amplitudes of the perturbations, M' is the perturbed topological charge for vortex solutions with the case $M' = 0$ corresponding to nonvortex solutions, λ is a complex eigenvalue representing the growth rate of the perturbations.

Substituting the perturbed ansatzes, Eqs. (3.9) and (3.10), into the model Eqs. (2.29) and (2.30) yields two coupled equations by collecting the linear terms of $\delta\Psi$ and δn and the terms oscillating as $e^{\lambda t}$,

$$
\begin{aligned}
\lambda\delta\Psi = &\left[i\omega + i\frac{\hbar}{2mr} + i\frac{\hbar}{2m} - i\frac{\hbar(M+M')^2}{2mr^2} - \frac{\gamma_c}{2} - i\frac{2g_c}{\hbar}|\Psi|^2 - \left(i\frac{g_r}{\hbar} - \frac{R}{2}\right)n\right]\delta\Psi \\
&- i\frac{g_c}{\hbar}\Psi^2\delta\Psi^* - \left(i\frac{g_r}{\hbar} - \frac{R}{2}\right)\Psi\delta n,
\end{aligned}
\tag{3.11}
$$

$$
\lambda\delta n = \left(-\gamma_r - R|\Psi|^2\right)\delta n - R\Psi^* n\delta\Psi - R\Psi n\delta\Psi^*.
\tag{3.12}
$$

From Eq. (3.11) the conjugate part of the perturbation, $\delta\Psi^*$, satisfies

$$
\begin{aligned}
\lambda\delta\Psi^* = &\left[-i\omega - i\frac{\hbar}{2mr} - i\frac{\hbar}{2m} + i\frac{\hbar(M+M')^2}{2mr^2} - \frac{\gamma_c}{2} + i\frac{2g_c}{\hbar}|\Psi|^2 + \left(i\frac{g_r}{\hbar} + \frac{R}{2}\right)n\right]\delta\Psi^* \\
&+ i\frac{g_c}{\hbar}(\Psi^*)^2\delta\Psi + \left(i\frac{g_r}{\hbar} + \frac{R}{2}\right)\Psi^*\delta n.
\end{aligned}
\tag{3.13}
$$

The three coupled equations, Eqs. (3.11)-(3.13), can be written in a matrix form,

$$
\begin{pmatrix}
\alpha & -i\frac{g_c}{\hbar}\Psi^2 & -\left(i\frac{g_r}{\hbar} - \frac{R}{2}\right)\Psi \\
i\frac{g_c}{\hbar}(\Psi^*)^2 & \alpha^* & \left(i\frac{g_r}{\hbar} + \frac{R}{2}\right)\Psi^* \\
-R\Psi^* n & -R\Psi n & -\gamma_r - R|\Psi|^2
\end{pmatrix}
\begin{pmatrix}
\delta\Psi \\
\delta\Psi^* \\
\delta n
\end{pmatrix}
= \lambda
\begin{pmatrix}
\delta\Psi \\
\delta\Psi^* \\
\delta n
\end{pmatrix},
\tag{3.14}
$$

where $\alpha = i\omega + i\frac{\hbar}{2mr} + i\frac{\hbar}{2m} - i\frac{\hbar(M+M')^2}{2mr^2} - \frac{\gamma_c}{2} - i\frac{2g_c}{\hbar}|\Psi|^2 - \left(i\frac{g_r}{\hbar} - \frac{R}{2}\right)n$, so that the eigenvalue λ can be obtained by numerically solving the matrix in Eq. (3.14). The real part of λ, λ_r, represents the instability growth rate. If $\lambda_r \leq 0$, the solutions are stable due to the decay of the perturbations in Eqs. (3.9) and (3.10), while if $\lambda_r > 0$ the perturbation will increase exponentially according to the term $e^{\lambda t}$ over time and destroy the stationary solutions.

Figure 3.1(a) shows the dependence of the density of HSs on the pump intensity. The HSs are unstable in the region where the pump intensity is just above the threshold, the MI region. The linear growth rate of the perturbation is presented in Fig. 3.1(b), where the MI of HSs happens in the $\lambda_r > 0$ (colorful) region. The MI is associated with the parametric generation of field components with nonzero momenta k.

Generally, the MI requires an attractive nonlinearity analogous to the Kerr nonlinearity in focusing media [172–175]. It is demonstrated that the saturation of the incoherent reservoir as introduced in Ref. [126] with an effective attractive nonlinearity also supports MI. It is
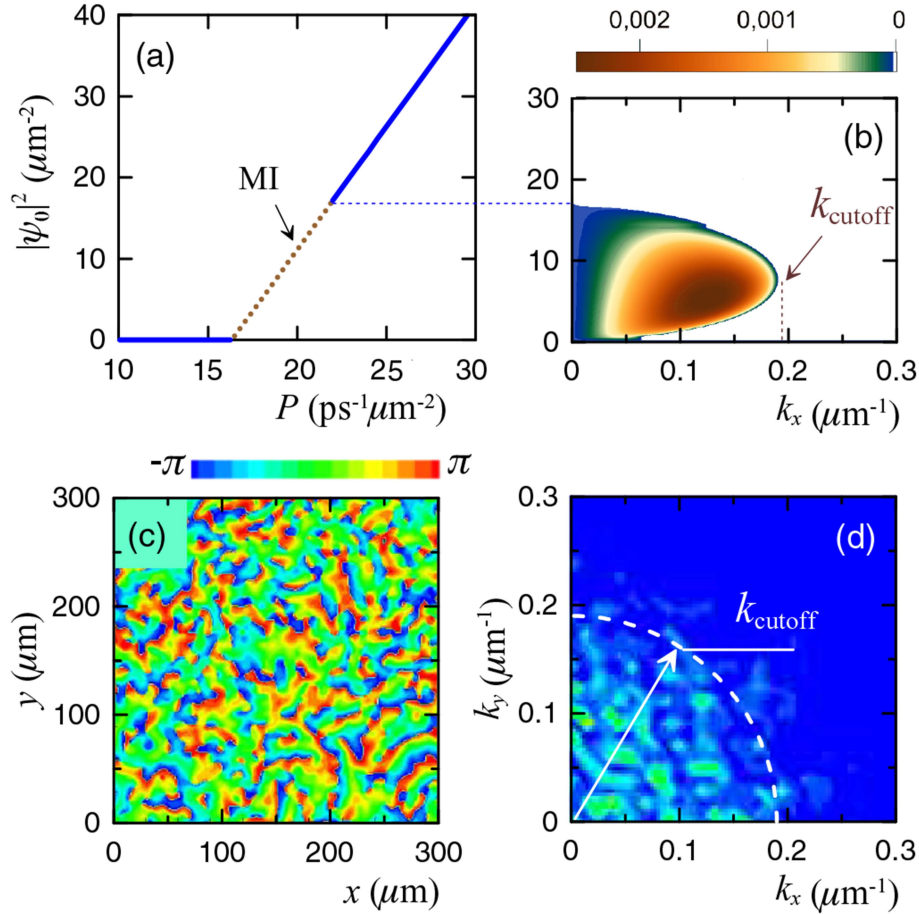

Fig. 3.1 (a) Dependence of condensate density on pump intensity. The red dotted line represents the unstable solutions (MI region), while the blue solid lines are stable solutions. (b) Growth rate of the small perturbation as a function of momentum and condensate density. Distribution of the condensate phase (c) in real space and (d) the density in reciprocal space within the MI domain for $P_0 = 18 \, \text{ps}^{-1} \mu \text{m}^{-2}$. k_{cutoff} is the in-plane wave vector representing the boundary of stable and unstable solutions. From [176].

worth noting that, due to the repulsive interaction of excitons, polaritons exhibit clearly defocusing nonlinearity, which also causes the MI of condensates. This obvious contradiction clearly elucidates the strong influence of the nonequilibrium nature of the system on the nonlinear phenomenon [126], which requires inclusion of an incoherent reservoir of excitons for compensating the loss of polariton condensates. To illustrate the influence of the nonequilibrium system on nonlinear behaviors. The nonlinear energy shift, $\hbar \omega_{\text{nl}}$, is considered and

obtained from Eq. (3.2) as

$$\hbar\omega_{\mathrm{nl}} = g_c|\Psi_0|^2 + g_r\frac{P_0}{\gamma_r + R|\Psi_0|^2}, \tag{3.15}$$

where the first term of the right side of Eq. (3.15), which is positive, represents the blue shift originating from the repulsive polariton-polariton interaction, whereas the second term represents the saturation of the reservoir. We define the effective nonlinearity coefficient as

$$g_{\mathrm{eff}} = \hbar\frac{\partial\omega_{\mathrm{nl}}}{\partial|\Psi_0|^2} = \left(g_c - \frac{g_r P_0 R}{(\gamma_r + R|\Psi_0|^2)^2}\right). \tag{3.16}$$

According to Eqs. (3.5) and (3.7), (3.16) can be simplified as

$$g_{\mathrm{eff}} = g_c\left(1 - \frac{g_r\gamma_c^2}{g_c R P_0}\right). \tag{3.17}$$

It is clear that the nonlinear efficiency changes sign around the point

$$P_{\mathrm{MI}} = \frac{g_r\gamma_c^2}{g_c R}, \tag{3.18}$$

that is, when $P_0 < P_{\mathrm{MI}}$, $g_{\mathrm{eff}} < 0$ which means the nonlinear response is focusing, so that one can explain why the MI appears in our defocusing nonlinear model. As $P_0 > P_{\mathrm{MI}}$, the nonlinear response changes to defocusing where the HSs are stable, and the critical point is clearly presented in Fig. 3.1(a).

In the MI region, $P_{\mathrm{th}} < P_0 < P_{\mathrm{MI}}$, translational symmetry breaking leads to the formation of nonuniform turbulent states of the condensate. Figure 3.1(c) shows phase defects which move chaotically and overlap. The Fourier transformation shows that most of the spatial momenta are bounded within the ring [Fig. 3.1(d)] with the radius given by the cutoff momenta of the unstable modes k_{cutoff} calculated in Fig. 3.1(b). Unlike in the coherently pumped polaritonic systems [20-23], in polariton condensates the formation of stationary periodically modulated patterns are not found due to destabilization caused by fluctuations of the reservoir.

3.1.2   Formation of spiraling waves

Although HSs are stable above the MI region, the initial noise leads to condensates that are excited to vortex states [Figs. 3.2(a) and 3.2(b)] instead of HSs. The main reason for the existence of phase defects in the stable region is that the pump creates a reservoir very quickly,

which then leads to the excitons condensating to the coherent state of the LPB. The hysteresis of the coherent response leads to a rapid increase in the density of the condensate, whilst the phase transmission lags behind. This results in the formation of topological defects, known as vortices, analogous to the Kibble-Zurek theory. It is known that a vortex size increases
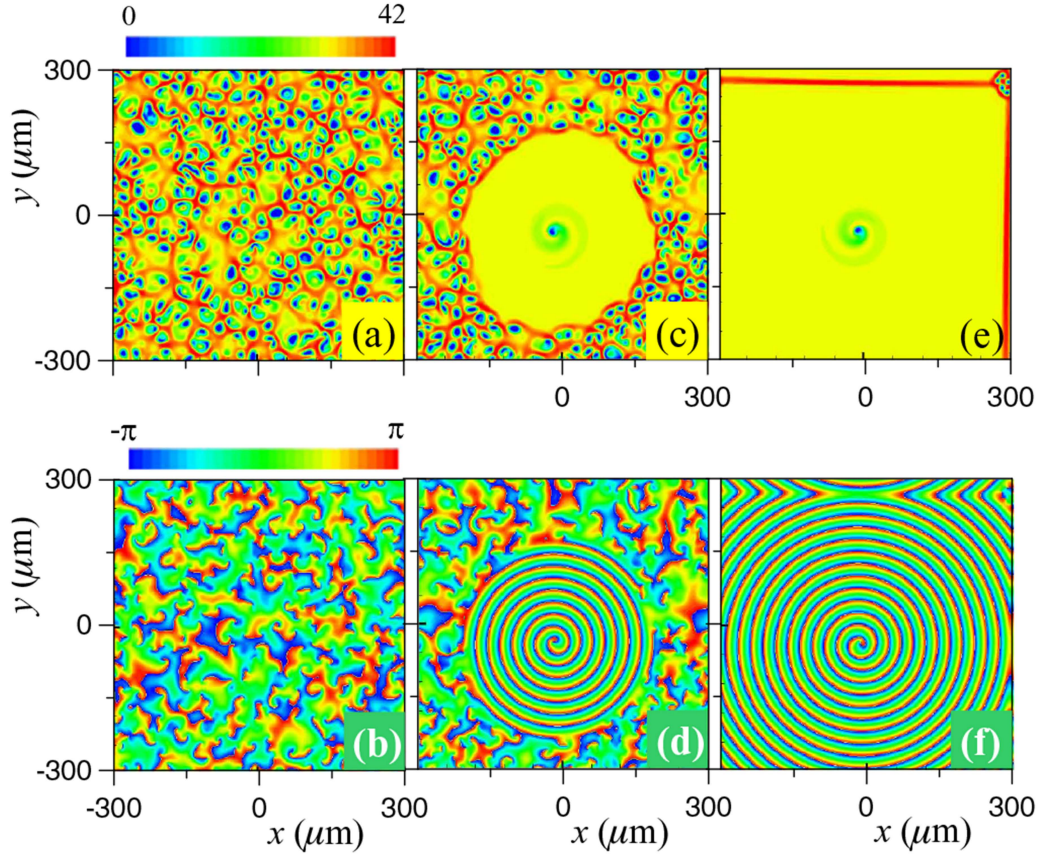

Fig. 3.2 Time evolution of a spiralling wave. Distributions of the condensate density (upper row) and phase profiles (lower row) at different time points for $P_0 = 27 \text{ ps}^{-1}\mu\text{m}^{-2}$. (a), (b) Initial turbulent state of the condensate at $t = 1000$ ps. (c), (d) Onset of a spiraling wave at $t = 5000$ ps. (e), (f) The spiraling waves at $t = 11000$ ps. From [176].

as pump intensity decreases until they overlap with each other leading to vortices are not structured and the chaotic behavior is seen when the distance between vortices is substantially smaller than their typical core size. However, after some sufficiently long time of about several thousands of polariton lifetime, the system switches spontaneously into a more regular regime, characterized by the formation of a single spiraling topological defect (Fig. 3.2). The outgoing radiation with a period of 144 ps from the center of the topological solution repels the surrounding inhomogeneities of the profile and other topological defects. This gives an additional purely dissipative mechanism which enforces a long-range spatial coherence in

nonequilibrium systems operating in the regime of strong turbulence. The spiraling wave drives away other phase defects and eventually covers the whole computational window. Similar spiraling waves are also found in other nonequilibrium dissipative systems [74,75]. The spiraling wave have been proven to be robust supported by the polariton nonequilibrium system, which can be found in the pump interval $P_{MI} < P_0 < 32$ ps$^{-1}\mu$m^{-2}.

Note that the phase defects appear in pairs, according to law of conservation of angular momentum, which is also valid for the turbulent state. The spiraling state with a nonzero orbital angular momentum can also emerge even if the initial turbulent state is nonrotating. During the turbulent dynamics of vortices, the symmetry between the two defects within a pair is broken so that only one of them develops into the spiraling wave. One can see that after the formation of the spiralling wave, Figs. 3.2(e) and 3.2(f), the total orbital angular momentum of the condensate within the computational window remains zero, because periodic boundary conditions in both x and y directions are used in our simulations. To ensure that the periodic boundary conditions do not influence the formation of the spiraling wave, we performed additional numerical simulations of the dynamics of condensates under a localized pump with a platform in the form of a super-Gaussian intensity distribution. In this condition, the boundaries are far away from the solution and do not have any contribution to the turbulent vortices. It is found that the spiraling waves appear also within the platform region of the localized pump, and the solution tails vanish at the boundaries of the computational window. These calculations provide solid proof that the existence of the spiraling waves is independent of the periodic boundary conditions in our simulation.

3.1.3 Collective dynamics of vortices

When the pump intensity is stronger, far above the MI threshold, one can see that from Eq. (3.17) the dynamics of condensates is dominated by a defocusing nonlinearity. If the polaritons are pumped incoherently from a small white noise as discussed above, a lot of phase defects (vortices) can survive and occupy the whole window under the formation of spatially coherent condensates. However, the vortices are not fixed, they move randomly because two vortices with the same topological charges repel each other, while two vortices with opposite topological charges attract each other. Two attracting vortices mutually annihilate if the distance between them is too small. When the distances between the vortices are large enough or the influence from the surroundings reaches the balance between attractions and repulsions, vortices will not annihilate anymore and keep the dynamical equilibrium [Fig. 3.3].

Just above the spiraling wave domain, the vortex size is squeezed by the stronger background. The number of phase defects converges eventually to some constant value indicating

the formation of a coherent state with a finite number of defects as shown in Fig. 3.3(a). At this point the vortices sustain a dynamic equilibrium under the interactions with other vortices and move chaotically. It is remarkable that the average separations between nearest
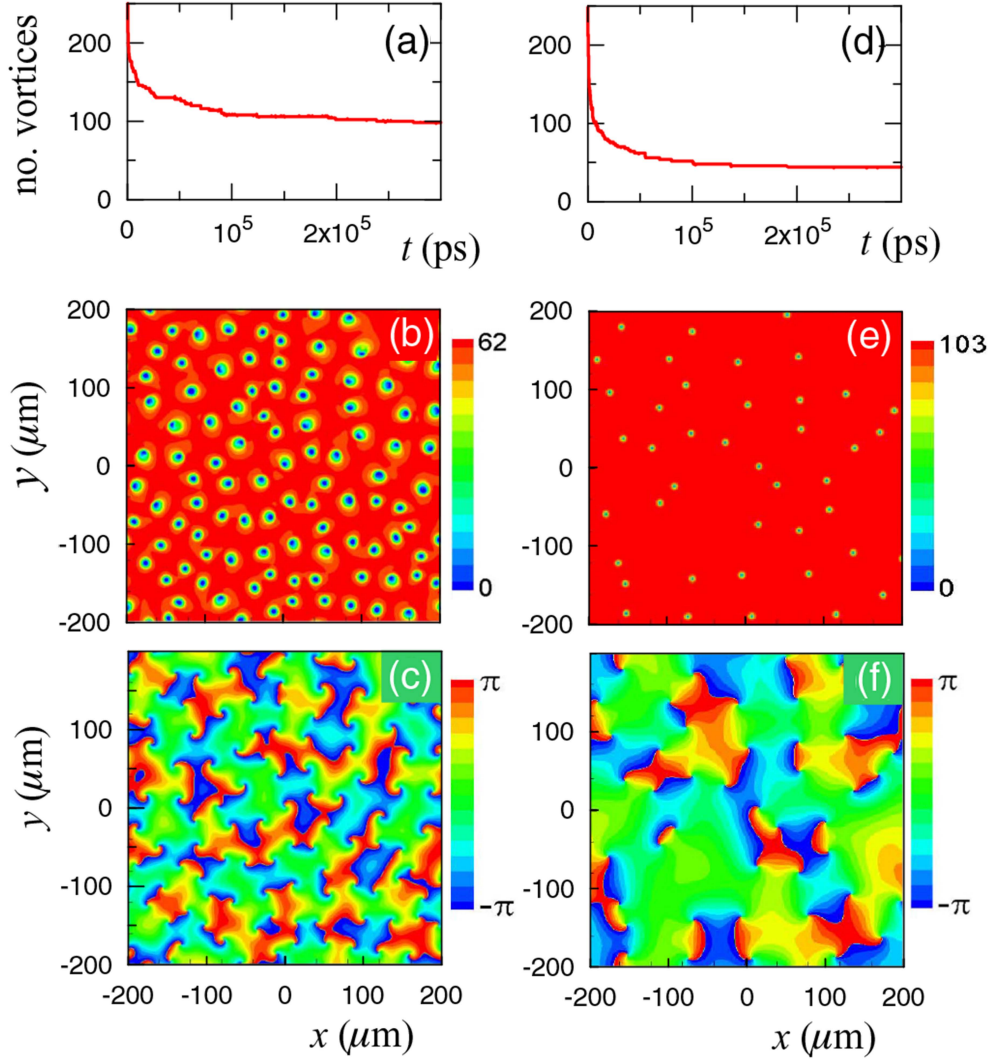

Fig. 3.3 Dynamics of condensates far above the MI region for (a)-(c) $P_0 = 35 \text{ ps}^{-1}\mu\text{m}^{-2}$ and (d)-(f) $P_0 = 50 \text{ ps}^{-1}\mu\text{m}^{-2}$. (a), (d) Time evolutions of the vortex number. (b), (e) Density distributions of condensates. (c), (f) Phase distributions of condensates. From [176].

vortices remain more or less constant as shown in Figs. 3.3(b) and 3.3(c). In addition, the vortices themselves become unstable and develop into radially asymmetric rotating structures, as can be seen in the snapshot profiles in Figs. 3.3(b) and 3.3(c). For even stronger pump intensity the average distance between vortices under dynamical equilibrium becomes even larger as shown in Figs. 3.3(d)-3.3(f). Note that this dynamical equilibrium forms over a shorter time about hundreds of nanoseconds. For a very strong pump, $P_0 > 80 \text{ ps}^{-1}\mu\text{m}^{-2}$,

the whole number of vortices drops gradually with time and approaches zero. The reason is that under much stronger excitation the condensation is achieved in a very short time. During this time, a phase defect does not have enough time to form a vortex, but is instead pumped into the coherent HS. Therefore, the stronger the pump intensity, the smaller the vortex size.

It is worth noting that there are several differences between the spiraling topological states and the vortices. First, there is no rotational symmetry as seen for the vortices in the spiraling waves in Fig. 3.2. Second, spiraling topological states are not stationary and experience uniform rotation of the density with a typical rotation period of about 144 ps. In contrast, vortex positions are fixed in the absence of additional attraction or repulsion. Finally, in the case of spiraling topological states, unlike vortices, the profile converges to the homogeneous traveling wave solution with the amplitude Ψ_0 and a nontrivial momentum k for spiralling waves. Apparently, the spiralling wave is characterized by a permanent radial flux of exciton-polaritons from the vortex center to the periphery and therefore resembles a point like source of ring waves. These spiraling waves can exist only in nonequilibrium dissipative systems.

3.2   Periodic excitation

In the above section, we investigated the vortices under homogeneous pumps and their turbulent dynamics, leading to the conclusion that the control of vortices is very difficult due to the free background and their interaction. In addition, 1D dark solitons are to be unstable if the background is homogeneous because of the nonequilibrium dynamics of polaritons. It is known that a periodic lattice can be used to stabilize the solutions and avoid the critical collapse in the cubic nonlinear system [177–184]. In this section, we use a periodic pump to create a periodic reservoir which can be regarded as an internal periodic lattice for the stabilization of phase defects.

Figure 3.4(a) shows a microcavity sample sandwiched between two DBRs with a QW. To generate a periodic pump, two coherent plane waves are launched parallel to the x axis with small incidence angle on top of the sample, forming a periodic distribution of the pump intensity along the x direction. The 1D intensity distribution of the periodic pump is shown in Fig. 3.4(b). If two additional same plane waves are launched parallel to the y axis with the same incidence angle, four coherent plane waves create a 2D optical lattice in intensity as shown in Fig. 3.4(c). All parameters of the Eqs. (2.29) and (2.30) in this section are the same as those in Sec. 3.1 except the effective mass m and the loss rate of condensates γ_c. In this section the effective mass $m = 10^{-4} m_e / a$ and the loss rate γ_c are variable, where, a is a constant representing the effective mass rate which can be adjusted if considering different

detunings of the cavity photon mode and the QW excitons. The influence of effective mass and loss rate of condensates on the formation of dark solitons will be discussed below.
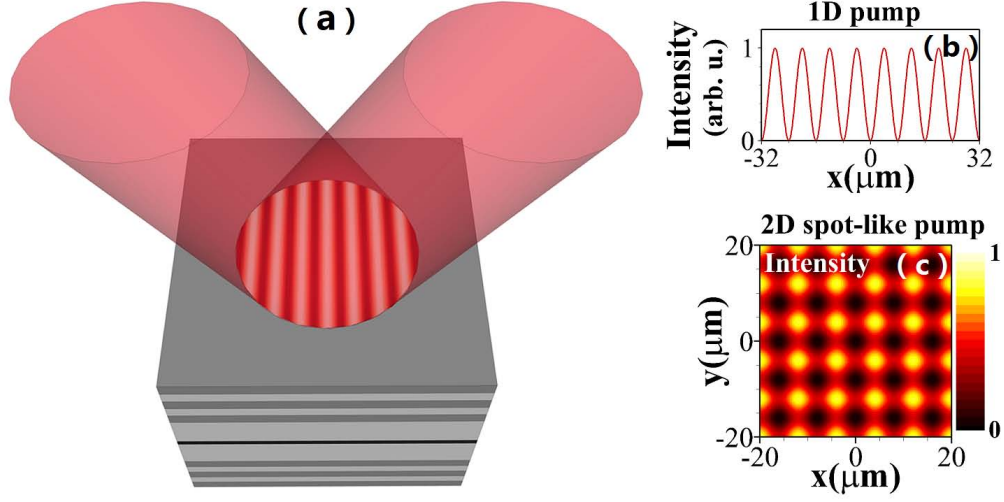

Fig. 3.4 (a) Sketch of a semiconductor microcavity with a quantum well (QW) sandwiched between two distributed Bragg reflectors (DBRs). Two coherent homogenous optical beams creates a periodically incoherent pump for the excitation of polariton condensates. Distributions of periodic pump intensity in (b) 1D and (c) 2D cases. From [185].

3.2.1   Dark solitons

In the 1D model, the periodic pump can be written

$$P(x) = P_0 \sin^2 \left(\frac{\pi x}{d} \right), \tag{3.19}$$

where $d = 8$ μm is the period of the pump intensity, and its distribution is shown in Fig. 3.4(b). One can see that the minimum value of the pump intensity, pump valleys, is located at

$$x_v = dN, \quad N = 0, \pm 1, \pm 2, \cdots \tag{3.20}$$

while the maximum value of the pump intensity, pump peaks, is located at

$$x_p = dN + \frac{d}{2}, \quad N = 0, \pm 1, \pm 2, \cdots \tag{3.21}$$

It is known that an incoherent pump always create a reservoir which is similar to the pump profile, so that a periodic pump creates a periodic reservoir which supports a periodic solution. Figure 3.5(a) shows the existence region of steady-state periodic solutions depending on

the pump intensity P_0. When the pump intensity is within some range above the pump threshold, $2 < P_0 < 12$ ps$^{-1}\mu$m^{-2}, the density distribution of periodic solutions is similar to that of the periodic pumps or the distribution of reservoir excitons, the minimum intensity of the solutions $|\Psi|^2 = 0$ as shown in the insert. However, when the pump intensity is
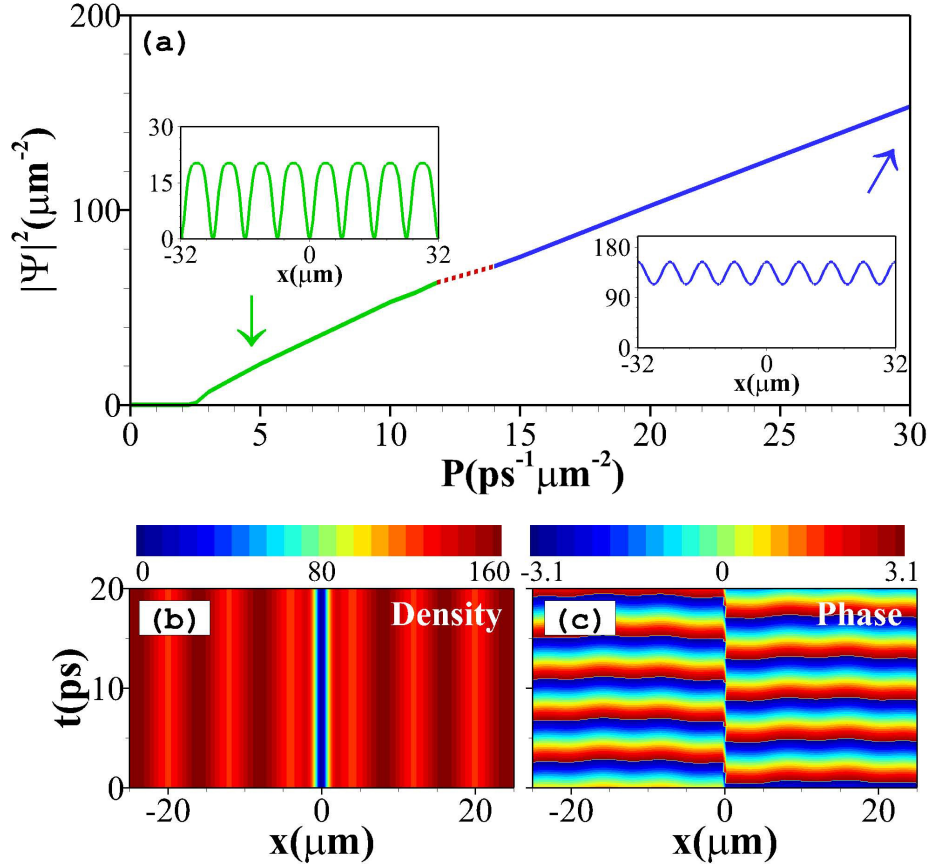

Fig. 3.5 (a) Dependence of peak density of steady state periodic solutions supported by 1D periodic pumps and pump intensity. Solid lines represent stable solutions, while dashed line represents unstable solutions. The inserts show the solutions at $P_0 = 5$ ps$^{-1}\mu$m^{-2} and $P_0 = 30$ ps$^{-1}\mu$m^{-2}, respectively. Time evolutions of (b) the density and (c) the phase of a stable dark soliton in 1D at $P_0 = 30$ ps$^{-1}\mu$m^{-2}. From [185].

larger, $P_0 > 14$ ps$^{-1}\mu$m^{-2}, the periodic reservoir is more like a potential which traps more condensates inside the reservoir valleys and results in the appearance of solution peaks in the pump valleys, and the minimum of the periodic solution locates in the pump peaks. It is worth noting that the contrast of the periodic solution reduces as the pump intensity increases, such that the solution approaches to the homogeneous solution at larger pump intensity.

The transition state between two kinds of periodic solutions happens in the small region of $12 \leq P_0 \leq 14 \text{ ps}^{-1}\mu\text{m}^{-2}$, where the solutions oscillate irregularly.

At larger pump intensities, $P_0 > 14 \text{ ps}^{-1}\mu\text{m}^{-2}$, besides the periodic solutions, a dark soliton is obtained. At these pump powers the density of condensates approaches zero [Fig. 3.5(b)] and a π phase jump is seen [Fig. 3.5(c)] in one of the pump valleys ($x = 0 \, \mu\text{m}$ for instance). Therefore, under higher pump intensity both periodic solutions and dark solitons can be excited due to different initial conditions. For near homogeneous initial conditions (without or with very few phase defects), condensates are easily pumped to the pure periodic solutions, while dark solitons can survive when phase defects (initial white noise) appear around pump valleys. Therefore, in this model, dark solitons can be found only in pump valleys or the peaks of the periodic background.
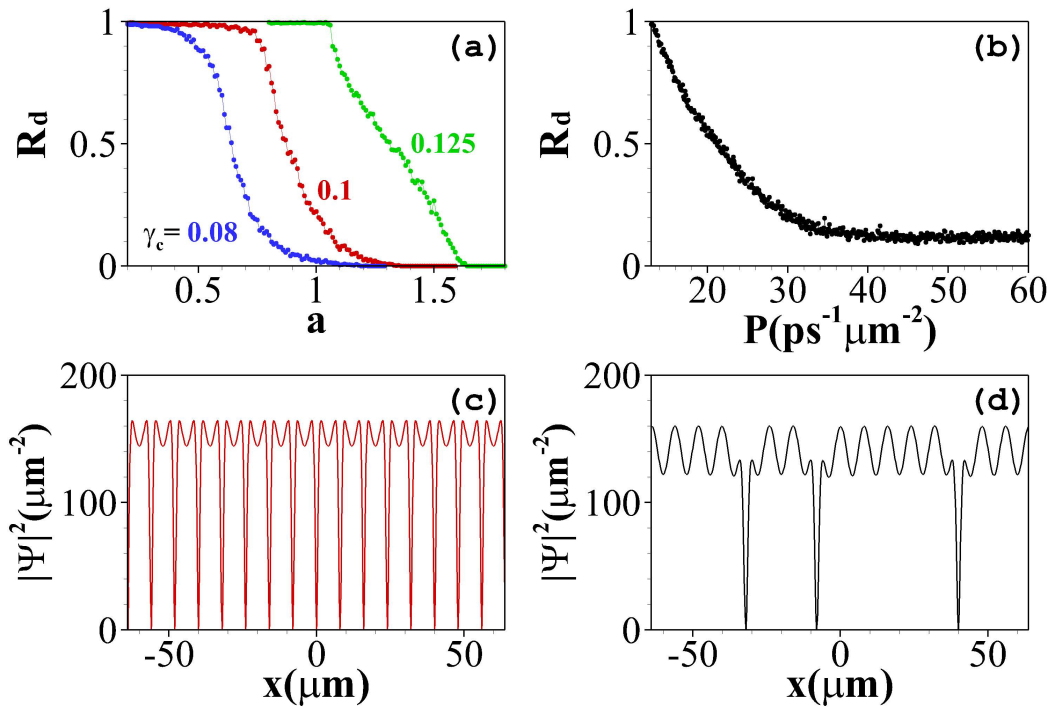

Fig. 3.6 Number of dark solitons. (a) Dependence of the dark soliton rate on the effective mass rate at $P_0 = 30 \text{ ps}^{-1}\mu\text{m}^{-2}$ for $\gamma_c = 0.08$, 0.1, and 0.125 ps^{-1}. (b) Dependence of the dark soliton rate on the pump intensity with $a = 1$ and $\gamma_c = 0.1 \text{ ps}^{-1}$. Profiles of dark solitons with (c) $\gamma_c = 0.1 \text{ ps}^{-1}$, $a = 0.5$, and $P_0 = 30 \text{ ps}^{-1}\mu\text{m}^{-2}$, and (d) $\gamma_c = 0.1 \text{ ps}^{-1}$, $a = 1$, and $P_0 = 30 \text{ ps}^{-1}\mu\text{m}^{-2}$. From [185].

Due to the spontaneous formation of condensates, initial noise strongly influences the position of dark solitons. The number of dark solitons depends on the initial presence of phase defects near pump valleys, but equally importantly depends on system parameters such as dissipation and effective mass [176]. In order to count the number of dark solitons, we

define the ratio

$$R_d = \frac{number\ of\ dark\ solitons}{number\ of\ pump\ valleys}, \quad 0 \leq R_d \leq 1. \tag{3.22}$$

It is shown that in Fig. 3.6(a) the number of dark solitons are strongly related to the loss rate and the effective mass rate of condensates for noisy initial conditions and a fixed pump intensity. For a fixed loss rate, $\gamma_c = 0.1$ ps^{-1} for instance, more dark solitons are excited with $R_d \to 1$ for larger effective mass (smaller a), because a condensate having larger effective mass is less correlated to its neighbors, or more independent, resulting in the survival of more phase defects during the excitation. When $R_d = 1$, dark solitons are formed in each pump valley as shown in Fig. 3.6(c). Conversely, a condensate with smaller effective mass (larger a) is more correlated to others, which allows the defects caused by the initial noise to disappear easier and therefore less dark solitons are formed [Fig. 3.6(d)] during the excitation. When $R_d = 0$, there are no longer any surviving dark solitons because of the extremely strong correlations between condensates. For a fixed effective mass, $a = 1$ for instance, the correlation between condensates is stronger if the polaritons have longer lifetimes (smaller γ_c), which results in less dark solitons formed. Conversely, larger γ_c polaritons disappear very quickly, leading to more dark soliton excitations due to the weaker correlation between condensates. In conclusion, the weaker the correlations between different locations in a condensate (with smaller a and smaller γ_c), the greater the number of surviving dark solitons, and vice versa.

The number of dark solitons also depends on the pump intensity when all other parameters are fixed, as shown in Fig. 3.6(b). Most of the pump valleys are excited to dark solitons when the pump intensity is smaller, and the number of dark solitons reduces as the pump intensity increases. The reason is that for larger pump intensity the contrast of periodic solutions is small and closer to homogeneous. This means that the effect of the lattice is reduced and therefore phase defects can interact more freely with nearby defects. Therefore, most of the phase defects disappear after reaching the steady state. It is the same reason why the dark solitons cannot exist under homogeneous excitation [125, 126]. As pump intensity further increases, the condensates are excited to a steady state in a very short time, and during this time condensates do not have enough response time to interact with each other. As a consequence, the number of vortices asymptotes to a constant for larger pump intensity.

In experiments the initial conditions of microcavity polaritons are always noisy. It is difficult to excite a pure periodic solution, a single dark soliton, or a dark soliton to a specified pump valley from noise because the initial white noise in uncontrollable. Therefore, to create or annihilate a specified dark soliton as illustrated in Fig. 3.7 is critical that one is able to control the dark solitons. It is known that the phase defects under homogeneous excitations are unstable. They disappear and transfer to the homogeneous solutions when reaching the

steady state. To counter this, a homogeneous pump can first be used to create a homogeneous solution [$t < 1000$ ps in Fig. 3.7(a)] in order to smooth the initial noise. A few several
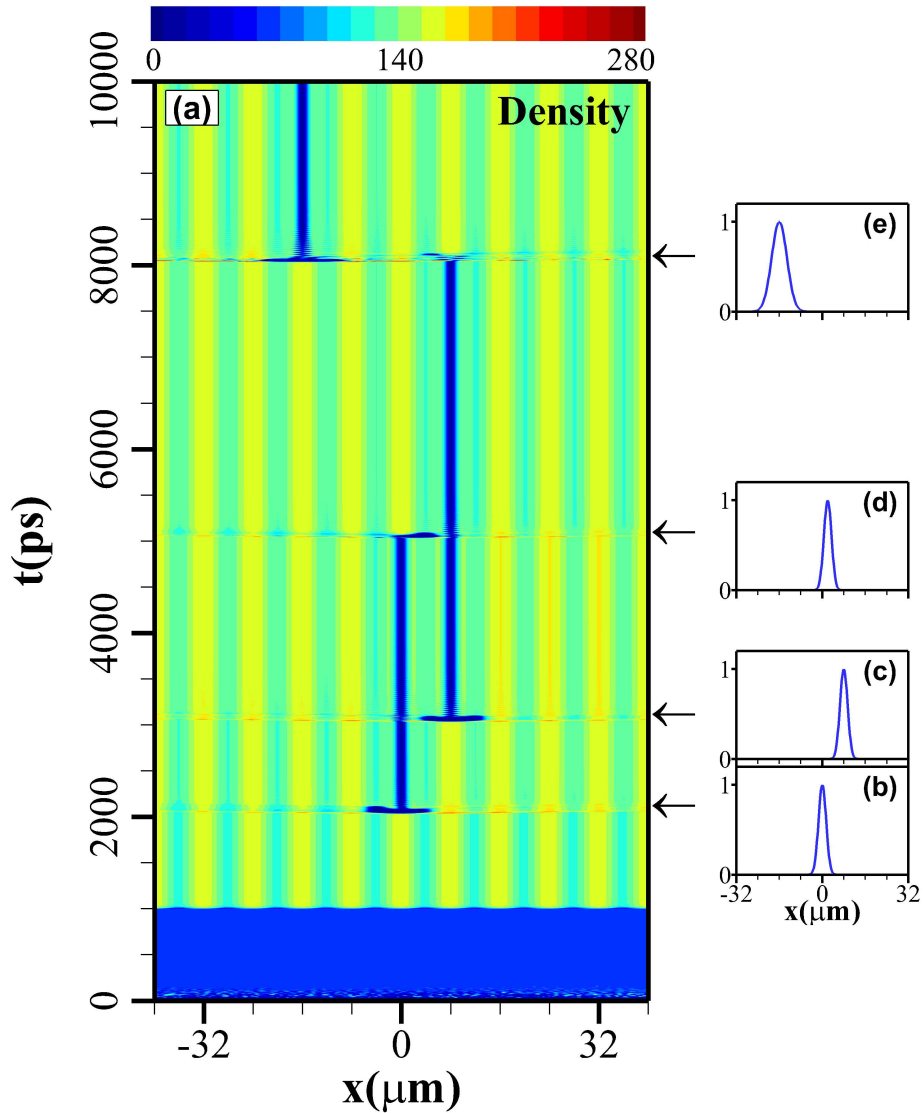

Fig. 3.7 Excitation and switch dynamics of dark solitons. (a) Time evolution of the density of condensates under homogeneous ($t < 1000$ ps) and periodic ($t \geq 1000$ ps and $P_0 = 32$ ps$^{-1}\mu$m^{-2}) pumps. (b)-(e) Profiles of coherent pulses for creating or annihilating dark solitons launched at different time and spatial points for (b) $x = 0$ μm, (c) $x = 8$ μm, (d) $x = 2$ μm, and (e) $x = -16$ μm. From [185].

hundreds of picoseconds later, another coherent homogeneous plane wave is launched on top of the sample and interferes with the first plane wave forming a periodic pump and exciting

simultaneously the periodically modulated solution [$1000 \leq t < 2000$ ps in Fig. 3.7(a)]. The pure periodic solution is regarded as a density background for the generation of dark solitons.

After the formation of the periodic solution, a normal-incident coherent pulse, represented by E_c in Eq. (2.29), 3 μm width [Fig. 3.7(b)] and 80 ps duration, is used to create a dark soliton. It is known that a normal incident coherent pulse with Gaussian shape suffers a sudden depletion at the center of injection and forms a ring shape because of the outgoing propagation of condensates [186]. One can see that a minimum density is excited at around $x = 0$ [$t = 2000$ ps in Fig. 3.7(a)] after the injection of the coherent pulse. At the same time, the continuous phase is cut off and a phase dislocation (π phase jump) is formed so that a dark soliton is created. Later, another dark soliton is created using the same method in a neighboring pump valley [$3000 < t < 5000$ ps in Fig. 3.7(a)]. Hence, the whole pump valleys can be excited to the dark soliton state using this method.

Due to the fact that dark solitons can only survive in pump valleys, if the same coherent pulse is launched into the middle of a pump peak (for example, $x = 4$ μm) it can annihilate both neighboring dark solitons formed at $x = 0$ μm and $x = 8$ μm because the condensates propagate symmetrically in both directions. However, if the coherent pulse is launched close to one of them [$x = 2$ μm in Fig. 3.7(d)] the nearest ($x = 0$ μm) dark soliton is destroyed and the other ($x = 8$ μm) survives as shown in Fig. 3.7(a) at $5000 < t < 8000$ ps. This is because the reservoir peak at $x = 4$ μm hinders the propagation of condensates along $x > 4$ μm.

It is worth noting that a broader coherent pulse, 6 μm width [Fig. 3.7(e)] and 50 ps duration, can be used to switch off a dark soliton in a more distant pump valley. After the injection of the broader pulse [$t > 8000$ ps in Fig. 3.7(b)], the dark soliton at position $x = 8\mu$m is annihilated because of the stronger energy propagation of condensates. Simultaneously, a new dark soliton forms in the pump valley where the broad pulse pump was injected. Therefore, a narrow coherent pulse can be used to annihilate any targeted single dark soliton, while a broader coherent pulse can be used to simultaneously annihilate several surrounding dark solitons. The control demonstrated is very robust and in particular is not sensitive to the phase of the applied light pulses, nor does it require precise tuning of the pulse frequency.

3.2.2 Manipulation of vortices

As mentioned in Sec. 3.13 a 2D homogeneous pump supports turbulent vortices due to the initial white noise according to the Kibble-Zurek theory. To stabilize the vortices, we investigate the dynamics of condensates under a 2D lattice pump formed by four coherent plane waves as introduced in Fig. 3.4(c). The 2D periodic pump can be written as

$$P(x,y) = P_0 \left[\sin^2 \left(\frac{\pi x}{d} \right) + \sin^2 \left(\frac{\pi x}{d} \right) \right], \tag{3.23}$$

where $d = 8$ μm is the lattice constant. Under the excitation of a lattice pump, two kinds
of vortices are generated, as shown in Figs. 3.8(a) and 3.8(b). One vortex type resides in
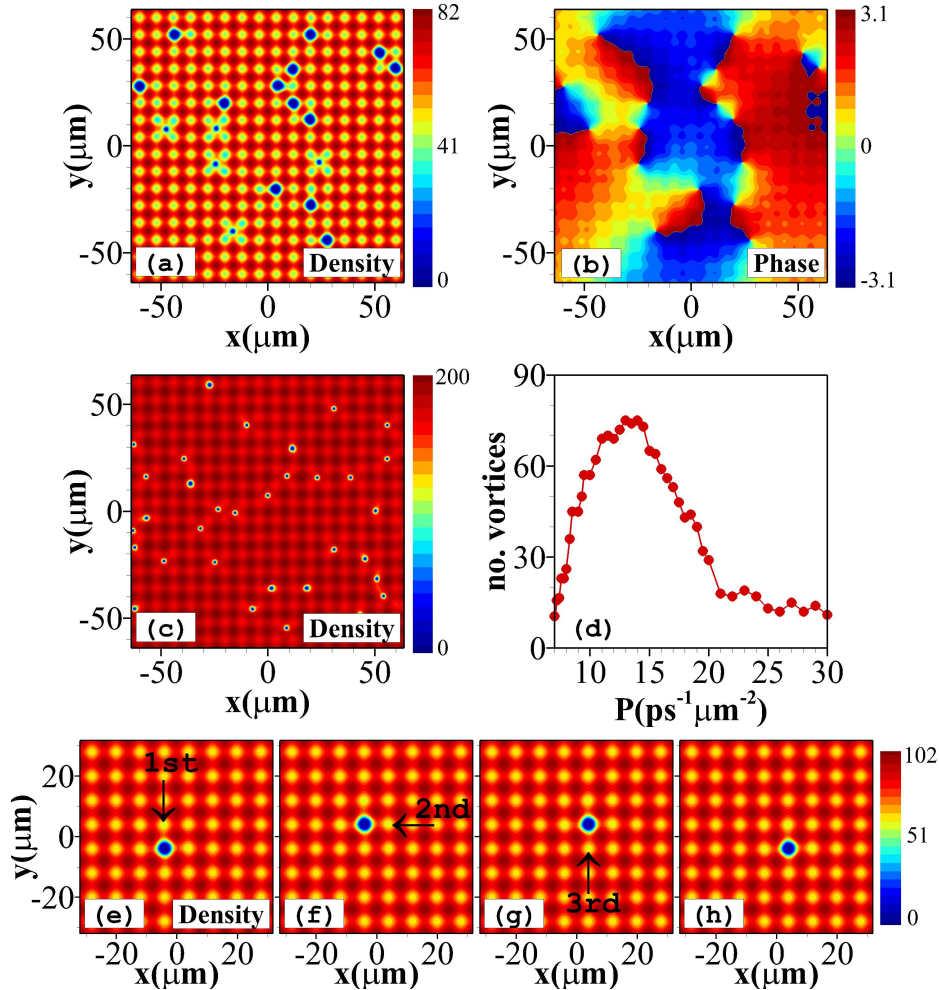the pump valleys and the other, which is larger in size, is found at the pump peaks. As

Fig. 3.8 Vortices and coherent control. Distributions of (a) density and (b) phase of conden-
sates under 2D lattice pumps at $P_0 = 8$ ps$^{-1}\mu$m^{-2} with initial noise. (c) Density distribution
of condensates at $P_0 = 20$ ps$^{-1}\mu$m^{-2}. (d) Dependence of vortex number on pump intensity
with initial noise. (e)-(h) Manipulation of a vortex by a sequence of four coherent pulses at
$P_0 = 10$ ps$^{-1}\mu$m^{-2}. Snapshots of the density profile are shown at (e) $t = 400$ ps, (f) $t = 800$
ps, (g) $t = 1200$ ps, and (h) $t = 1400$ ps. Arrows show the target moving cells. From [185].

before, these vortices are formed due to the initial white noise. Although their distribution is
irregular, they are all trapped in the center of their corresponding lattices and do not move.
The total number of vortices increases [Fig. 3.8(d)] as the pump intensity grows. However,
once the pump power becomes sufficiently large, the background periodic solution becomes

closer to homogeneous and the size of the vortices reduces [Fig. 3.8(c)]. In addition, at these high pump powers the lattice becomes weakly trapping and the vortices are able to travel to other lattice sites. In this condition, vortices begin to move out of their initial lattice sites and interact with others. A vortex and an antivortex attract each other and annihilate when they are too close, which is similar to the vortex dynamics in the homogeneous background. This is the reason why the number of vortices decreases sharply at very high pump powers ($P_0 > 14$ ps$^{-1}\mu$m^{-2}). The number of vortices is counted when the polariton and reservoir density achieves a steady state. When $P_0 > 21$ ps$^{-1}\mu$m^{-2} the contrast of background periodic solutions is almost constant, which leads to the number of vortices decreasing slowly and approaching a constant. In this region the vortices are far away from each other so that their interactions are very weak, or they are in a dynamic balance due to the repulsive interactions between the same charged vortices.

Unlike the creation and annihilation dynamics of dark solitons by coherent pulses in the 1D case, it is very difficult to create a vortex (2D phase defect) in the 2D periodic solutions using a coherent pulse. The reason is that a coherent pulse can generate a dark hole of density as studied in Ref. [186], but it is very difficult to reconfigure the 2D homogeneous phase in a short time. For the same reason, a coherent pulse cannot be used to switch off any vortices. A coherent pulse, however, is able to translate a vortex from its current cell to one of its neighboring cells as shown in Figs. 3.8(e)-3.8(h). Here, we use four identical coherent pulses, 3 μm width [Fig. 3.7(e)] and 80 ps duration, to move a vortex from its original cell and after a number of steps return to this cell. A coherent pulse creates a density hole, resulting in a decrease in the surrounding density, which opens one side of the lattice used for fixing the vortex. The vortex then escapes from its current site through the density gap, so the phase defect moves out of its own lattice and into the neighbouring lattice. Therefore, if one wants to move a vortex to a specified neighbouring lattice, thereby guiding the vortex. This method can be used to manipulate vortices from irregular to desired regular distributions. Also, a coherent pulse can be used to annihilate a vortex-antivortex pair by moving them to the same lattice site.

If one assumes that the 2D periodic pump is strip-like, then the pump can be written as

$$P(x,y) = P_0 \sin^2\left(\frac{\pi x}{8}\right), \qquad (3.24)$$

the pump along the y direction is homogeneous and $d = 8$ μm is the lattice constant along the x direction. Its distribution is shown in Fig. 3.4(a). There are also two kind of vortices [Figs. 3.9(a) and 3.9(b)] similar to those introduced in Fig. 3.8 under the lattice pumps, but they move freely along the y direction without any obstacle.

Of important is that the two kinds of vortices are not circularly shaped but rather, ellip-
tically shaped due to the limit along only one direction. The free moving dynamics along
the homogeneous direction can be used to incoherently control the motion of vortices. For
example, two fixed vortices are created by a 2D lattice pump [$t < 500$ ps in Fig. 3.9(c)].
Switching off the two coherent plane waves of the pump along y direction, results in the
periodic pump switching from the lattice to the strips [$500 \leq t \leq 1000$ ps in Fig. 3.9(c)]. The
vortices begin to move along the y direction. Switching the two coherent plane waves of
the pump back on again [$t > 1000$ ps in Fig. 3.9(c)], the lattice is reformed and the vortices
are fixed to their closest lattice sites. One can also switch off the two coherent plane waves
of the lattice pump along the x direction to horizontally move the vortices. However, the
direction of movement (forward or backward) and the velocity of the vortices are uncertain.
This is because the dynamics are influenced by the phase distributions and the interactions or
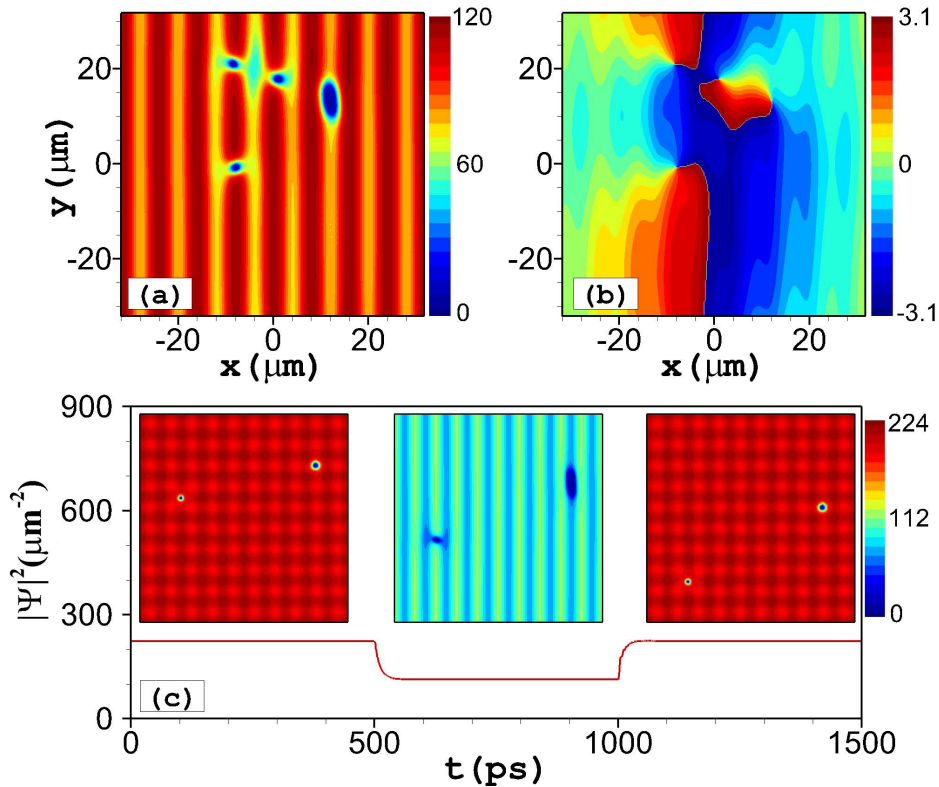separation between vortices.

Fig. 3.9 Vortices and incoherent control. Distributions of (a) density and (b) phase of
condensates under a 2D strip-like pump at $P_0 = 23$ ps$^{-1}\mu$m^{-2} with initial noise. (c) Time
evolution of peak density of condensates at $P_0 = 22$ ps$^{-1}\mu$m^{-2} for the manipulation of
vortices by switching the excitation between lattice and strip-like pumps. The inserts are the
density distributions of polaritons at each platform. Adapted from [185].

3.3   Chapter summary and concluding remarks

In this chapter, the method for seeking stationary solutions of the GPE and a coupled reservoir equation is introduced based on Newton's iteration method. Furthermore, the stability of the solutions are analyzed by adding a perturbation into the stationary solutions. Under homogeneous excitation, HSs are formed and stable when the system exhibits defocusing nonlinearity. The MI appears when the pump intensity is just above the condensation threshold, where the effective nonlinearity is focusing. In the MI region, the modulated patterns are not periodic and move irregularly due to the influence of the incoherent reservoir. Above the MI region, phase dislocations also can survive in analogy to the Kibble-Zurek theory, such that turbulent vortices can be found that become spiralling waves. At pump intensities far above the MI threshold, collective vortices are found. They interact with each other and annihilate until reaching a dynamic equilibrium. When the pump intensity is too strong, no vortex survive in the nonequilibrium polariton condensates.

To stabilize the turbulent vortices or dark solitons, a modulated periodic pump is introduced to this model. Two (or four) coherent plane waves can create a 1D (2D strip-like) or 2D lattice periodic pump which generates a similar periodic reservoir. The periodic reservoir, on the one hand, can limit the propagation of condensates, which is similar to a potential and can support stable 1D phase defects (dark solitons). The stabilization of dark solitons by periodic potentials has also been demonstrated in atomic condensates [187]. On the other hand, the periodic reservoir can also generate a periodic solution which is close to a homogeneous distribution. Therefore, the pure periodic solution can be regarded as a background. In the 1D case, dark solitons can be excited from initial white noise and the number of occupied pump valley sites is related to the loss rate and effective mass of condensates, as well as the pump intensity. A coherent pulse is used to create or annihilate any specified dark soliton. In the 2D case, two kinds of vortices are found in both the pump valleys and peaks, and it is shown that they can be manipulated to a specified lattice by a coherent pulse. They can also be controlled by switching the periodic pumps between lattice and strips, because the strip-like periodic pumps can support moving vortices along the uniform directions.

Chapter 4

Vortices under ring-shaped pumps

The excitation dynamics of condensates under homogeneous pumps is discussed in Chapter 3. In this condition, a turbulent state of vortices is formed due to the condensate-reservoir feedback. A periodic pump, however, can stabilize the free motion of vortices, which indicates that the quasi-localized pump can be regarded as a periodic potential and strongly influence the dynamics of condensates. In this chapter, we consider a localized pump, a ring-shaped pump, for excitation. Under a localized pump, it is shown that a localized reservoir with a similar shape to that of the pump is generated. The localized reservoir strongly influences the density distribution of condensates. Therefore, a ring-shaped pump leads to the generation of a ring-shaped reservoir which can be regarded as an internal potential limiting most of the condensates inside the reservoir ring. Generally speaking, due to the pump having the minimum intensity in the middle, the density of the condensates in the center of the pump is also a minimum, such that a ring with a topological charge, known as a crater-shaped vortex, is formed. In this chapter, we study in detail the existence and stability of this kind of vortices, and their topological charge. It is found that the sign of the topological charge representing the rotation directions, clockwise or anticlockwise, is either "+" or "-" due to the radial symmetry of the system and the random initial noise [123].

In this chapter, we find two simple methods to control the topological charge of a vortex. The first method is that one can use an elliptical incoherent pump to create an elliptical solution of condensates, which breaks the radial symmetry of the system. The later formed vortex has a certain topological charge. Similarly, for a already formed vortex with a vortex that has already been formed, with a certain charge, an elliptically incoherent pulse can be used to switch the topological charge to its opposite sign. The switching dynamics strongly depend on the ellipticity of the pulse and the position of the pulse in relation to the target vortex. This method, however, mainly concentrates on a single vortex. In this chapter, vortex-vortex control is investigated as a means to achieve multi-vortex control. Two or more

closed vortices form a phase-locked state, resulting in the topological charge control of a vortex chain containing many vortices.
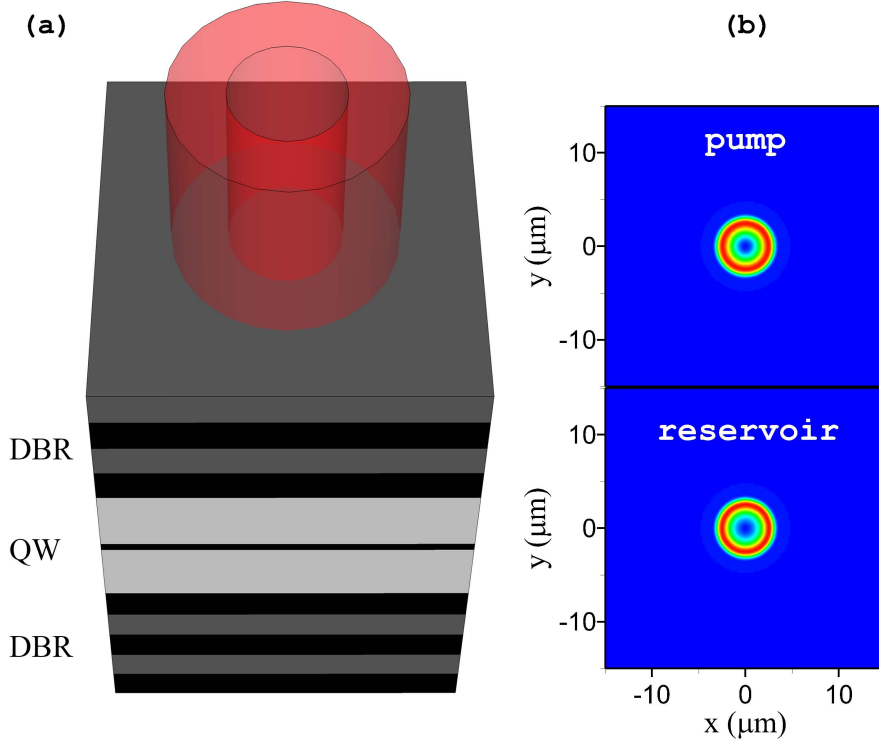
4.1 Steady-state solutions

Fig. 4.1 (a) Sketch of a semiconductor microcavity with a quantum well (QW) sandwiched between two DBRs. A ring-shaped incoherent pump creates a vortex solution of condensates. (b) Distribution of a ring-shaped pump (upper) and the corresponding reservoir density (lower).

The dynamics of condensates in uniform samples is described by the coupled GP model, Eqs. (2.29) and (2.30), with $V = 0$. Here, we investigate the existence of topological solutions with different orbital angular momentum under a ring-shaped incoherent excitation. Note that a small-size ring pump, with the radius smaller or comparable to the thermal de-Broglie wavelength, is expected to sustain a stable vortex solution. For larger ring radii a condensate can break down to a pattern with many lobes, representing two phase-locked standing waves [188]. We consider a ring-shaped optical pump having the following spatial profile:

$$P(r) = P_{\mathrm{ring}}(r) = P_0 \left[1 - e^{-\left(\frac{r}{w}\right)^2} \right] e^{-\left(\frac{r}{w}\right)^{10}}, \tag{4.1}$$

where P_0 is the intensity of the pump and the radius of the pump is controlled by w. The system that our model simulates is presented in Fig. 4.1(a). The ring-shaped incoherent pump generates a reservoir cloud which has a similar profile to that of the pump [Fig. 4.1(b)]. Such a pump configuration can sustain vortex solutions with different topological charges, which are strongly related to the radius of the pump ring as shown in Figs. 4.2. The parameters in the model (2.29) and (2.30) in this chapter are: $m = 10^{-4}m_e$, $\gamma_c = 0.33$ ps$^{-1}\mu$m^2, $\gamma_r = 1.5\gamma_c$, $g_c = 6 \times 10^{-3}$ meVμm^2, $g_r = 2g_c$, and $R = 0.01$ ps$^{-1}\mu$m^2 taken from [119].
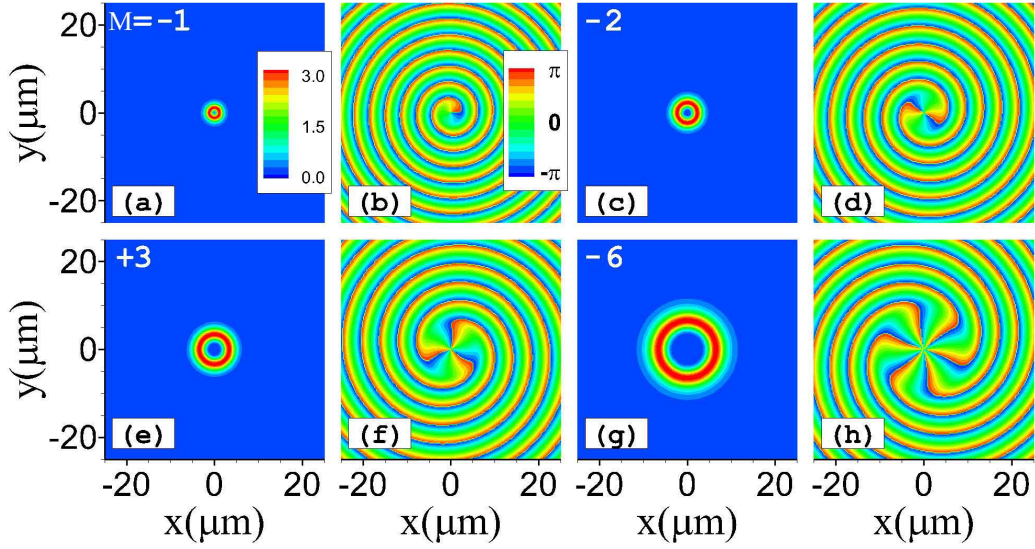

Fig. 4.2 Density distributions of stable vortices supported by incoherent ring-shaped pumps with different diameters. Distributions of density (a,c,e,g) and phase (b,d,f,h) of vortices for (a,b) $w = 3$ μm and $P_0 = 125$ ps$^{-1}\mu$m^{-2}, (c,d) $w = 5$ μm and $P_0 = 110$ ps$^{-1}\mu$m^{-2}, (e,f) $w = 7$ μm and $P_0 = 95$ ps$^{-1}\mu$m^{-2}, and (g,h) $w = 12$ μm and $P_0 = 65$ ps$^{-1}\mu$m^{-2}. Adapted from [189].

Figure 4.3(a) shows three prominent examples of the bifurcation branches of the vortices with winding numbers $|M| = 1, 2, 3$. The size of the vortex depends on the winding number $|M|$ [Figs. 4.2 and 4.3(d)] and is also proportional to the effective healing length of the system, which can be properly modified for the case of nonequilibrium dissipative system. It is obvious from Fig. 4.3(b) that the vortex is confined in the reservoir such that the radius of the vortex is strongly related to the radius of the pump. Therefore the radius of the ring-shaped pump is a crucial parameter, since its spatial overlap with the vortex determines both the vortex stability and the excitation threshold. The nonlinear interaction between polaritons and their interaction with the reservoir results in a blue-shift of the vortex eigenfrequencies for increasing pump intensity [Fig. 4.3(c)].

A standard linear stability analysis has been performed to prove the stability of the solutions using the method introduced in Chapter 3. It is found that the vortices with $|M| = 1$ are stable in a broad interval of pump intensities, at least, for the optimal choice of the pump ring radius [Fig. 4.3(a)]. It is worth noting that when the pump intensity is very large almost all condensates are trapped in the center of the reservoir, resulting in a ring-shaped potential barrier, forming a fundamental mode. The vortices with higher winding numbers, for example, $|M| = 2$ and $|M| = 3$, may become unstable for strong enough pump intensity even for the optimized pump size. In general the stability interval of the vortices decreases for larger values of their orbital angular momentum $|M|$, and it always exists under smaller pump intensity close to their excitation thresholds.
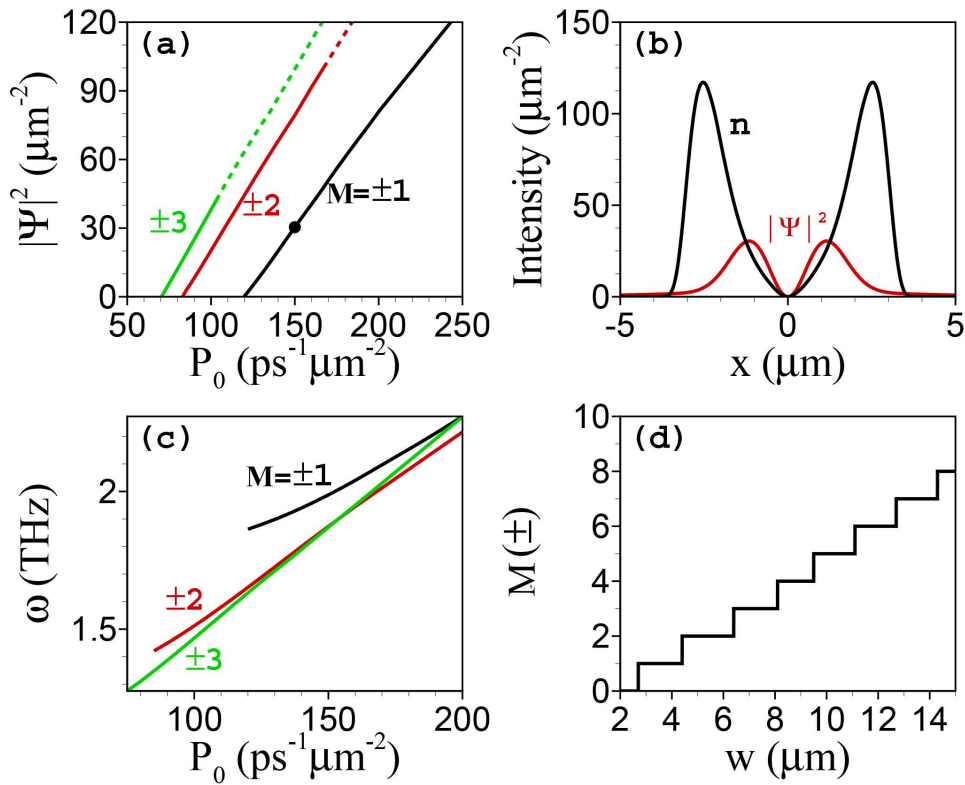

Fig. 4.3 (a) Peak density of condensates versus the pump intensity of the steady-state vortices with charges $M = \pm 1$, ± 2, and ± 3 supported by the ring-shaped pumps with radii $w = 3$, $w = 5$, and $w = 7$ μm, respectively. Dashed lines represent unstable solutions, while solid lines represent stable solutions. (b) One-dimensional polariton-density, $|\Psi|^2$, and reservoir density, n, profiles for the fundamental vortex depicted by the thick dot in (a). (c) Eigenfrequencies versus pump intensity for the vortices shown in (a). (d) The winding numbers of spontaneously formed vortices versus the radii of the ring-shaped pump modelled in the vicinity of their excitation thresholds. From [189].

To study the excitation and formation dynamics of vortices, we performed extensive numerical calculations starting from an initial small-amplitude noise for the pumps with different radii. Figure 4.3(d) illustrates the effect that changing the radius of the pump ring has on the topological charge of the spontaneously formed solutions. For very small radii ($w < 3~\mu$m) the ring-shaped pump also supports a nonvortex fundamental mode with $M = 0$, similar to the results in Ref. [94, 190]. It is also found that the topological charge jumps to higher integer values for increasing the ring-pump radius. However, in a small interval of the radius of the pump, the solutions have the same topological charge, but different radii.

4.2 Vortex control by elliptical pumps

Note that, since the total angular momentum of the system is absent, the sign of the topological charge has been generated randomly during the spontaneous creation of vortices [Fig. 4.2]. To control the rotation directions of vortices, we discuss the possibility of breaking the radial symmetry of the system through the addition of an elliptically shaped nonresonant beam [Fig. 4.4(a)]. In the presence of both elliptical and ring-shaped beams, the excitation pump can be written

$$P(x,y,t) = P_{\text{ring}}(x,y,t) + P_e e^{-\left(\frac{x^2}{w_x^2} + \frac{y^2}{w_y^2}\right)}, \tag{4.2}$$

where w_x and w_y represent the lengths of the main elliptical axes and the ellipticity parameter defined as $E = w_x/w_y$. After a short time (about several hundreds picoseconds) of excitation, an elliptical localization is formed [Figs. 4.4(b)-4.4(d)] with smooth background. Simultaneously, an elliptical phase, which progresses from the center, is generated [Figs. 4.4(b)-4.4(d)]. Next, a ring-shaped pump is used to generate a vortex around the elliptical pump. The vortex that later forms is strongly influenced by the elliptical solution if they are not too far away from each other. In this thesis, we define a vortex with clockwise rotation as having a negative "-" charge, while a vortex with anticlockwise rotation has a positive "+" charge.

Slightly above the condensation threshold the elliptical solution emits outgoing waves propagating to the position of the ring-shaped pump [Figs. 4.4(b)-4.4(d)]. It is essential that the elliptical wave breaks the symmetry and results in spontaneous formation of the vortex with predefined sign, even in the presence of initial small amplitude noise. It is found that the topological charges of vortex solutions formed under the same pump in the regions "I" and "II" [Fig. 4.4(a)] always have opposite signs. However, for different pumps, the vortices may rotate inversely, even if they are formed in the same region. For example, in the region "I" ("II"), the vortices rotate clockwise (anticlockwise) for $|M| = 1$ [Fig. 4.4(b)] and $|M| = 2$

[Fig. 4.4(c)], while the vortices rotate anticlockwise (clockwise) for $|M| = 3$ [Fig. 4.4(d)]. So, elliptical pumping can be used to change the signs of the vortex charges by changing the specific region that is injected using a fixed ring-shaped pump. An easy way to control the vortices is shown in Fig. 4.4(a). One can keep the position of the ring-shaped pump fixed, and change the elliptical direction of the control pump to realize control of the vortices. Through this mechanism, one can rotate the ellipse of the control pump, as shown in Fig. 4.4(a), to control the signs of vortex charges that will later form.
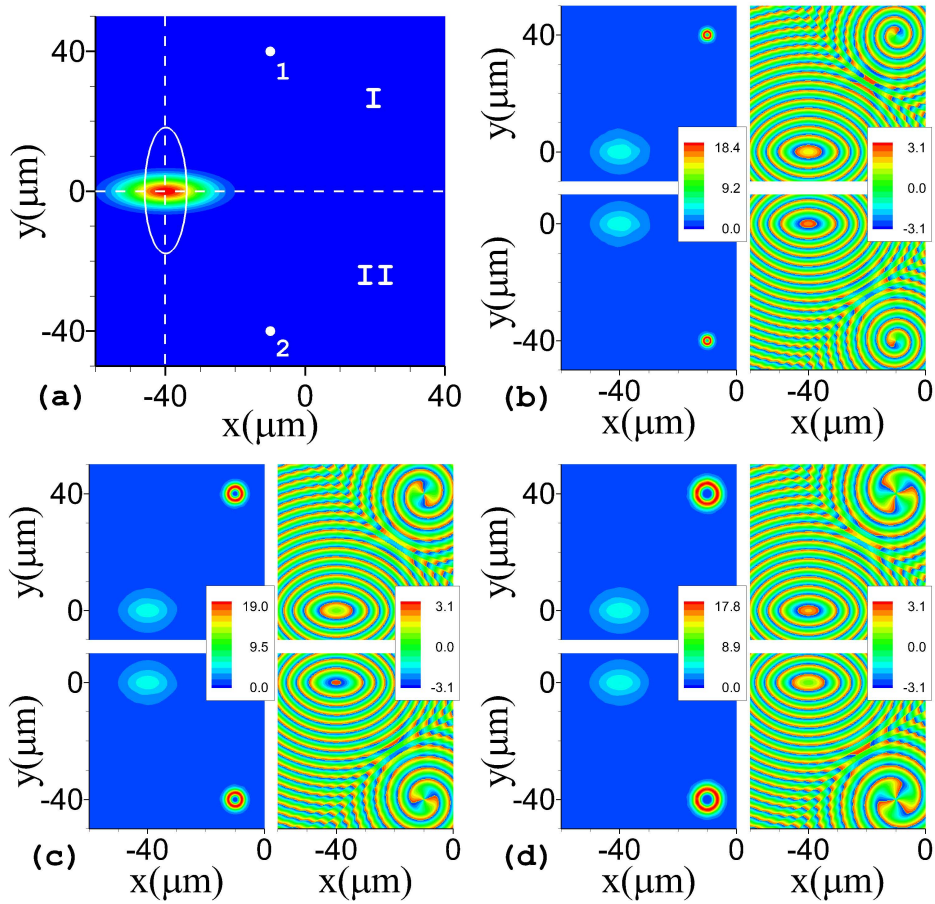

Fig. 4.4 (a) Intensity distribution of an elliptical pump. Points "1" and "2" in the regions "I" and "II" represent, respectively, the injected positions of ring-shaped pumps. (b)-(d) Density and phase distributions of predefined formation of the vortices in the vicinity of the elliptical control beam with the $P_e = 40$ ps$^{-1}\mu$m^{-2}, $E = 2$. The vortices with the positive ($M = +1$) and negative ($M = -1$) charges form in the upper and lower right corners, respectively, through the use of different ring-shaped pumps for (b) $P_0 = 140$ ps$^{-1}\mu$m^{-2} and $w = 3$ μm, (c) $P_0 = 100$ ps$^{-1}\mu$m^{-2} and $w = 5$ μm, and (d) $P_0 = 85$ ps$^{-1}\mu$m^{-2} and $w = 7$ μm. Adapted from [189].

We proceed with a systematic numerical analysis of the switching dynamics for a more realistic configuration. A control pulse is launched in close proximity to the vortex position instead of the CW elliptical pump. This control pulse is added to the pump in the right hand side of the rate equation for the reservoir in the following form:

$$P(x,y,t) = P_{\text{ring}}(x,y,t) + P_e e^{-\left(\frac{x^2}{w_x^2} + \frac{y^2}{w_y^2}\right)} e^{-\frac{t^2}{(\Delta\tau)^2}}, \tag{4.3}$$

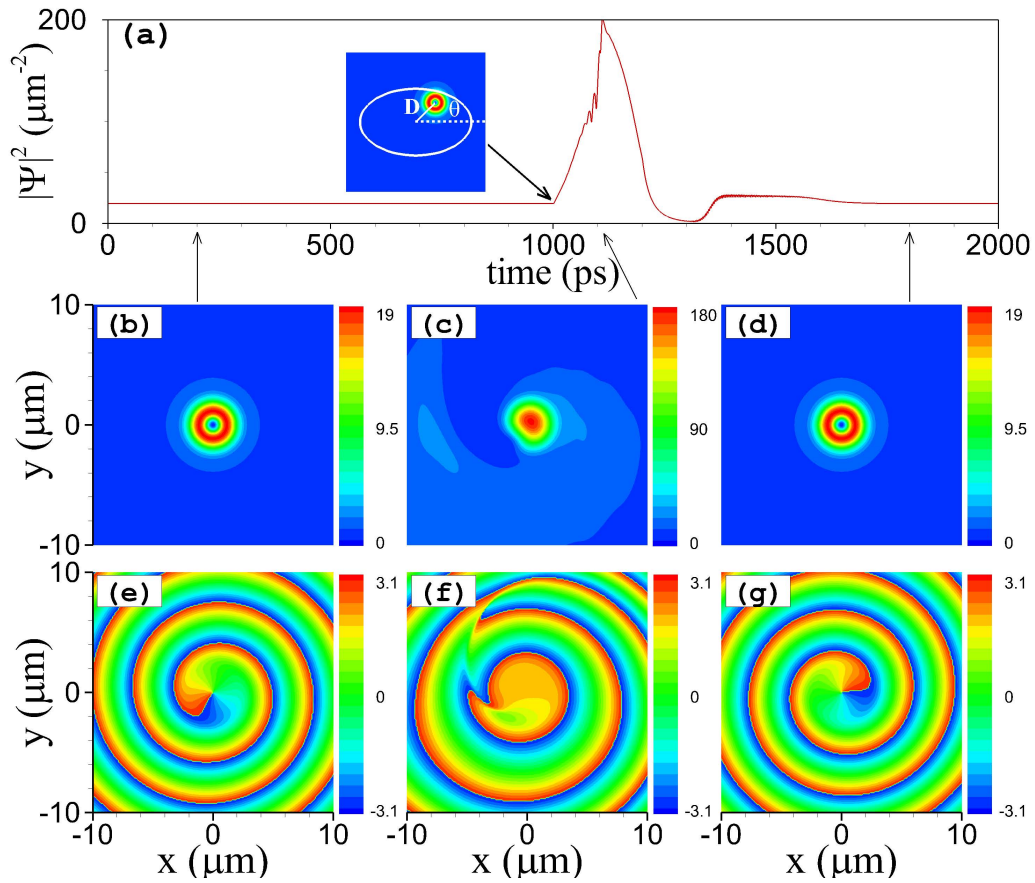where Δt represents the duration time of the pulse. Figure 4.5 shows an example of a desired

Fig. 4.5 (a) Time evolution of switching dynamics of a vortex from a positive charge $M = +1$ to a negative charge $M = -1$ through the use of an elliptical pulse with duration $\Delta\tau = 100$ ps, intensity $P_e = 50$ ps$^{-1}\mu$m^{-2} and $E = 2$. The vortex-pulse separation is $D = 5$ μm and the angle between the x-axis and the direction to the vortex is $\theta = \pi/4$. (b)-(d) Condensate density distributions at different time. (e)-(g) Phase profiles corresponding to (b)-(d), respectively. From [189].

switching of the charge of a fundamental vortex by a control pulse with a duration of 100 ps and elipticity $E = 2$. A positive charged vortex, $M = +1$, is forced to stop rotating [Figs.

4.5(c) and 4.5(f)] by the injection of an elliptical pulse close to the vortex [see the insert in Fig. 4.5(a)]. Under the influence of the elliptical pulse, a vortex with a negative charge, $M = -1$, is then formed.

The pulse intensity required for reliable switching depends on the parameters describing the shape and position of the control beam [Fig. 4.6]. The switching threshold converges to infinity $P_e \to \infty$ for a radially symmetric control beam ($E = 1$) since it cannot break the chirality of the system [Figs. 4.6(a) and 4.6(b)]. Therefore, for a fixed position of the
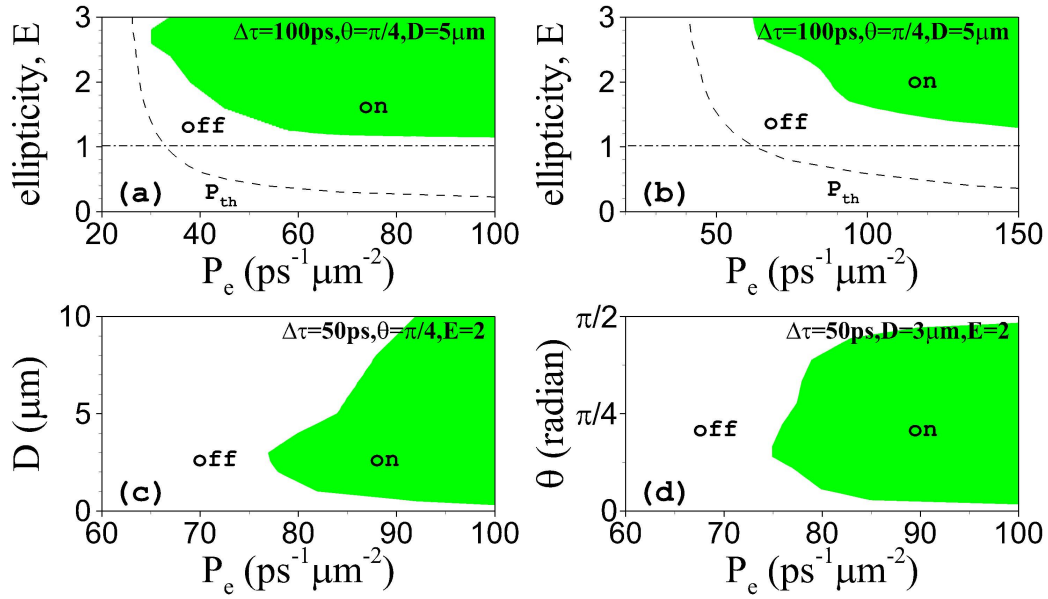

Fig. 4.6 Parameter domain (green shaded area) required for the reliable recharge of the vortex in the parameter plane of control beam intensity, P_e, and its elipticity, E. The control pulse parameters are $\Delta\tau = 100$ ps, $\theta = \pi/4$, $D = 5$ μm for (a) $w_y = 10$ μm and (b) $w_y = 5$ μm. (c) The parameters domain (shaded area) for reliable switching in a plane of control beam intensity, P_e, and the distance to the vortex position, D, for $\Delta\tau = 50$ ps. (d) The same as in (c) but in a plane of control beam intensity, P_e, and the angle between the x-axis and the direction to the vortex position, θ. Dashed lines depict the condensation threshold related to the elliptical pulse. From [189].

control pulse there is an optimal value of the ellipticity with a minimal value of the switching threshold. The relative position of the control pulse is related to the distance to the vortex position and the angle between the main axis of the elliptical pump (x direction) and the direction to the vortex. The distance between the control pulse and the ring-shaped pump that is holding the vortex is a crucial parameter. On the one hand, it is evident that the influence of the control pulse becomes weaker for a large separation due to the finite lifetime of polaritons. On the other hand, switching becomes less effective for a very short distance since the center of the elliptical pump possesses chirality. Thus, a competition between these two trends

gives an optimal distance between the control and ring-shaped beams, which is about $D \approx$ 2-3 μm and comparable to the radius of the ring-shaped pump, for the given set of parameters [Fig. 4.6(c)]. The switching threshold intensity depends also on the angle between the main axis of the elliptical control pulse (x direction) and the direction to the vortex position. For symmetry reasons switching is impossible for the high symmetry angles $\theta = n\pi/2$, where n is an integer [Fig. 4.6(d)]. Figure 4.6(d) shows that the optimal value of the angle is about $\theta = \pi/6$, for the given set of parameters. The presented dynamics of reliable charge reversal is not restricted to only the fundamental vortices ($|M| = 1$) but can be easily generalized to the vortices with higher winding numbers. It is worth noting that this method of control on vortex charges mainly focus on a single vortex.

4.3 Vortex-vortex control

To realize multi-vortex control, in this section phase-locked vortices are studied. If two ring-shaped pumps with the same profile are launched for the creation of vortices as illustrated in Fig. 4.7(a), two phase-locked vortices are formed. The reason is that apart from the two 2D parabolic potentials formed by the ring-shaped reservoirs, there is an additional quasi-1D parabolic potential between the two rings, and the width of the potential depends on the separation distance between the two pumps. It is experimentally and theoretically demonstrated that when the potential is narrow two phase-locked fundamental modes can be generated [91, 92]. There is an even number of small peaks between the two main peaks when their phase difference is π, while the same phase distribution between the two main peaks happens when the number of small peaks is odd. This property is similar to each of the quantum harmonic oscillator states in a parabolic potential. The number of small peaks are related to the separation distance between two pumps, or the width of the reservoir-induced potential. However, when the two pumps are far away from each other polaritons simultaneously occupy several of the lower simple harmonic oscillator (SHO) states, resulting in the complex temporal oscillations in real space [90].

The phase-locked state can also happen in vortices when they are separated by an appropriate distance. The phase-locked vortices are related to the separation distance between the ring-shaped pumps. The distance d represents the separation of vortex cores, namely, the centers of ring-shaped pumps. When the distance is very narrow, $d = 6$ μm for instance, as shown in Figs. 4.7(b) and 4.7(c), there are no smaller peaks (even number) seen between the two rings [Fig. 4.7(b)], so that the phase difference between the neighbouring peaks of the two vortex rings is π as marked by the black points in Fig. 4.7(c). In this condition, two vortices strongly interact with each other leading to density profiles that look more like

dipoles. Increasing the distance to $d = 15 \mu$m, the interaction between two vortices becomes weaker and the potential between two rings becomes broader. As a consequence, five smaller peaks (odd number) are formed between the two density rings as shown in Fig. 4.7(d), which results in the same phase distribution in the neighbouring peaks of the two vortex rings [see black points in Fig. 4.7(e)]. In other words, two vortices form a phase-locked vortex pair when they are in an appropriate distance. Here, we define that the 0-state (π-state) vortices indicate the phase difference is 0 (π) at the closest rings of vortices as marked by the black points in Fig. 4.7(c) (4.7(e)).
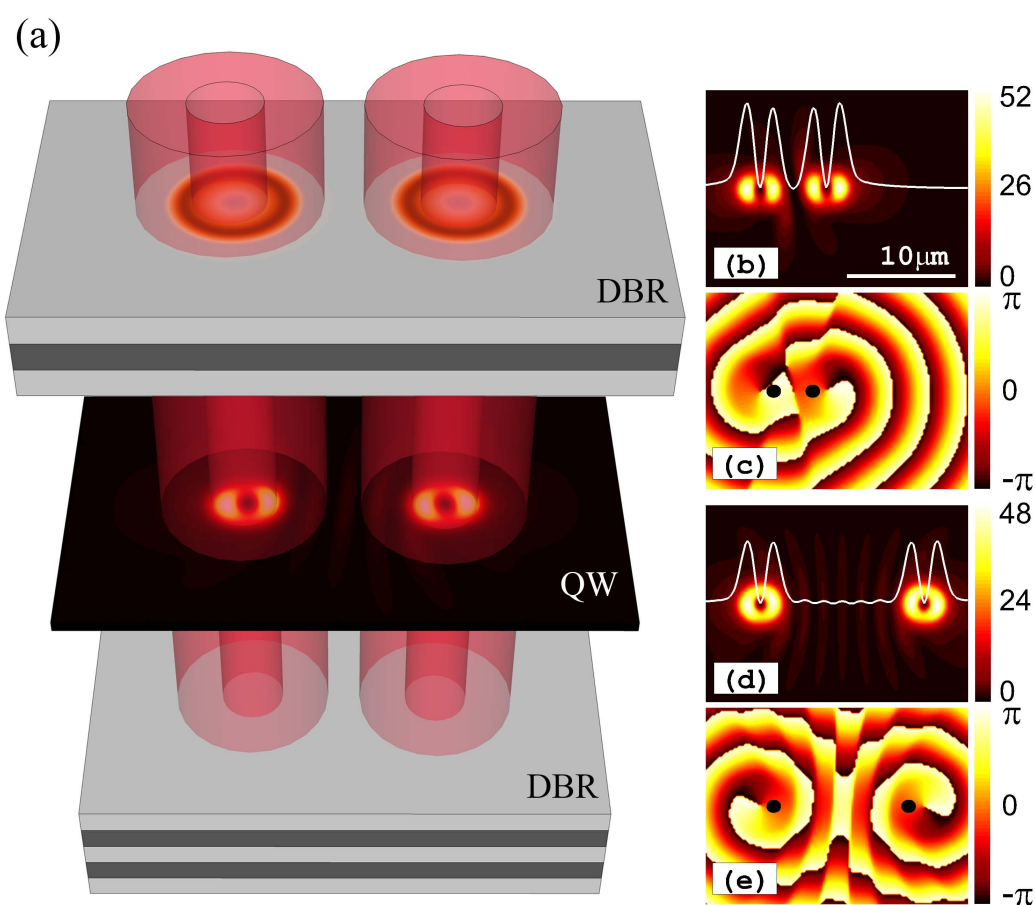

Fig. 4.7 (a) Sketch of a semiconductor microcavity under the excitation of two incoherent ring-shaped pumps. The microcavity containing a QW is sandwiched between two DBRs. Distributions of (b,d) density and (c,e) phase of two phase-locked vortices at (b,c) $d = 6 \mu$m and (d,e) $d = 15 \mu$m. White curves in (b,d) represent the 1D profiles of the density along the lines of vortex centers. Phase differences of vortices in (c,e) are counted in the region marked by the black points. From [191].

Figure 4.8 provides solid evidence that the phase difference, 0 or π, between two vortices changes alternatively as one slowly increases or decreases their separation distance. Here we fix a ring-shape pump and move another one to control the distance. Figure 4.8(a) shows the state transitions between the 0-state and the π-state when slowly increasing (red curve) and decreasing (blue curve) the distance between two pumps. It is worth noting that the two curves overlap for approximately half of this range, but there are still notable differences between them. For example, for $d = 12.2\ \mu$m in Fig. 4.8(a) there are two different stable
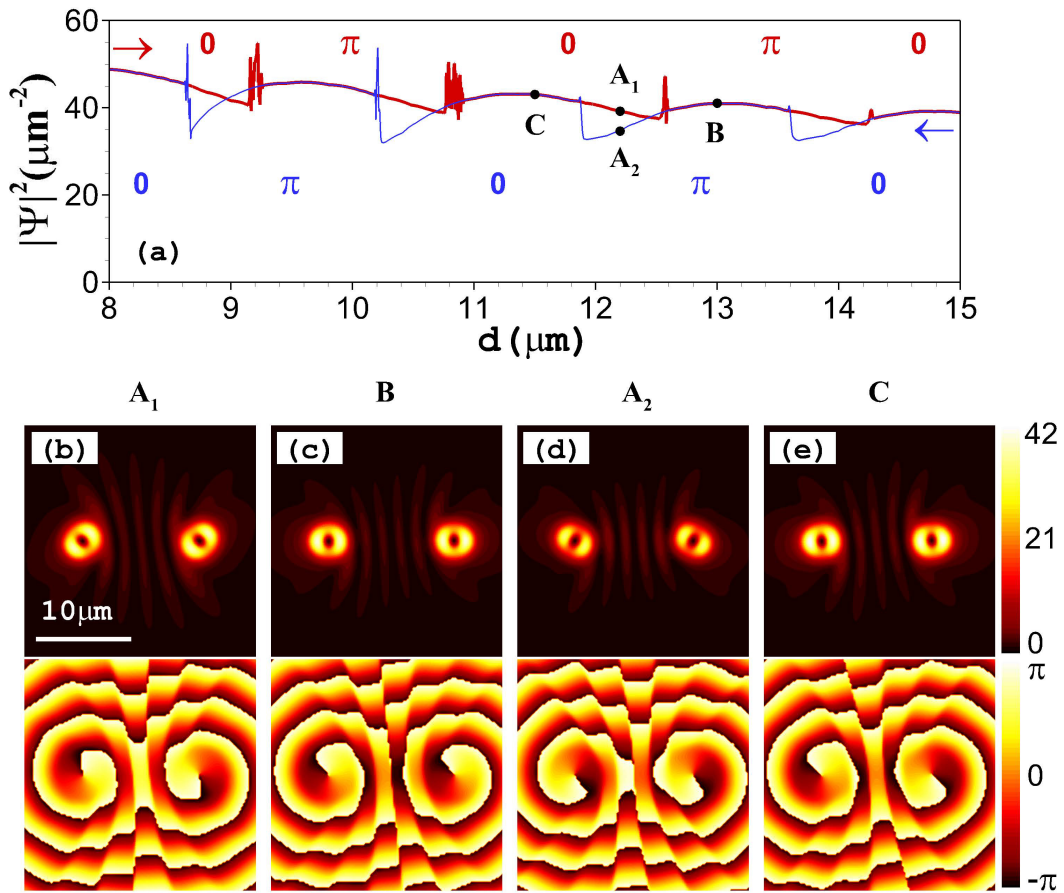

Fig. 4.8 (a) Peak density of two phase-locked vortices depending on their separation distances. Red curve represents the calculation by increasing the distance from $d = 8\ \mu$m to $d = 15\ \mu$m, while blue curve represents the calculation by decreasing the distance from $d = 15\ \mu$m to $d = 8\ \mu$m. (b-d) Profiles of density (upper row) and phase (lower row) of phase-locked vortices corresponding to the positions marked in (a).

states, known as bistability, due to different initial conditions. The A_1 state at $d = 12.2\ \mu$m is a 0-state vortex pair as shown in Fig. 4.8(b) which can be directly excited from initial noise or from the C state [Fig. 4.8(e)] by increasing the distance. When continuously increasing

the distance to the B state, $d = 13$ μm, the 0-state vortices switch to the π-state as shown in Fig. 4.8(c) and there is an intensity peak when the switching happens as shown in the red curve in Fig. 4.8(a). These π-state vortices, however, are still stable when the distance is decreased to $d = 12.2$ μm again, that is, the A_2 state [Fig. 4.8(d)]. When decreasing towards the C state, the vortices are switched back to the 0-state. Comparing the A_1 and the A_2 states it is found that the phase difference of the two vortices is different, but their topological charges are always the same because the distance is larger where the influence of the vortices to each other is already weak.

However, the bistability around $d = 9$ μm has different properties due to the strong interaction of two vortices when they are close to each other. In this region, the bistable state can have not only different phase-locked states, but also different topological charges. This means that when a pump moves from $d = 9$ μm to $d = 10$ μm and moves back again one of the vortices may switches to its opposite topological charged state. The switching in this region is uncertain, and will depend on the moving velocity of the ring-shaped pump. Note that the bistability interval distance is very narrow, less than 1 μm, in this model. These narrow intervals could be broadened if polaritons with larger lifetimes and smaller effective mass, because it has been demonstrated that the phase locked state depends not only on the separation between the condensed modes but also on the flow velocity of condensates [91].

Even though the phases of two vortices are locked as mentioned above, the two vortices can still have the same or opposite topological charges if simultaneously created by two ring-shaped pumps. For example, in Fig. 4.7(c) the two vortices have the same topological charge, however, these two vortices can also have opposite charges, which is similar to the phase profile in Fig. 4.9(f), because of the initial noise. Therefore, to control the topological charges of both 0-state and π-state phase-locked vortices is the main aim in this section. Here, we choose two typically phase-locked vortices: the 0-state vortices containing one small peak with the distance between the two pumps $d = 8$ μm as shown in Figs. 4.9(c) and 4.9(d) and the π-state vortices containing two small peaks with the distance $d = 10$ μm as shown in Figs. 4.9(e) and 4.9(f). Of, course, these two choices of the distance should avoid the bistability region.

First, we demonstrate the creation of phase-locked vortices with opposite topological charges. Under a ring-shaped pump, a vortex with $M = +1$ is formed [Figs. 4.9(a) and 4.9(b)]. The free propagation of condensates generates an outgoing radial velocity ($v_\parallel$) component, and the vorticity of condensates generates a tangential rotation-induced velocity ($v_\perp$) component as shown in Fig. 4.9(a). The two components of velocity satisfy the relations

$$v_\parallel = \frac{\hbar k}{m}, \tag{4.4}$$

$$v_\perp = \omega r' \tag{4.5}$$

where k is the wavenumber of polaritons, ω is the angular frequency of the vortex, and r' is the radius of the vortex. The values of these parameters can be extracted from Fig. 4.9(a) and the insert. One finds $\omega \simeq 2.0$ THz and $k \simeq 1.0$ μm^{-1} when considering the peak density of condensates in the reciprocal space, and $r' = 1.15$ μm. One can then determine that $v_\parallel \simeq 1.16$ μm/ps and $v_\perp \simeq 2.3$ μm/ps, which are comparable, so that polaritons flow with the resultant velocity $v = \sqrt{v_\parallel^2 + v_\perp^2}$ along the direction marked by the red arrow in Fig. 4.9(a). The energy flow of condensates breaks the radial symmetry of the background,
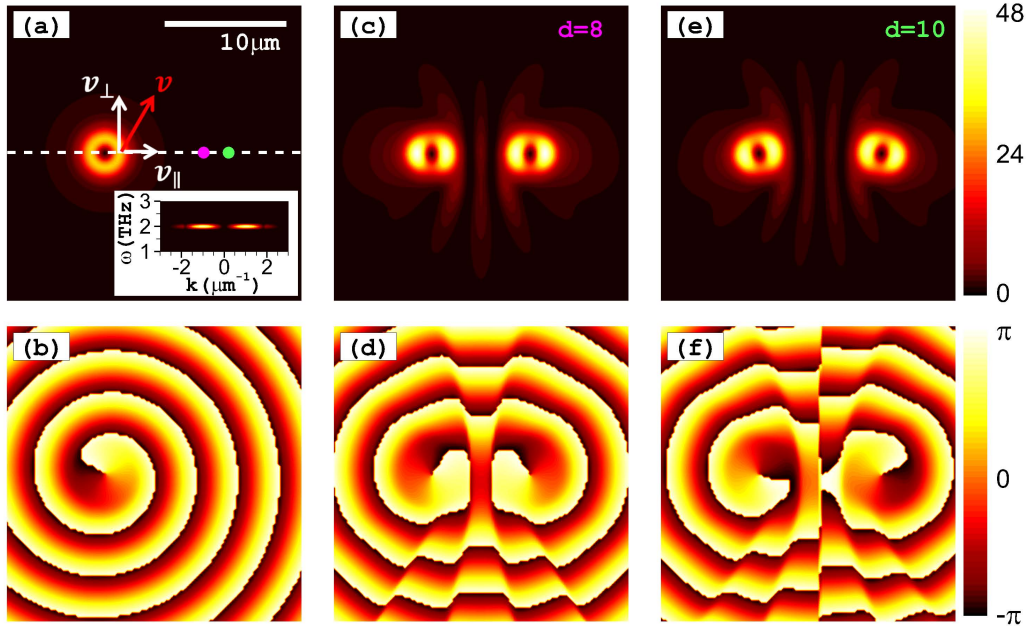

Fig. 4.9 Distributions of density (upper row) and their corresponding phase (lower row) of vortices. (a,b) A single vortex solution. The insert in (a) is the time-resolved profile along the dashed line. The arrows in (a) represent the velocity (v) of polaritons and its radial ($v_\parallel$) and tangential rotation-induced ($v_\perp$) components. The two points in (a) indicate the positions of the second ring-shaped pumps with $d = 8$ μm for the pink one and $d = 10$ μm for the green one. (c,d) Two phase-locked vortices at $d = 8$ μm. (e,f) Two phase-locked vortices at $d = 10$ μm. From [191].

which affects the surrounding vortices that will later form. Due to the flow direction, the second vortex generated nearby always rotates in a clockwise direction with the topological charge $M = -1$ for both 0-state [Figs. 4.9(c) and 4.9(d)] and π-state [Figs. 4.9(e) and 4.9(f)] vortices. This means that the second formed vortex always has the opposite topological charge when compared to the first one because of the radial symmetry breaking caused by

the time delay. In this model, the time delay should be longer than 200 ps, which is the formation time of the first vortex.
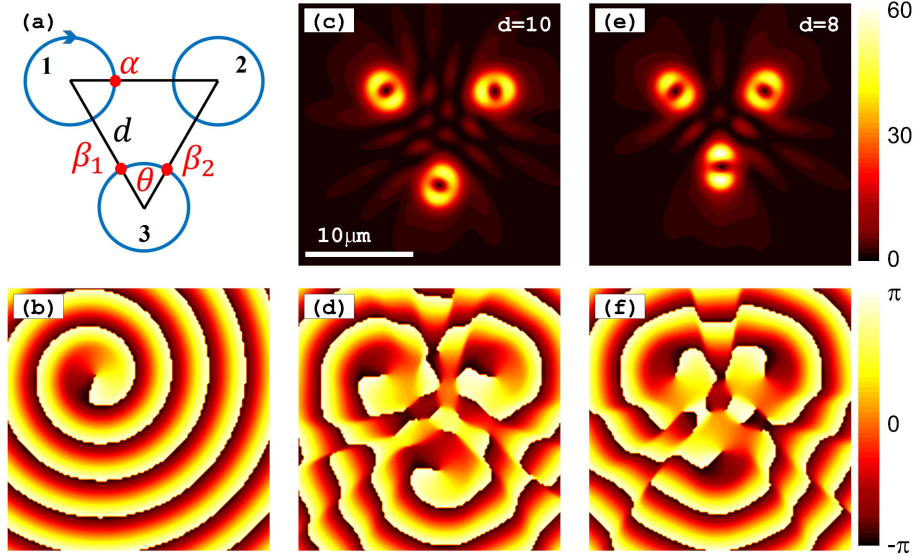

Fig. 4.10 (a) Sketch of three phase-locked vortices with the same distance, d, between them. α, β_1, and β_2 represent the phases at the intersections (red points) of the solution circles and the standard triangle. $\theta = \pi/3$ is the internal angle of the standard triangle. (b) Phase distribution of a single vortex. Distributions of (c) density and (d) phase of three phase-locked vortices at $d = 10\,\mu$m. Distributions of (e) density and (f) phase of three phase-locked vortices at $d = 8\,\mu$m. From [191].

Next, we consider three phase-locked vortices to investigate the generation of the same charged vortices. Three ring-shaped pumps are spatially arranged in the structure shown in Fig. 4.10(a) where their centers form an equilateral triangle. To analyze the relation between three topological charges, we keep the topological charge of the first vortex $M \equiv -1$, marked by the arrow in Fig. 4.10(a). Below, we analyze separately the 0-state and π-state vortices.

(i) For the π-state vortices, if the second vortex has the topological charge $M = -1$, the phase at β_1 and β_2 in the third vortex can be described by an arbitrary small phase α

$$\beta_1 = \alpha + \frac{\pi}{3} + \pi, \tag{4.6}$$

$$\beta_2 = \alpha + \pi - \frac{\pi}{3} + \pi, \tag{4.7}$$

so, the difference of the phases between β_1 and β_2 is

$$\beta_1 - \beta_2 = -\frac{\pi}{3}, \tag{4.8}$$

where $|\beta_1 - \beta_2| = \theta = \pi/3$. $\beta_1 - \beta_2 < 0$ means the third vortex also rotates clockwise with the topological charge $M = -1$. If the second vortex has the topological charge $M = +1$, the phase difference in the third vortex $|\beta_1 - \beta_2| = \pm\pi \neq \theta$.

(ii) For the 0-state vortices, when the second vortex has the topological charge $M = -1$, the phase difference in the third vortex $|\beta_1 - \beta_2| = 2\pi/3 \neq \theta$, when the second vortex has the topological charge $M = +1$, the phase difference in the third vortex $|\beta_1 - \beta_2| = 0 \neq \theta$. It turns out that in the three phase-locked vortices, the π-state vortices always have the same topological charge [Figs. 4.10(c) and 4.10(d)]. Because of this, when a single vortex is formed [Fig. 4.10(b)] with the topological charge $M = -1$, the later simultaneously formed two vortices have the same topological charge with the first one, provided that the three vortices are structured into the equilateral triangle. In other words, the first topological charge is copied by the other two vortices, so that their phases are synchronous. For the 0-state vortices, however, the three topological charges are uncertain [Fig. 4.10(f)] from the above analytical results.

Until now, it is clear that under the influence of a predefined vortex an inversely charged vortex can be formed for both 0-state and π-state vortices. However, creating a vortex with the same charge requires an additional control vortex for the π-state vortices. Therefore, for π-state vortices one can generate any expected vortex charge. These results can be used to control the topological charges of any individual vortex in a chain. A vortex chain is shown in Fig. 4.11(a) with four memory-bits '1 1 0 0' if we define the $+1$ charged vortex as the binary number 1 and the -1 charged vortex as the binary number 0. The four memory-bits are composed of four π-state vortices with $d = 10\,\mu$m. Our target is to independently switch any memory-bit to its opposite state for information reconfiguration. Here, we introduce several typical examples for the switching.

It is shown that the first memory-bit has the same topological information, the '1' state, with the second one [Fig. 4.11(b)]. To switch the first bit to its opposite state, using the method mentioned in Fig. 4.9, one can switch off the first vortex for tens of picoseconds or a longer time until the first vortex disappears, then switch it on again. Under the influence of the second vortex, the newly created first vortex changes to the '0' state as shown in Figs. 4.11(c) and 4.11(d). If a vortex is sandwiched between two different charged vortices, for example, the third vortex in Fig. 4.11(a), it is very hard to switch it to the opposite state using the method in Fig. 4.9, because its neighbouring vortices (the second and the forth ones) have opposite topological charges. To switch it to the '1' state, that is, the same state as the second vortex, an additional vortex is necessary using the method in Figs. 4.10(c) and 4.10(d). One can first switch off the third vortex for a short time, then switch it on and, simultaneously, launch an additional ring-shaped pump at the position marked by the white

ring in Fig. 4.11(a), with $d = 10 \, \mu$m, to the second and the third vortices. When the vortices are formed and reach the steady state, the additional pump can be removed. Hence, the information of the second vortex is copied by the third vortex [Figs. 4.11(c) and 4.11(d)]. In this method, the forth vortex does not strongly influence the formation of the third vortex. In this way, the '1 1 0 0' [Figs. 4.11(a) and 4.11(b)] memory state is successfully reconfigured to the '0 1 1 0' state [Figs. 4.11(c) and 4.11(d)].
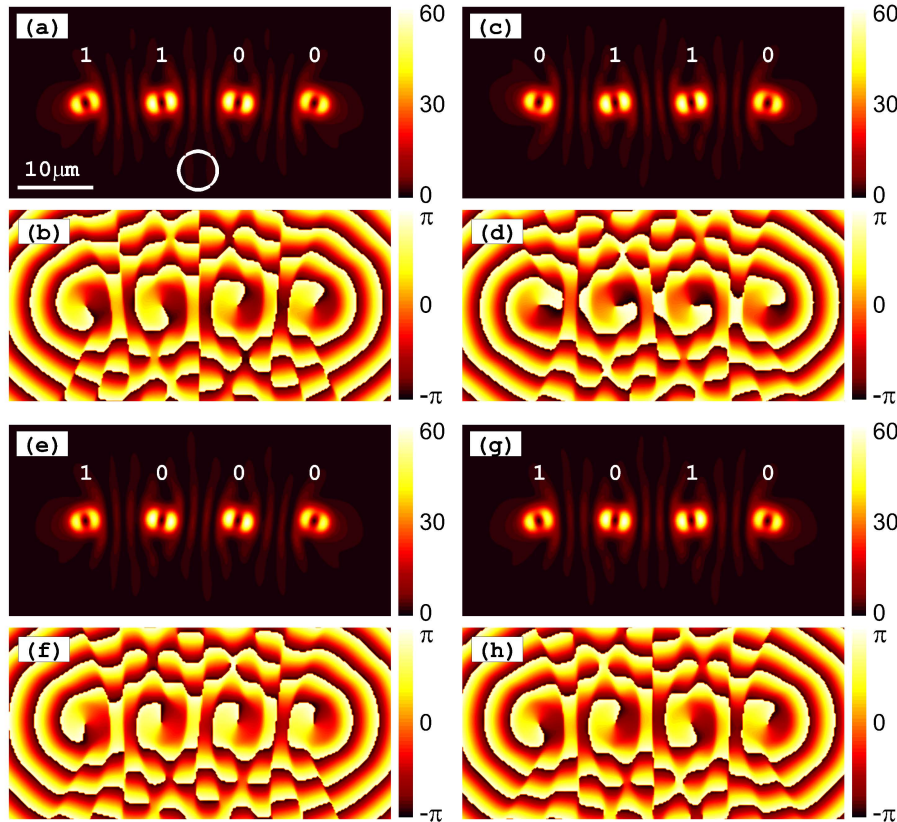

Fig. 4.11 A vortex chain containing four phase-locked π-state vortices at $d = 10 \, \mu$m. Distribution of (a,c,e,g) density and (b,d,f,h) their corresponding phase. (a,b) The '1 1 0 0' state. (c,d) The '0 1 1 0' state. (e,f) the '1 0 0 0' state. (g,h) the '1 0 1 0' state. The white circle in (a) represents the position of the additional control pump. From [191].

The second vortex in Fig. 4.11(a) is also between two vortices with opposite charges. Similarly, switching off the second vortex for a short time and then switching it on again together with the additional control pump copies the information from the third vortex, forming the '1 0 0 0' state [Figs. 4.11(e) and 4.11(f)]. For the '1 0 0 0' state, it can be seen that the third vortex is sandwiched between vortices possessing the same charge. As we introduced in Fig. 4.9, it is very easy to inverse it by switching it off and on again in a small time interval. The '1 0 1 0' state is then formed [Figs. 4.11(g) and 4.11(h)]. To switch it back

to the '1 0 0 0' state, a control pump is needed for the third vortex to print the topological charge from the second or the forth vortex.

4.4   Chapter summary and concluding remarks

In this chapter, we have demonstrated that a ring-shaped incoherent pump can support robust vortices with a integer topological charge. The vortices are more stable when they have smaller topological charges. The sign of the topological charge can be controlled by an additional nonresonant elliptical pump by launching them in different quarters divided by the elliptical solution. The sign of a predefined vortex charge can be reliably switched by means of a purely nonresonant elliptically shaped control pulse. Note that a properly tilted Gaussian beam can serve as an elliptically shaped incoherent control beam and, therefore, is well accessible for any experiment. The obtained results may serve as a step towards understanding of a long-standing challenge relating to the creation and reliable control of the coherency in dissipative systems by purely incoherent means. Besides single vortex control, we also addressed multi-vortex through vortex-vortex control. For a vortex chain including several topological charges, the topological charge of a vortex can be controlled through locked phases. A predefined vortex breaks the radial symmetry of the system because of the outgoing flow and rotation of condensates, so that a latter formed vortex always have an opposite topological charge. The three coupled π-state vortices, however, have the same topological charge if they are structured in an equilateral triangle. The control of a vortex charge can be utilized to realize an optically reprogrammable memory based on a chain of vortices.

Chapter 5

Dynamics of condensates in periodic potentials

In Chapter 3 and Chapter 4, the dynamics of polaritons in uniform semiconductor microcavities, without external potentials, were investigated. However, a localized pump was used to generate a reservoir-induced potential, also known as an optically induced potential or an internal potential depending on the profile of the excitation pump. In this chapter, we introduce a new kind of potential by fabricating the microcavity sample to modulate the cavity photon mode. The change of the cavity photon mode results in the change of the photon-exciton detuning leading to an energy shift of the lower polariton branch in the potential region. Therefore, a potential well or a potential barrier is formed to limit the flow of polaritons. This kind of potential cannot be influenced by the pump field (excitation-independent). In this chapter we investigate two kinds of external periodic potentials: one is a 1D lattice with weak contrast, the contrast of which is comparable to the kinetic energy of free polaritons, the other one is a 2D tight-trapping lattice. In the weak-contrast lattice, a simplified theoretical approach is shown to describe the oscillation dynamics of polariton condensates, which has a good agreement with the numerical results of the full GP model. In the 2D tight-binding model, a clear band structure of polariton condensates are observed. When the pump intensity is just above the condensation threshold, polaritons occupy the boundary of the first Brillouin zone (fundamental modes), then shift into the band gap region as pump intensity increases. Under a broader pump excitation, higher modes (dipoles) are excited inside each single trap. Furthermore, for stronger pump intensity, condensates can be excited in the planar region (out of the traps). Due to the limit of potential traps on the flow of condensates, a Talbot pattern (interference pattern) is observed out of the trap region. Importantly, our numerical results of the GP model match very well with the experimental results. To understand and explain more clearly the dynamics of condensates in tight-binding lattices, a discrete model

is developed which provides qualitative explanation of complex phenomena observed in recent experiments.

5.1   Dynamics of condensates in weak-contrast lattices

If considering the motion of the polaritons in the quasi one dimension, for example, confining polaritons inside a microwire by fabricating a potential in the microcavity, the system is reduced to a 1D model. The whole microcavity sample is illustrated in Fig. 5.1 (a) showing additional periodic coating on top of the sample. There are a variety of techniques were used in experiments for the fabrication of periodic potentials such as reaction ion etching [11], mirror thickness variation [132], stress application [73], metal surface deposition [133–135], surface acoustical wave modulation [136, 137], deep etching of micropillars [138], local application of crystal strain [73], deposition of semiconductor microrods on a silicon grating [139], or the microstructuring of buried mesa traps [140].
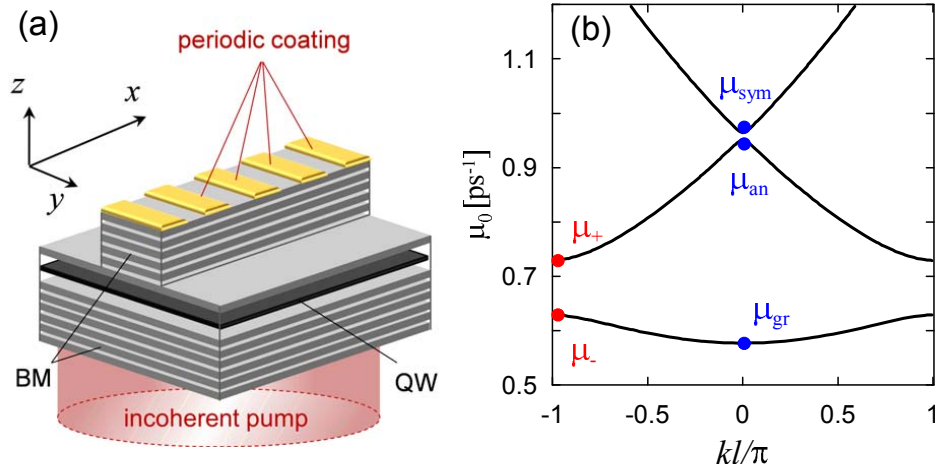

Fig. 5.1 (a) Sketch of a microcavity with a periodic coating and driven by an incoherent optical pump. A semiconductor QW is in the microcavity sandwiched between two DBRs. (b) Band structure of the polariton condensates in the vicinity of the condensation threshold $P_{th} = 16.335 \text{ ps}^{-1}\mu\text{m}^{-2}$. Eigenstates μ_{gr}, μ_{an} and μ_{sym} represent the ground, antisymmetric and symmetric states of the condensates with $k = 0$, whereas μ_{+}, μ_{-} are symmetric and antisymmetric states of the polaritons with $kl = \pi$. Other parameters are: $V_0/\hbar = 0.1 \text{ ps}^{-1}$, $l = 2\pi/\beta = 8 \mu\text{m}$. [192]

In this chapter we investigate the dynamics of condensates under incoherent excitation in the presence of external potentials with $E_c = 0$ and $V \neq 0$ in the Eqs. (2.29) and (2.30). The 1D periodic potential is written as

$$V(x) = V_0 \cos(\beta x), \tag{5.1}$$

where V_0 represents the potential depth, $\beta = 2\pi/l$ and $l = 8\ \mu$m is the period of modulation or lattice constant. The parameters in Eqs. (2.29) and (2.30) with 1D periodic potentials are $m = 10^{-4}m_e$, $\gamma_c = 0.33$ ps$^{-1}\mu$m^2, $\gamma_r = 1.5\gamma_c$, $g_c = 6 \times 10^{-3}$ meVμm^2, $g_r = 2g_c$, and $R = 0.01$ ps$^{-1}\mu$m^2.

5.1.1   The simplified approach model

Considering homogeneous excitations, a steady-state HS of the system is introduced in Chapter 3 in the limit of zero potential ($V_0 = 0$). To investigate the general dynamics of nonequilibrium polariton condensates we consider a simplified approach [131, 193, 194] taking into account only three main spatial harmonics, which is relevant to the description of the three lowest energy bands, in the weak-contrast lattice. We expand the 1D condensate wavefunction, $\Psi(x,t)$, into a set of spatial harmonics with the common transverse wavevector β and a coupling between the harmonics introduced by an index modulation term, which relieves the degeneracy at the intersections of the dispersion curves. The condensate wavefunction centered around a momentum k and reservoir density can thus be approximately expressed as

$$\Psi(x,t) \approx \left[A(t) + B(t)e^{-i\beta x} + C(t)e^{i\beta x}\right]e^{ikx}, \tag{5.2}$$

$$n(x,t) \approx n_0 + n_+ e^{i\beta x} + n_- e^{-i\beta x}, \tag{5.3}$$

where A, B, and C are condensate amplitudes of spatial harmonics. Due to the condensate-reservoir feedback during the excitation, the modulated polariton condensates evokes a spatial modulation of the reservoir described by the terms with $n_\pm$ in Eq. (5.3).

Substituting the above expansions into Eqs. (2.29) and (2.30) and collecting the terms at the same harmonics, a set of mean-field equations are obtained for each component of condensates by neglecting higher harmonic terms

$$i\hbar\frac{\partial A}{\partial t} = \left(\frac{\hbar^2 k^2}{2m} + i\Gamma_0\right)A + g_c\left(|A|^2 + 2|B|^2 + 2|C|^2\right)A + 2g_c A^* BC$$
$$+ 0.5V_0\left(B + C\right) + \Theta(n_+ B + n_- C), \tag{5.4}$$

$$i\hbar\frac{\partial B}{\partial t} = \left(\frac{\hbar^2(\beta - k)^2}{2m} + i\Gamma_0\right)B + g_c\left(|B|^2 + 2|A|^2 + 2|C|^2\right)B + g_c C^* A^2$$
$$+ 0.5V_0 A + \Theta n_- A, \tag{5.5}$$

$$i\hbar\frac{\partial C}{\partial t} = \left(\frac{\hbar^2(\beta+k)^2}{2m} + i\Gamma_0\right)C + g_c\left(|C|^2 + 2|A|^2 + 2|B|^2\right)C + g_cB^*A^2$$
$$+ 0.5V_0A + \Theta n_+A, \tag{5.6}$$

where $\Gamma_0 \equiv \frac{\hbar}{2}(Rn_0 - \gamma_c) - ig_rn_0$ characterizes gain or loss depending on the sign of its real part [Re(Γ_0)], namely, the homogeneous component of the reservoir n_0, $\Theta = \left(\frac{i\hbar}{2}R + g_r\right)$ is a complex amplitude characterizing the coupling between the reservoir and its spectral components. Similarly, a set of equations for the density of the reservoir described by sideband components $n_\pm$ is also obtained:

$$\frac{\partial n_0}{\partial t} = P_0 - \left(\gamma_r + R\left(|A|^2 + |B|^2 + |C|^2\right)\right)n_0$$
$$- R\left(A^*B + AC^*\right)n_+ - R\left(A^*C + AB^*\right)n_-, \tag{5.7}$$

$$\frac{\partial n_+}{\partial t} = - \left(\gamma_r + R\left(|A|^2 + |B|^2 + |C|^2\right)\right)n_+$$
$$- R\left(A^*C + AB^*\right)n_0 - RCB^*n_-, \tag{5.8}$$

$$\frac{\partial n_-}{\partial t} = - \left(\gamma_r + R\left(|A|^2 + |B|^2 + |C|^2\right)\right)n_-$$
$$- R\left(A^*B + AC^*\right)n_0 - RBC^*n_+. \tag{5.9}$$

So far, in weak-contrast lattices the full GP model is truncated to a simplified model, Eqs. (5.4)-(5.9), for describing the time evolution of the three spatial components of the condensates and the incoherent reservoir.

Under a homogeneous pump, the density of the reservoir is given mainly by the homogeneous oscillation component which is larger than the inhomogeneous components with $n_0 \simeq n_{r0} \gg n_+, n-$. Thus, for steady-state solutions the following conservation law is obtained

$$I_0 = |A(t)|^2 + |B(t)|^2 + |C(t)|^2 \approx \frac{P_0}{n_{r0}R} - \frac{\gamma_r}{R}, \tag{5.10}$$

where $n_{r0} = \gamma_c/R$ represents the homogeneous component of the reservoir for steady-state solutions.

Within the simplified model, when the pump intensity is just beyond the condensation threshold, the condensates begin to form. Around the threshold the band-gap structure is not modified so strongly due to the weak-contrast potentials. In addition, the influence of the nonlinearity formed by the polariton-polariton interaction can be neglected because of the weak density of condensates. In this condition, to find the stationary solutions of three

components, we assume they have the same eigenfrequency and the ansatzes have the form

$$A(t) = ae^{-i\mu(k)t}, \tag{5.11}$$

$$B(t) = be^{-i\mu(k)t}, \tag{5.12}$$

$$C(t) = ce^{-i\mu(k)t}, \tag{5.13}$$

where a, b, and c are corresponding amplitudes and $\mu(k)$ is the eigenfrequency or the chemical potential related to the momentum k. Substituting the ansatzes (5.11)-(5.13) into Eqs. (5.4)-(5.6) and considering the linear limit and neglecting the imaginary parts, one can obtain the three coupled equations of the amplitudes

$$\hbar\mu(k)a = \frac{\hbar^2 k^2}{2m}a + g_r n_0 a + \frac{V_0}{2}(b+c), \tag{5.14}$$

$$\hbar\mu(k)b = \frac{\hbar^2 k^2}{2m}b + g_r n_0 b + \frac{V_0}{2}a, \tag{5.15}$$

$$\hbar\mu(k)c = \frac{\hbar^2 k^2}{2m}c + g_r n_0 c + \frac{V_0}{2}a. \tag{5.16}$$

The above coupled eigenequations can be written in a matrix form

$$\begin{pmatrix} \frac{\hbar^2 k^2}{2m} & \frac{V_0}{2} & \frac{V_0}{2} \\ \frac{V_0}{2} & \frac{\hbar^2(k-\beta)^2}{2m} + g_r n_0 & 0 \\ \frac{V_0}{2} & 0 & \frac{\hbar^2(k+\beta)^2}{2m} + g_r n_0 \end{pmatrix} \begin{pmatrix} a \\ b \\ c \end{pmatrix} = \hbar\mu(k) \begin{pmatrix} a \\ b \\ c \end{pmatrix}. \tag{5.17}$$

By solving the above linear eigenvalue problem a dispersion relation, dependence of the condensate energy $\hbar\mu_0(k)$ on the transversal momentum k, is found. The results are presented in Fig. 5.1 (b). It is shown that in recent experiments the condensation of polaritons in periodic lattices appears around the high symmetry points such as zero momentum, $k = 0$, and the boundaries of the Brillouin zone, $k = \pm\beta/2$ [133, 136, 195]. For $k = 0$, the condensates have the same phase in potential traps, which is called in-phase or 0-state, while for $k = \pm\beta/2$, the condensates are characterized by the phase difference between two neighbouring potential minima being equal to π, which is known as the anti-phase or π-state.

In this section, we mainly investigate the condensate dynamics under the simplified model, Eqs. (5.4)-(5.9), at the symmetry points, that is the 0-state point with $k = 0$ and the π-state point with $k = \pm\beta/2$. For the 0-state with $k = 0$, the eigenvalues and eigenvectors can be obtained by solving analytically the matrix in Eq. (5.17). Three energy states, the

ground state, the antisymmetric state, and the symmetric state, can be found from the band structure in Fig. 5.1(b).

The ground eigenstate has minimal energy which is given by

$$\hbar\mu_{\text{gr}} = g_r n_{r0} + 2E_0 - \sqrt{4E_0^2 + V_0^2/2},\tag{5.18}$$

where $E_0 = \hbar^2\beta^2/8m$ is a characteristic energy representing the kinetic energy of condensate at the boundary of the Brillouin zone where $k = \beta/2$. The corresponding eigenvector is

$$\begin{pmatrix} a \\ b \\ c \end{pmatrix} = \frac{\sqrt{I_0}}{\sqrt{2G\left(G+4E_0/V_0\right)}} \begin{pmatrix} G+4E_0/V_0 \\ -1 \\ -1 \end{pmatrix},\tag{5.19}$$

where $G \equiv \sqrt{\left(4E_0/V_0\right)^2 + 2}$. The normalization of the eigenvector's length is given by Eq. (5.10). From the eigenvector, one notes that the two inhomogeneous oscillation components are symmetric with $b=c$, which means that they oscillate against each other during the time evolution. In this case, the amplitude of the homogeneous (zero-momentum) component is stronger than the others with $|a| > |b| = |c|$.

The first excited eigenstate of the condensate is antisymmetric and is given by

$$\hbar\mu_{\text{an}} = g_r n_{r0} + 4E_0,\tag{5.20}$$

with the corresponding eigenvector

$$\begin{pmatrix} a \\ b \\ c \end{pmatrix} = \sqrt{\frac{I_0}{2}} \begin{pmatrix} 0 \\ +1 \\ -1 \end{pmatrix},\tag{5.21}$$

in respect to the momentum sign inversion ($b = -c$). The zero-momentum component vanishes such that this state has a perfect sin-like shape and is spatially shifted by one quarter of a lattice period.

The second excited eigenstate also has a symmetric shape and reads

$$\hbar\mu_{\text{sym}} = g_r n_{r0} + 2E_0 + \sqrt{4E_0^2 + V_0^2/2},\tag{5.22}$$

with the corresponding eigenvector

$$
\begin{pmatrix} a \\ b \\ c \end{pmatrix} = \frac{\sqrt{I_0}}{\sqrt{2G\left(G - 4E_0/V_0\right)}} \begin{pmatrix} G - 4E_0/V_0 \\ +1 \\ +1 \end{pmatrix},
\tag{5.23}
$$

in respect to the momentum sign inversion ($b = c$). Unlike the ground-state (5.19) the central zero-momentum component of the symmetric state converges to zero ($a \to 0$) for a vanishing potential ($V_0 \to 0$).

A proper initial distribution of exciton-polaritons should be chosen to study the relaxation dynamics in weak-contrast lattice under the simplified model. An antisymmetric eigenstate as the initial condition, introduced in Eq. (5.21), is used. In experiments this can be realized by launching two coherent optical pulses with a proper phase difference and arranged in opposite directions. Considering the homogeneous excitation, the initial condition of the reservoir is taken to be spatially homogeneous with $n_0 = n_{r0}$ and $n_+ = n_- = 0$. Small-amplitude noise, which breaks the symmetry of the initial eigenstate triggering the relaxation dynamics to the more stable state, has also been added to the initial condensate profiles. Figures 5.2(a) and 5.2(b) clearly demonstrate that the initially excited state [Eq. (5.21)] relaxes to the ground states [Eq. (5.19)] after a short time. The relaxation dynamics are induced by the spatial modulation of the reservoir. Within the simplified model, the first three lowest energy states result from the uniform gain [$Re(\Gamma_0)$] due to the homogeneous excitation such that the modulation of the reservoir is negligible with $n_\pm = 0$ in the linear case. When considering the nonlinearity and the influence of the periodic potential with the pump intensity above the condensation threshold, the reservoir is modulated ($n_\pm \neq 0$) due to the non-neglectable feedback of the density of condensates. The strong feedback breaks the symmetry of the solution resulting in the transition to the more stable ground state. In the ground state coherent polaritons gather around the valleys of the periodical potential. This is the reason why the excited initial conditions eventually switch to the ground state after a hundred picoseconds oscillation.

The relaxation dynamics from the excited state to the ground state occurs only when the potential depth is weaker weaker, assuming a fixed pump intensity. For lattices with stronger potential depth, even the single ground state becomes unstable leading to complex oscillations, as illustrated in Figs. 5.2(c) and 5.2(d). These oscillations appear due to the temporal beating between the ground state and the excited symmetric state. Similar beating dynamics between two spatial modes of a weak-contrast lattice have been predicted for the optical parametric oscillator [196]. Thus the oscillation frequency ω_{zero} can be estimated as

the difference between the eigenfrequencies μ_{sym} and μ_{gr},

$$\omega_{\text{zero}} \approx \sqrt{(4E_0/\hbar)^2 + 2(V_0/\hbar)^2}. \tag{5.24}$$

Numerical simulations demonstrate that the relation of (5.24) from the simplified model predicting accurately the oscillations frequency in the vicinity of the condensation threshold ($P_0 \approx P_{\text{th}}$) [Fig. 5.2(e)], where the condensate density and the reservoir modulation are very small. For a stronger pump intensity the influence of the nonlinear effects and reservoir inhomogeneities play an important role. As a consequence, the oscillation frequency increases with the pump intensity until the critical value where the ground mode of the condensate state stabilizes again and the oscillations disappear. This threshold boundary [Fig. 5.2(f)] for the appearance of oscillations is determined by potential depth and pump intensity. For fixed pump intensity, the oscillation dynamics appears at larger potential depth because the potential can be regarded as a perturbation and the inhomogeneous reservoir is supporting oscillations. When the density of the near homogeneous reservoir is stronger, however, the formation of stable ground stated is preferred.

Considering the condensates around the boundaries of the Brillouin zone for $k = \pm\beta/2$, the analytical solutions are very cumbersome. To simplify the solutions, we consider only the first two eigenstates as shown in Fig. 5.1(b) where the third eigenstate (the C component) is far above them and can be neglected in the limit of weak-contrast lattices. Thus, the previous three coupled eigenequations (5.14) and (5.15) can be rewritten as

$$\hbar\mu(k)a = \frac{\hbar^2 k^2}{2m}a + g_r n_0 a + \frac{V_0}{2}b, \tag{5.25}$$

$$\hbar\mu(k)b = \frac{\hbar^2 k^2}{2m}b + g_r n_0 b + \frac{V_0}{2}a, \tag{5.26}$$

which provide a cubic polynomial for the eigenvalue and can be written in the matrix form

$$\begin{pmatrix} \frac{\hbar^2 k^2}{2m} & \frac{V_0}{2} \\ \frac{V_0}{2} & \frac{\hbar^2(k-\beta)^2}{2m} + g_r n_0 \end{pmatrix} \begin{pmatrix} a \\ b \end{pmatrix} = \hbar\mu(k) \begin{pmatrix} a \\ b \end{pmatrix}. \tag{5.27}$$

In this approximation, two eigenstates are found with the eigenfrequencies

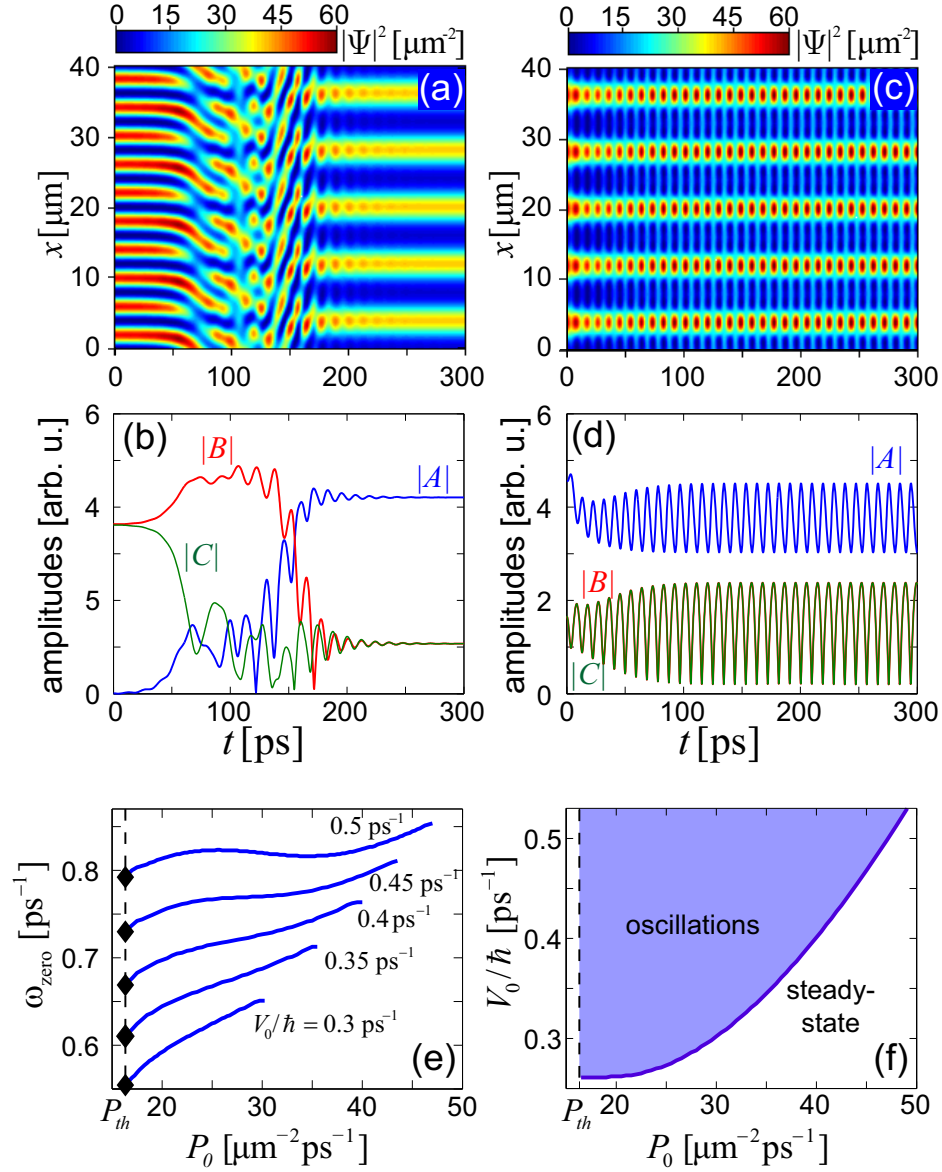$$\hbar\mu_\pm = g_r n_{r0} + E_0 \pm V_0/2\,, \tag{5.28}$$

Fig. 5.2 Time evolutions of 0-state condensates at $P_0 = 25 \text{ ps}^{-1} \mu\text{m}^{-2}$ for potential contrasts (a,b) $V_0/\hbar = 0.2 \text{ ps}^{-1}$ and (c,d) for $V_0/\hbar = 0.35 \text{ ps}^{-1}$. (a,c) Density distribution of condensates. (b,d) Amplitudes of three spatial harmonics corresponding to (a) and (c), respectively. The initial state of the condensate is taken in the form of antisymmetric state (5.21) for (a,b) and in the form of ground state (5.19) for (c,d), respectively. (e) Dependence of oscillation frequencies on the pump intensity for different potential contrasts. Dark diamonds depict the analytical results given by Eq. (5.24). (f) Phase boundary of pump intensity versus modulation depth $V_0/\hbar$, illustrating the domain of persistent oscillation existence (shaded area). The vertical dashed line shows the threshold pump intensity. From [192].

and the corresponding eigenvectors

$$\begin{pmatrix} a \\ b \\ c \end{pmatrix} \approx \sqrt{\frac{I_0}{2}} \begin{pmatrix} +1 \\ \pm 1 \\ 0 \end{pmatrix} . \tag{5.29}$$

The sign "+" ("−") in Eqs. (5.28) and (5.29) represents symmetric (antisymmetric) eigenstates relative to the central momentum $k = \beta/2$.

The numerical results [Figs. 5.3(a) and 5.3(b)] show that both symmetric (μ_+) and antisymmetric (μ_-) eigenstates undergo instability. They switch to dynamically stable persistent oscillations with maxima of the condensate density oscillating around the bottoms of the potential valleys. Similar to the oscillation dynamics in Fig. 5.2 the oscillations between two π-states also exist even in the vicinity of the condensation threshold. In other words, coherent polaritons periodically change their collective momenta between two values $k = +\beta/2$ and $k = -\beta/2$ which are represented in the simplified model by the spatial harmonics A and B, respectively [Fig. 5.3(b)]. This is similar to Josephson oscillations of the polaritons in the double well potential well [197]. However, unlike conventional Josephson dynamics, the oscillations considered here happen in the momentum space between two components with different momenta and, therefore, can be observed in the far-field measurements. The oscillation frequency can be approximated by a simple expression

$$\omega_\pi \approx \mu_+ - \mu_- = V_0/\hbar . \tag{5.30}$$

The frequency of oscillations ω_π can also be found analytically in the limit of a very weak lattice contrast ($V_0 \to 0$) where the spatial modulation of the reservoir can be neglected ($n_\pm = 0$). Assuming $C = 0$ and $n_\pm = 0$ in the simplified model, the problem can be reduced to two coupled nonlinear equations in the standard system [198]. In this case, if the two components A and B completely exchange their populations during oscillation, one can obtain

$$\omega_\pi = \frac{\pi V_0}{2\hbar F\left(\frac{\pi}{2} \,|m'\right)} , \tag{5.31}$$

where $F(x|m')$ is a first order elliptic integral with $m' = \frac{I_0^2 g_c^2}{4V_0^2}$, and the total density of the condensate $I_0 = |A|^2 + |B|^2$ can be approximated by Eq. (5.10). When the pump is slightly
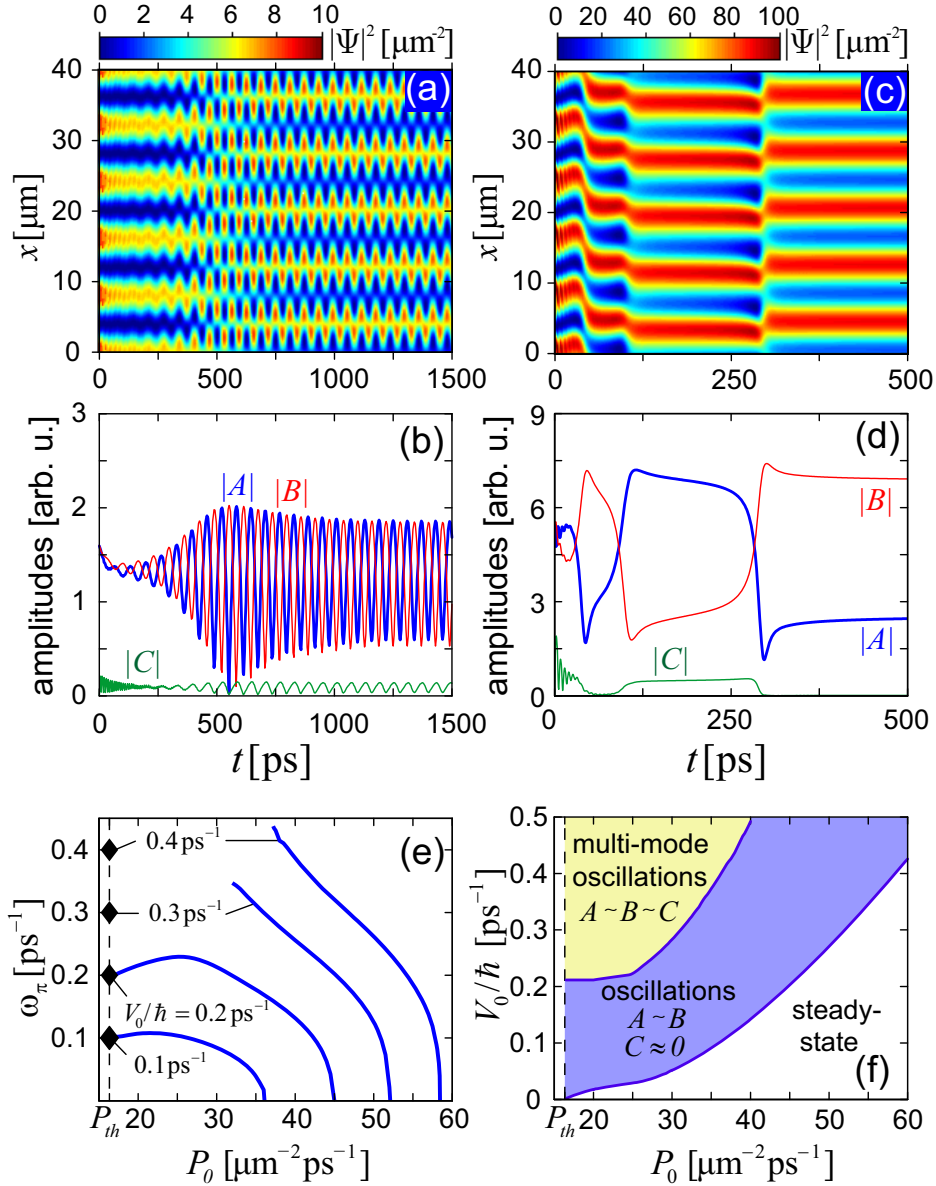
Fig. 5.3 Time evolutions of π-state condensates for the potential contrasts $V_0/\hbar = 0.1$ ps^{-1} at pump intensity (a,b) $P_0 = 18$ ps$^{-1}\mu$m^{-2} and (c,d) $P_0 = 36$ ps$^{-1}\mu$m^{-2}. (a,c) Density distribution of condensates. (b,d) Amplitudes of the spatial harmonics. (e) Dependence of oscillation frequencies on the pump intensity for different values of the modulation depths. Dark diamonds depict the analytical results given by Eq. (5.30). (f) Phase boundary of the pump intensity versus modulation depth. From [192].

above the threshold where $m' \ll 1$. The frequency of oscillations approaches

$$\omega_\pi \simeq \frac{V_0}{\hbar} \left(1 + \frac{1}{16} \frac{I_0^2 g_c^2}{V_0^2}\right)^{-1}. \tag{5.32}$$

It is worth noting that for $P_0 \simeq P_{\text{th}}$ the oscillations become linear because $I_0 \simeq 0$ so that the oscillation frequency of Eq. (5.32) has the same form as that seen in Eq. (5.30). The approach given by Eqs. (5.31) and (5.32) is valid in the vicinity of condensation threshold, since, unlike the conventional Josephson oscillations, the system is governed by the saturation dynamics of the reservoir rather than by the Kerr-like nonlinearity. For a stronger pump intensity the nonlinear effect changes the character and the periods of oscillations drastically. The oscillation frequency decreases along with the increase of pump P. For even stronger pump intensity ($P_0 > 36$ ps$^{-1}\mu$m^{-2} for $V_0/\hbar = 0.1$ ps^{-1} for instance) the solution becomes steady-state with the energy residing in the potential peaks [Fig. 5.3(c),(d)]. It is shown in Figs. 5.3(b) and 5.3(b) that the density in the third energy state (the C component) is very small as introduced in Eq. (5.29).

The π-state oscillations and their frequencies are sensitive to the pump intensity and potential depth as summarized in Fig. 5.3(e). For a lattice with very weak modulation contrasts ($V_0/\hbar < 0.21$ ps^{-1}) persistent oscillations exist in a pump interval from the condensation threshold to the critical value where the oscillation frequency approaches zero, that is, steady-states. The whole solutions for different pump intensity and potential depthes are presented in Fig. 5.3(f). For stronger potential depths ($V_0/\hbar > 0.21$ ps^{-1}), the threshold of π-oscillations shifts to the larger values of the pump intensity where the periodic energy exchange between $k = +\beta/2$ and $k = -\beta/2$ components in nonlinear case. For much stronger potential depth, the oscillation becomes less regular, transforming to a quasi-periodic regime as shown in the upper "multi-mode oscillations" region in Fig. 5.3(f). In this regime the condensates exhibits oscillatory behavior for which the population of higher mode $|C|$ becomes comparable with the lower modes $|A|$ and $|B|$.

5.1.2   Dynamics of condensates within the full GP model

In the previous section we discussed the steady-state and oscillation dynamics of condensates in the frame of a simplified model, Eqs. (5.4)-(5.9). To prove the validity of the simplified model, the original model, Eqs. (2.29) and (2.30), should be used. In this section we study the existence and stability of both 0-state and π-state oscillatory solutions obtained in the frame of the full GP model with the periodic potentials.

As introduced in the above section, to obtain the steady-state or oscillatory solutions a crucial initial condition is necessary. In the full GP model, the initial conditions also significantly influence the relaxation dynamics of condensates. It is shown that in Fig. 5.3(e) when the potential depth is smaller, condensates are easily pumped to the π-state oscillation. We use $k = \beta/2$ or $k = -\beta/2$ for the initial conditions in the GP model. These momenta can be excited in experiments by angling an optical beam. When the pump intensity is just above the condensation threshold, persistent oscillation emerges [Fig. 5.4(a)] after a few nanoseconds. The time evolution of its phase [Fig. 5.4(b)] shows that this oscillatory behavior is really due to the collective momenta oscillating between $k = \beta/2$ and $k = -\beta/2$. This is in perfect agreement with previous analytical predictions in Eq. (5.32) and 5.3(b). The comparison for different pump powers is shown in Fig. 5.4(c), which shows that they agree very well for smaller pump intensity even for larger potential depth. For larger pump intensity, however, the oscillation dynamics becomes unstable after some time (several hundreds picoseconds) and jump spontaneously to the ground state, as shown in Fig. 5.4(e), which is a metastable state. To demonstrate the stability of oscillations, we add white noise to the initial conditions. Figure 5.4(d) shows the existence regions of the steady-state solutions, the stable oscillations, and the metastable states. The stable π-state oscillations appear when the potential contrast is weak and the pump intensity is close to the condensation threshold. When the pump intensity is larger and the potential depth is stronger, oscillations disappear and steady-state solutions are seen, these are the metastable states. For much stronger potential depth or pump intensity, only steady-state solutions exist as shown in the white region in Fig. 5.4(d).

As studied in Fig. 5.2(f) in the simplified model, the oscillation dynamics in 0-state always appears at larger potential depth. In the full GP mode, as shown in Figs. 5.5(c) and 5.5(d), the temporal beating of the ground state and the excited state for a stronger potential depth is obtained. In this condition the oscillation dynamics are in a full agreement with those found in the simplified model, as shown in Figs. 5.2(c) and 5.2(e). However, these oscillation dynamics in the full model are in a metastable region which exist for only tens of nanoseconds before spontaneously transferring to another oscillation state [Figs. 5.5(c) and 5.5(d)]. The density of the two oscillations in Figs. 5.5(a) and 5.5(c) are very similar, but their phases are different. The phase profile shown in Fig. 5.5(d) is the combined oscillations of 0-state and π-state. Apparently, the selective gain saturation associated with the reservoir dynamics is responsible for this particular choice of the condensate eigenstates involved into the oscillations. Note that this type of oscillation is very robust and can be formed even from noise initial conditions. The comparison of the oscillation frequencies between the GP model and the simplified model is shown in Fig. 5.5(e). One can see that the results
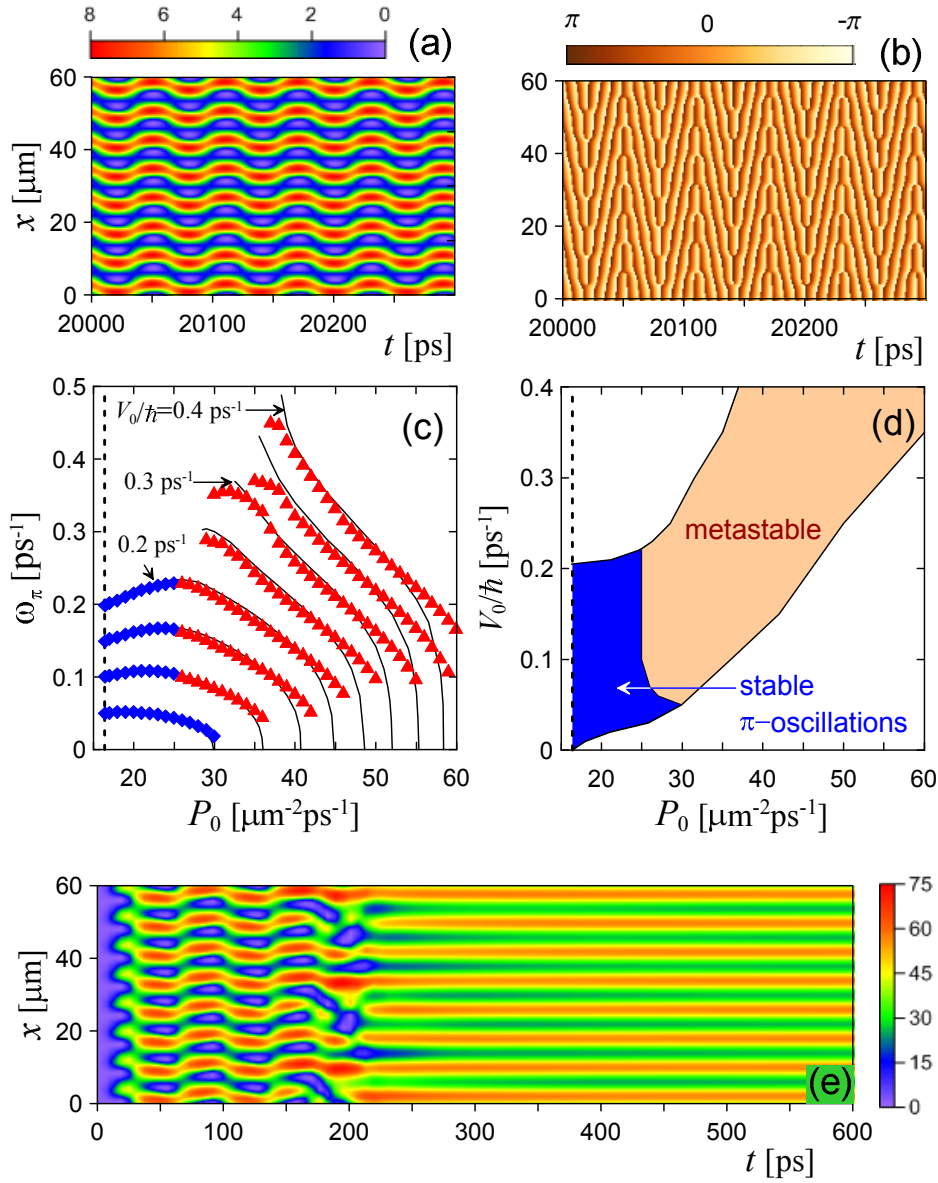
Fig. 5.4 Profiles of (a) condensate density and (b) phase of oscillating π-states for the potential contrasts $V_0/\hbar = 0.1$ ps^{-1} and $P_0 = 18$ ps$^{-1}\mu$m^{-2}. (c) Dependence of oscillation frequencies on the pump intensity for the following values of the modulation depths (from the left bottom to the right top): $V_0/\hbar = 0.05, 0.1, 0.15, 0.2, 0.25, 0.3, 0.35,$ and 0.4 ps^{-1}. Blue diamonds depict dynamically stable oscillations with oscillation time is longer than 1 ns. Red triangles show the metastable oscillations with oscillation time is between 100 ps and 1 ns. Thin solid lines depict the results of the simplified model (5.4)-(5.9). (d) Existence domain of stable and metastable π oscillations. (e) Density profile of the metastable oscillations for $P_0 = 30$ ps$^{-1}\mu$m^{-2} and $V_0/\hbar = 0.1$ ps^{-1}. From [192].

of the simplified model agree qualitatively with the results of the GP model especially for smaller pump intensity and potential depth. The agreement of the two results becomes worse
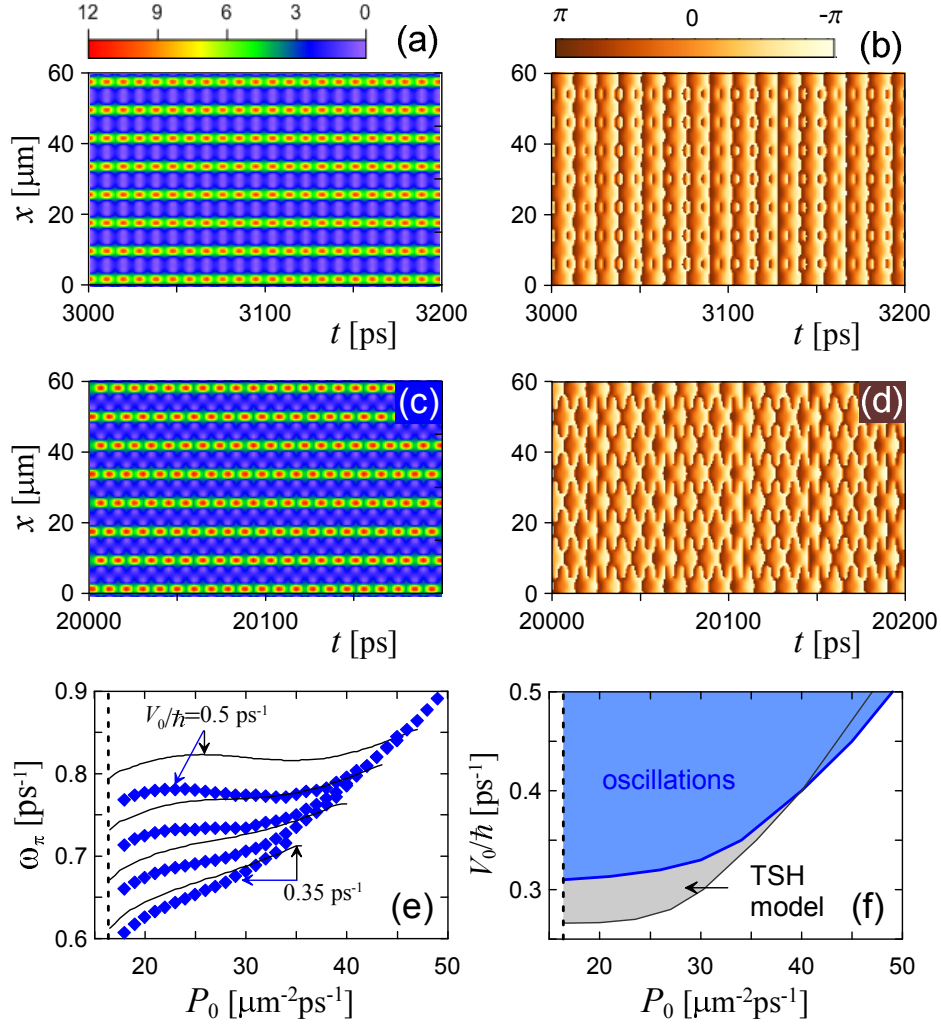

Fig. 5.5 Profiles of (a) the condensate density and (b) phase of the meta-stable oscillation for the potential contrasts $V_0/\hbar = 0.4$ ps^{-1}. (c) and (d) the same as in (a) and (b), respectively, after a long time ($t > 10000$ ps). (e) Dependence of oscillation frequencies on the pump intensity of the potential depths (from the bottom to the top): $V_0/\hbar = 0.35, 0.4, 0.45,$ and 0.5 ps^{-1}. Blue diamonds represent the results of the GP model (2.29) and (2.30), whereas thin solid lines depict the results of the simplified model (5.4)-(5.9). (f) Existence domain of 0-state oscillations obtained both in the GP model (blue shaded area) and in the simplified model. From [192].

when the pump intensity is larger of the potential contrast is stronger. The existence domain for both oscillation solutions can be seen in Fig. 5.5(f). It is shown from their existence domain that the dismatch of the two oscillations becomes worse for smaller pump intensity. As discussed previously, the approach of the simplified model should be more accurate for

smaller pump intensity in the linear limit. However, the neglected higher energy states in the simplified model play a significant role in the full GP model in the linear limit such that the oscillations are easily perturbed to the steady-state for weaker potential depth and pump intensity in the full model as shown in Fig. 5.5(f).

5.2 Dynamics of condensates in tight-trapping lattices

In this section we consider the case when the potential depth is much larger than the kinetic energy of free polaritons. This means that the majority of polaritons will be found in potential traps. In the tight-binding model, the dynamics of polariton condensates around the bottom of the LPB can also be described by the Eq. (2.29). However, in order to more accurately compare to real experiments, additional white quantum noise should be added into the GPE because there is always loss due to the finite lifetime of polaritons and gain from the continuous pumping during the condensation in the nonequilibrium system. Therefore, if considering only incoherent excitation with $E_c = 0$, Eq. (2.29) can be rewritten as

$$i\hbar\frac{\partial\Psi(\mathbf{r},t)}{\partial t} = \left[-\frac{\hbar^2}{2m}\nabla_\perp^2 - i\hbar\frac{\gamma_c}{2} + g_c|\Psi(\mathbf{r},t)|^2 + \left(g_r + i\hbar\frac{R}{2}\right)n(\mathbf{r},t) + V(\mathbf{r})\right]\Psi(\mathbf{r},t)$$
$$+ i\hbar\frac{d\Psi_{\mathrm{st}}(\mathbf{r},t)}{dt},$$
(5.33)

where the dynamics of the incoherent reservoir $n(\mathbf{r},t)$ still obey Eq. (2.30). The white noise is described by the last term of the right side of Eq. (5.33). It is known that nonequilibrium polaritons condensate and disappear very fast, which is the major contribution to this noise source. Thus, the noise satisfies the correlation

$$d\Psi_{\mathrm{st}}(\mathbf{r}_i,t) = \sqrt{\frac{\gamma_c + Rn(\mathbf{r}_i,t)}{4\Delta x\Delta y}}dW_i,$$
(5.34)

where dW_i is a Gaussian random variable satisfying the correlation functions $\langle dW_i dW_j\rangle = 0$ and $\langle dW_i^* dW_j\rangle = 2\delta_{ij}$, i and j are indices counting discrete mesh points $\mathbf{r}_i$ with the discretizations in the x and the y directions, respectively. Without the noise term in Eq. (5.33), one can see that Eq. (5.33) is applicable only when the pump intensity is above the condensation threshold for polaritons, that is, the gain is larger than the loss. When the pump intensity is below the threshold, the only solution for the wavefunction of the polaritons is the trivial one. In the presence of the white noise, nontrivial noise leads to the observation of dispersion spectra numerically even though the pump intensity is blow the threshold, which can be used to explain the photoluminescence spectra from experiments [171]. However,

when the pump intensity is just above the condensation threshold, the white noise can be regarded as a perturbation, are expected to slightly affect the dynamics of the condensates. When the pump intensity is much larger, the white noise is negligible in comparison to the density of condensates.

We create a periodic potential for polaritons in a 1D array within a 2D sample, as illustrated in Fig. 5.6 (a). The 1D array potential traps have the same diameter and energy depth as for the 2D case. They are distributed in a line and separated by the same interval. The lattice can be described by

$$V = \sum_{j=-Nl} V_0 \exp\left[-\left(\frac{(x+j)^2+y^2}{d'}\right)^{10}\right], \quad N = 0, \pm 1, \pm 2, \cdots, \tag{5.35}$$

where V_0 is the potential depth, l represents the lattice constant, d' is the diameter of the potential trap, and the integer number N indicates the number of traps. The parameters in the model (5.33) and (2.30) are $m = 10^{-4} m_e$, $\gamma_c = 0.33$ ps$^{-1}\mu$m^2, $\gamma_r = 0.005$ ps$^{-1}\mu$m^2, $g_c = 10^{-3}$ meVμm^2, $g_r = 2g_c$, and $R = 0.001$ ps$^{-1}\mu$m^2, which are quite different from the previous ones because they have been chosen to coincide with the parameters used in experiments from a collaboration with our group [171].

5.2.1   State transitions of condensates in 1D arrays

We consider a 1D chain array with lattice constant $l = 3$ μm, trap diameter $d' = 2$ μm, and potential depth $V_0 = 5$ meV as presented in Figs. 5.6(a) and 5.6(b). First, a narrow incoherent Gaussian pump with pump diameter $w_p = 5$ μm is used for excitation. It is clear that this narrow pump covers only one main trap as shown in Fig. 5.6(a). It is known that when the pump intensity is very small, far below the condensation threshold, the band-gap structure cannot be experimentally observed in weak periodic potentials [133] because the kinetic energy of free polaritons, as noise, at the boundaries of Brillouin zones is larger than the potential depth. However, in tight-trapping periodic potentials the band-gap structure can be clearly seen [Fig. 5.6] in the energy-momentum space after taking the Fourier transform. The band structure can also be derived analytically from the single particle state

$$\Psi(\mathbf{r}) = u_k(\mathbf{r}) \exp(i\mathbf{k}\mathbf{r}), \tag{5.36}$$

where $u_k(\mathbf{r}) = u_k(\mathbf{r}+a)$ is the Bloch function, $\mathbf{k} = (k_x, k_y)$ is limited in the first Brillouin zone. Substituting the above single particle state into Eq. (5.33) and considering only the

dispersion and potential terms, the time-independent eigenfunction can be obtained as

$$\left[\frac{\hbar^2}{2m}(-i\nabla + k)^2 + V(\mathbf{r})\right] u_{n,k}(\mathbf{r}) = E_n(\mathbf{k})u_{n,k}(\mathbf{r}),\tag{5.37}$$

where n represents the band index. The linear band structure solved from (5.37) is shown in Figs. 5.7(e)-5.7(g), which fits very well with the numerical results.
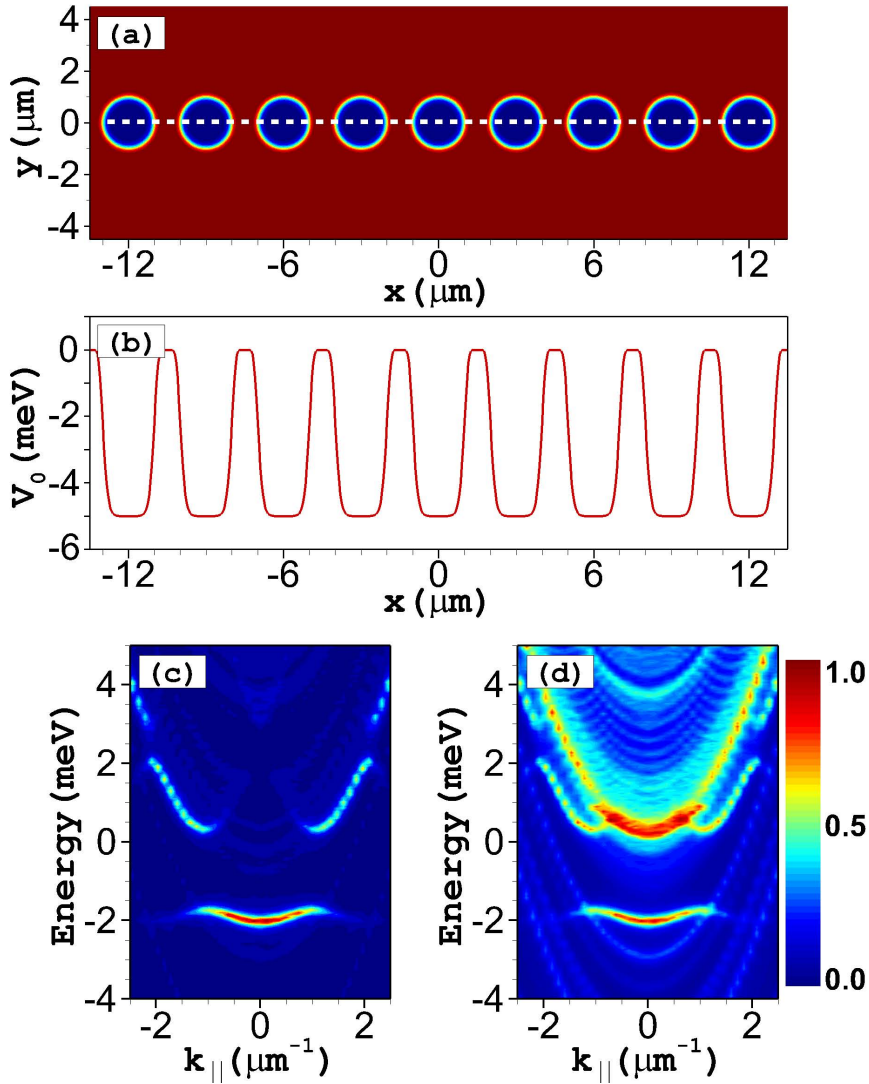

Fig. 5.6 (a) Distribution of a 1D chain lattice with the lattice constant $l = 3$. (b) Distribution of the potential depth along $y = 0$ line in (a). Spectra of polaritons at $P \ll P_{th}$ (c) along $y = 0$ line and (d) in the whole excitation region.

In addition to the first three energy bands, there is a dispersion parabola as shown in Fig. 5.6(d), which is measured in the whole excitation region. However, if one measures the band

structure just along the symmetric line ($y = 0$), one can clearly obtain the first three bands without the additional parabola as shown in Fig. 5.6(c). The reason is that the additional parabola comes from the asymmetric background planar region (outside the potential traps) along the y axis. When measuring the far field density of condensates just along y direction at $x = 0$, only the parabola dispersion, without the band structure, is observed. Note also that, in the tight-trapping potentials, the first two bands are separated by a broad gap [Fig. 5.6(c)].
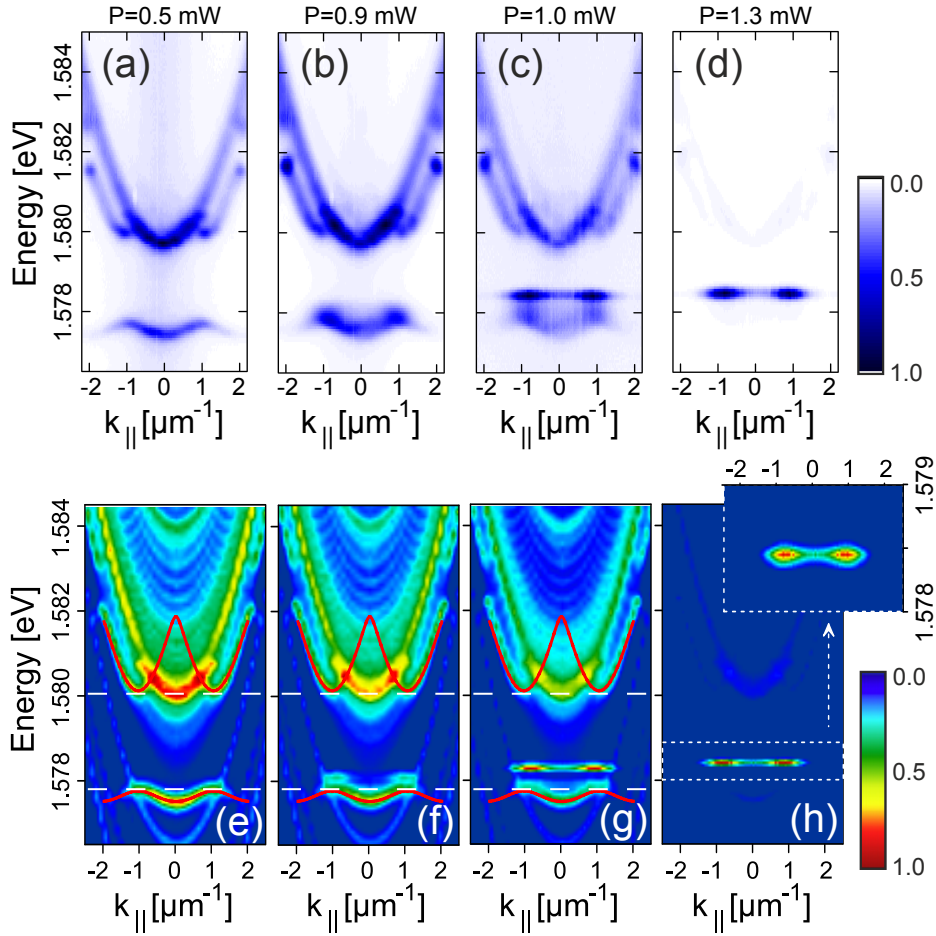

Fig. 5.7 (a)-(d) Experimental far-field photoluminescence spectra recorded at different pump powers. (e)-(h) The dependence of polariton occupation at different energy states as a function of inplane momenta, $k_\parallel$, calculated using (5.33) and (2.30) for pump intensity (e) $P_0 = 1$ ps$^{-1}\mu$m^{-2}, (f) $P_0 = 10$ ps$^{-1}\mu$m^{-2}, (g) $P_0 = 16$ ps$^{-1}\mu$m^{-2}, and (h) $P_0 = 20$ ps$^{-1}\mu$m^{-2}. The pump has a Gaussian profile with a FWHM of (a)-(d) 3.8 μm and (e)-(h) 5 μm. From [171].

In experiments [171] the band-gap structure and an additional parabola are observed when the pump intensity is smaller than the condensation threshold [Fig. 5.7(a)]. In this case, the parabola dispersion branch is mainly occupied by incoherent polaritons. Increasing the pump intensity, polaritons begin to build up at the boundaries (π-state) of the first energy

band. Simultaneously, the first band becomes broader and shifts slightly to the higher energy state [Fig. 5.7(b)]. As the pump intensity increases, close to the condensation threshold, most of polaritons that resident in the π-state of the first band move into the first finite gap due to the nonlinear effect [Fig. 5.7(c)]. When the pump intensity is larger than the threshold, almost all polaritons become coherent, occupying the π-state of the first band with a narrow line width [Fig. 5.7(d)]. The condensation dynamics of polaritons loaded into the tight-binding 1D chain lattices was first observed experimentally [Figs. 5.7(a)-5.7(d)] by our colleagues (Christian Schneider's group). They fabricated the microcavity sample using the method introduced in Ref. [171]. Upon investigation, it is found that our theoretical results [Figs. 5.7(e)-5.7(h)] agree perfectly with the experimental results.
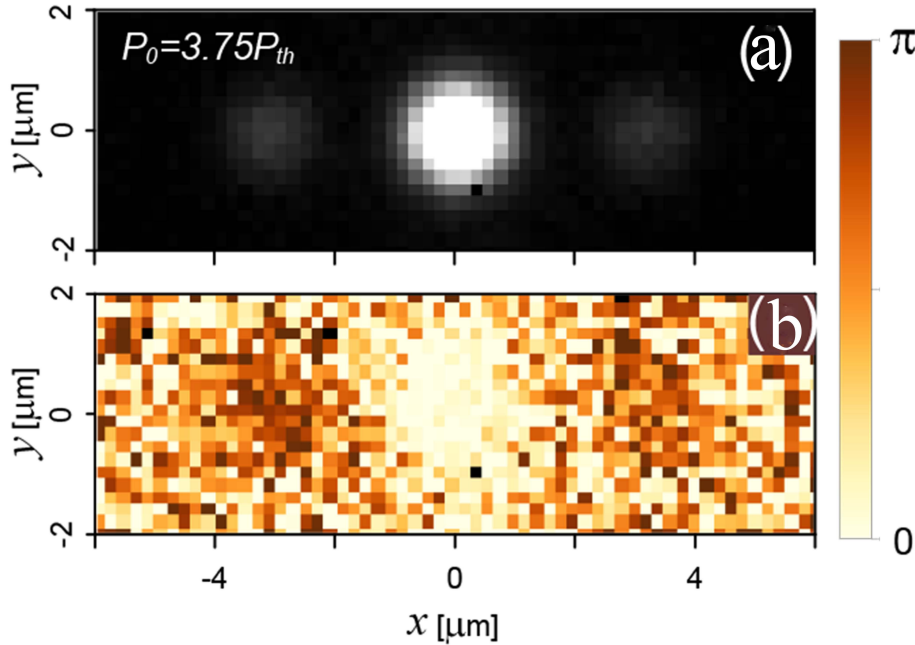

Fig. 5.8 Distributions of (a) density and (b) phase of condensates in the real space at $P_0 = 60$ ps$^{-1}\mu$m^{-2} from numerical simulations. From [171].

In experiments, when the pump intensity is much larger than the threshold, condensates in the π-state of the first band begin to occupy the lower energy state as shown in Ref. [171]. When the pump intensity is too large, most of the condensates occupy the lowest energy state, forming an "M" shape band. Importantly, one can see clearly the red shift of the first band as the pump intensity increases. This means that under much stronger excitation, the heating mechanism plays an important role, which leads to the coupling between excitons and cavity photons becomes weaker. In our simulation, we can observe the evolution of condensates to the lowest energy state. However, only blue shift of energy bands are observed instead of red shift due to the consistent defocusing nonlinearity. This is evidence that when the pump

intensity is too large the GP model is invalid for describing the polariton condensates. In this case, the acoustic phonon-mediated relaxation should be accounted for [171].

In both theoretical and experimental results, polaritons condensate initially to the π-state of the first band when the pump intensity is just above the threshold. The reason for this is that the narrow excitation pump excites only one main trap and two neighbouring traps with very small density [Fig. 5.8(a)], and the density of condensates in the planar region (the region between traps) is almost zero. It is known that two neighbouring traps can support both the symmetric modes (the ground state) and the antisymmetric modes (π-state or the excited state) [133]. Due to the zero density of condensates between neighbouring traps, the system permits only the antisymmetric modes which exhibits π phase difference between neighbouring traps [Fig. 5.8(b)]. For very strong pump intensity, a fraction of the polaritons condensate outside the traps resulting in the nonzero density distribution of condensates between neighbouring traps. Therefore, the ground state, symmetric modes, are formed. In this condition, the condensates are coherent, having the same phase distribution in each trap.
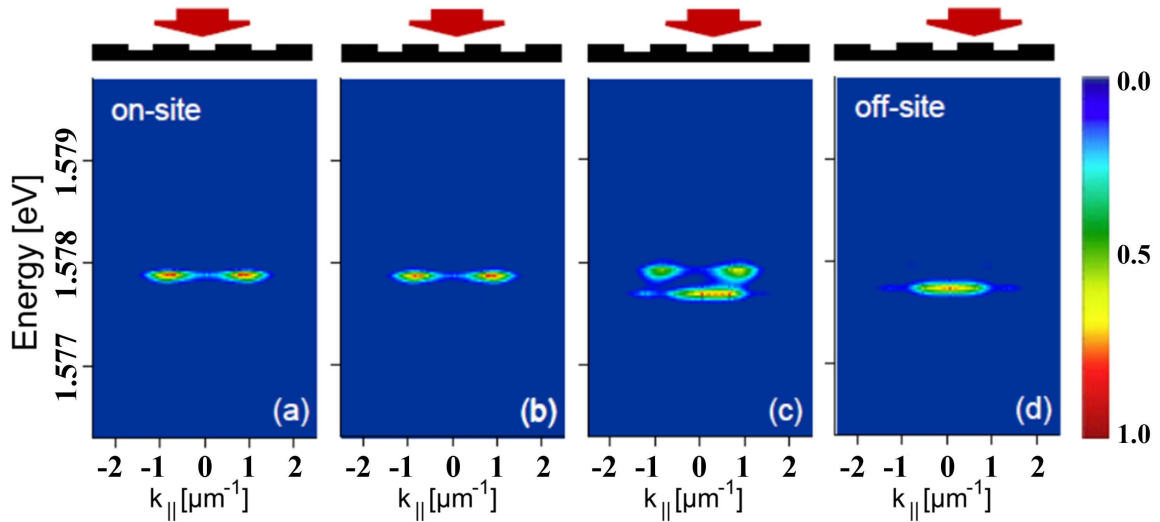

Fig. 5.9 Emission spectra at different positions of the pump. (a) The case of "on-site" excitation with the pump beam focused on the center of the trap. (b) The pump spot is shifted from the trap center at $\Delta x = 0.5 \ \mu$m. (c) The pump spot is on the edge of the trap, $\Delta x = 1.0$ μm. (d) The case of "off-site" excitation, where the pump beam is focused between two traps corresponding to a potential maximum barrier, $\Delta x = 1.5 \ \mu$m. The pump intensity is above condensation threshold with $P_0 = 40 \ \text{ps}^{-1} \mu\text{m}^{-2}$. From [171].

We previously investigated the condensation dynamics of polaritons by focusing the pump intensity around the middle of a potential trap, that is, on-site excitation, as illustrated in Figs. 5.9(a) and 5.9(b). If the excitation pump with fixed intensity is moved to the edge of a trap, major condensates transform to the lower energy state with some of them left in the

π-state [Figs. 5.9(c)]. When the pump intensity is focused around the center of a barrier (the region between two traps), that is, off-site excitation, most of the condensates occupy the ground state [Figs. 5.9(d)]. This demonstrates that the condensates raised into the excited π-state under on-site excitation are more stable. These numerical results can explain very well the experimental observation in [171].
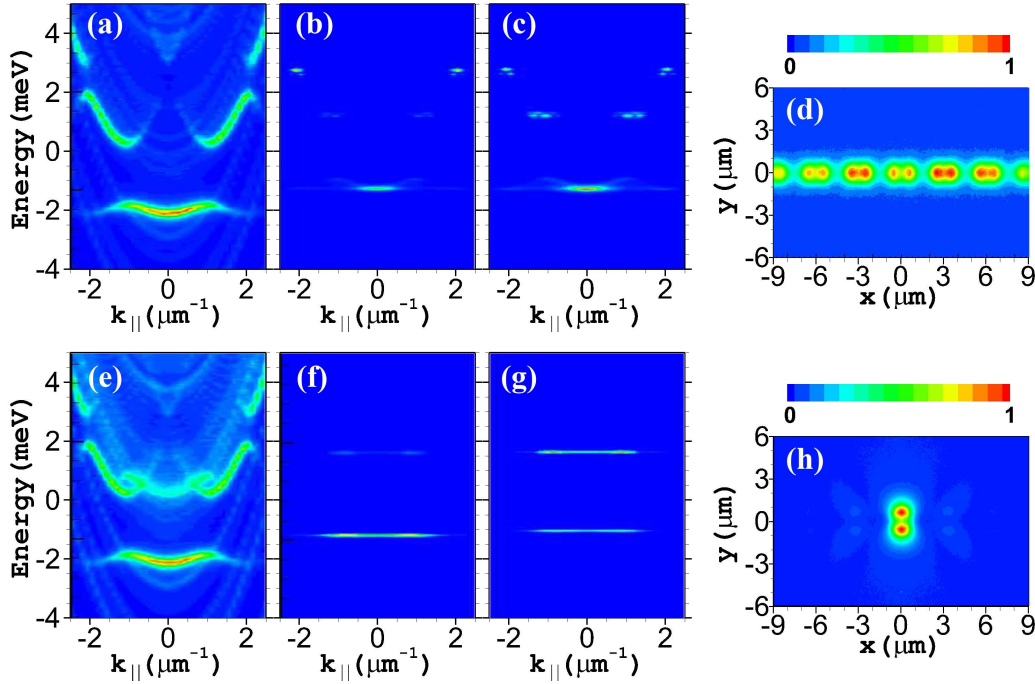

Fig. 5.10 Emission spectra under a horizontally elliptical pump measured along $y = 0$ as shown in Fig. 5.6(a) at (a) $P_0 = 1$ ps$^{-1}\mu$m^{-2}, (b) $P_0 = 40$ ps$^{-1}\mu$m^{-2}, and (c) $P_0 = 80$ ps$^{-1}\mu$m^{-2}. (d) Density distribution of condensates in real space of (b). Emission spectra under a vertically elliptical pump measured along $y = 0$ as shown in Fig. 5.6(a) at (e) $P_0 = 1$ ps$^{-1}\mu$m^{-2}, (f) $P_0 = 55$ ps$^{-1}\mu$m^{-2}, and (g) $P_0 = 80$ ps$^{-1}\mu$m^{-2}. (h) Density distribution of condensates in real space of (g).

It is found that from the previous discussion a narrow pump, which is comparable with the size of a trap, always excited the condensates to the fundamental modes (the symmetric or antisymmetric modes in the first band). An important question arises: Can the condensates be excited to the second or higher energy bands? To investigate this, we use an elliptically optical beam focused on several traps in the chain. In comparison to the previous narrow Gaussian pump, the horizontally elliptical pump has the same width along the y direction with $w_y = 5$ μm, which covers the trap region. However, the pump distribution along the x direction is much broader with $w_x = 20$ μm, which covers pairs of traps. The photoluminescence spectrum [Fig. 5.10(a)], which is only dependent upon the distribution of the periodic

potential, is the same with that introduced in Fig. 5.6(c). When the pump intensity is above the threshold, condensates build up at the boundaries (the π-state) of the second band instead of the first band presented in Fig. 5.10(b). The reason is that the broader pump along the x direction gives condensates an opportunity to flow along the chain leading to the generation of transverse dipole modes in each trap [Fig. 5.10(d)]. The boundary of the second band means the dipole modes in neighbouring traps have π phase difference, that is, antisymmetric dipoles. For the larger pump intensity, condensates begin to occupy the lower symmetric state (the 0-state) of the second band [Fig. 5.10(c)], which is similar to the transition dynamics of condensates under narrow pumps in Fig. 5.7.

If rotate the horizontally elliptical pump by $\pi/2$ to the position perpendicular with the lattice array for excitation. This elliptical pump covers only one main trap along the x direction, but covers a larger planar region out of the trap along the y direction. The clear band-gap structure can be seen in Fig. 5.10(e) as the pump intensity is far below the condensation threshold. Increasing the pump intensity just above the threshold, one can see a similar spectrum as that introduced in Fig. 5.7(d) in which condensates reside primarily in the π-state of the first band [Fig. 5.10(f)]. The difference is that a small density of polaritons, as shown in Fig. 5.10(f), condensates to the state in the additional parabola in the second band region, which can clearly be seen in Fig. 5.10(g) at larger pump intensity. As we indicated above, the additional parabola is related to the dynamics of condensates along the y direction. Moreover, it overlaps with the second band so that the condensation spectrum in the additional parabola [the higher energy state in Fig. 5.10(g)] represents the fact that a dipole mode along the y direction is formed as shown in Fig. 5.10(h). The π-state of the first band means the dipole mode is antisymmetric with its neighbours although their densities are very small [Fig. 5.10(h)]. The strong energy flow along y direction also given an opportunity for the observation of the additional parabola dispersion measured along only the $y = 0$ line when the pump intensity is below the threshold.

5.2.2 Talbot effect

The Talbot effect is a manifestation of the near-field diffraction of a coherent plane wave incident on a periodic grating, resulting in a 2D pattern of fringes. It is interpreted as the interference of coherent spherical waves originating from the apertures of the grating. As studied in Fig. 5.8, the condensates are loaded mostly into the potential traps, so that there is no clear density distribution out of the chain region. However, the density of condensates between the traps (in the barrier region) is still weak even if the pump intensity is strong because the barrier region between the traps is very narrow and the excitation pump only covers one trap. When pumping with a broader optical spot covering several traps, polaritons

begin to condensate in the planar region when the pump intensity is above the condensation threshold as shown in Fig. 5.10.
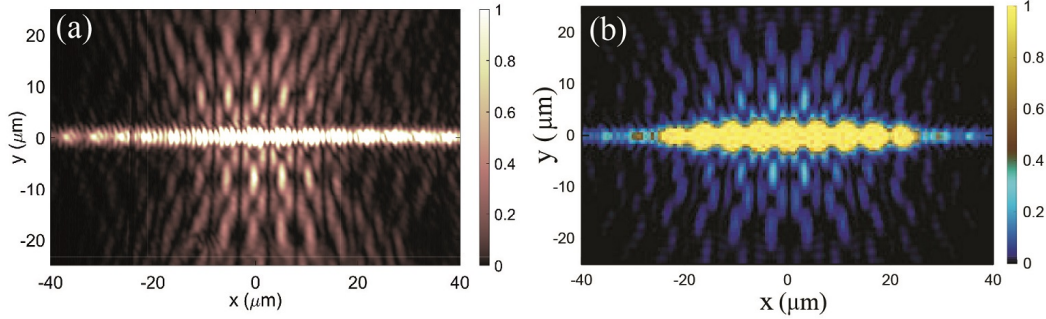

Fig. 5.11 (a) Experimental spatial distribution of the Talbot pattern of condensates. (b) Talbot pattern of condensate density calculated numerically using the GP model. From [199].

To observe clearly the polaritons condensed in the planar region, the sizes of barriers and traps are increased with the parameters are $l = 3.5$ μm and $d' = 5.5$ μm. In this case, with the pump intensity above the condensation threshold some of the condensates are forced to stay in the barriers. They then propagate perpendicularly with the potential array due to the confinement of the stronger density of condensates in the chain traps as shown in Fig. 5.11(b). The free propagation of condensates in the planar region forms a Talbot pattern because of the coherent interference. The distribution of the interference pattern out of the chain traps is shown in Fig. 5.11 where the density is much smaller than that in the traps. This Talbot effect was first observed experimentally by Elena Ostrovskaya's group as shown in Fig. 5.11(a) [199], and our numerical results in qualitative agree with them. It also shows that the stronger the pump intensity, the more visible the Talbot pattern. By comparing with the experiments, we can further verify that the GP model can accurately describe the dynamics of polariton condensates loaded into periodic potentials.

5.3   Dynamics of polaritons in discrete lattices

In the previous section, we studied the nonlinear dynamics of condensates in tight-binding periodic potentials where the condensates weakly interact with others localized in the neighbouring traps due to the evanescent tails. To get a simpler understanding of the influence of condensates from neighbouring potential wells in the tight-binding approximation, the continuous periodic problem can be reduced to a discrete model if we consider only the fundamental mode in each trap. To avoid the higher-order modes in a trap as we analyzed above, several narrow pumps can be used to individually excite each trap.

5.3.1 Discrete model and uniform solutions

Under the above assumption the order parameter can be characterized by its complex amplitude ψ_m at each site, where m is the number of the site. The density of incoherent polaritons can be characterized by the amplitude n_m at each site. The standard full GP model (2.29) and (2.30) for describing the dynamics of polariton condensates under a relevant normalization, $\psi_m = \sqrt{\frac{g_c}{\hbar}}\Psi$ and $n_m = Rn$, can be written in a discrete form as:

$$i\frac{\partial \psi_m}{\partial t} = \left(-\hat{D} - i\gamma_1 + in_m + |\psi_m|^2 + \alpha n_m\right)\psi_m, \tag{5.38}$$

$$\frac{\partial n_m}{\partial t} = -\left(\gamma_2 + \beta|\psi_m|^2\right)n_m + P_m. \tag{5.39}$$

where $\hat{D}\psi_m = \sigma(\psi_{m+1} + \psi_{m-1} - 2\psi_m)$ is the operator of the discrete diffraction, $\sigma = \frac{\hbar}{2m}$ is the coupling strength of neighbouring potential wells (depending on the effective mass of polaritons), $\gamma_1 = \gamma_c$ is the loss rate of coherent polaritons, $\alpha = \frac{2g_r}{\hbar R}$ represents the nonlinear interaction of coherent polaritons and incoherent reservoir excitons contributing to the blue shift, $\gamma_2 = \gamma_r$ is the loss rate of incoherent reservoir excitons, $\beta = \frac{\hbar R}{g_c}$ is the condensation rate defining the additional damping rate of the incoherent polaritons caused by their condensation into the coherent polaritons, $P_m = RP$ is the pumping rate. The values of the parameters used in this model are $\alpha = 1.824$, $\beta = 1.0965$, $\gamma_1 = 1$, and $\gamma_2 = 1.5$.

To get a deeper understanding of the dynamics of condensates we first seek the stationary solution in the form

$$\psi_m(t) = \psi_s e^{-i\omega t + iQm}, \tag{5.40}$$

$$n_m(t) = n_s, \tag{5.41}$$

where Ψ_s is the stationary profile of coherent condensates, n_s is the stationary profile of incoherent reservoir excitons, ω is the eigenfrequency of condensates, and Q is the phase difference between condensates at neighbouring sites. Substituting the ansatzes (5.40) and (5.41) into the discrete model (5.38) and (5.39), an eigenfunction can be obtained and solved numerically. The detailed method is introduced in Chapter 3.

A perturbation can then be added into the stationary solution for the stability analysis in the form

$$\psi_m(t) = \left(\psi_s + \delta\Psi e^{-iqm}e^{\lambda t}\right)e^{-i\omega t + iQm}, \tag{5.42}$$

$$n_m(t) = n_s + \delta n e^{-iqm}e^{\lambda t} \tag{5.43}$$

where $\delta\Psi$ is the amplitude of the perturbation in condensates, δn is the amplitude of the perturbation in reservoir excitons, q is the phase difference between neighbouring sites of the

perturbation, and λ is the instability growth rate. As we introduced in Chapter 3, one can obtain the instability growth rate by substituting Eqs. (5.42) and (5.43) into Eqs. (5.38) and (5.39).
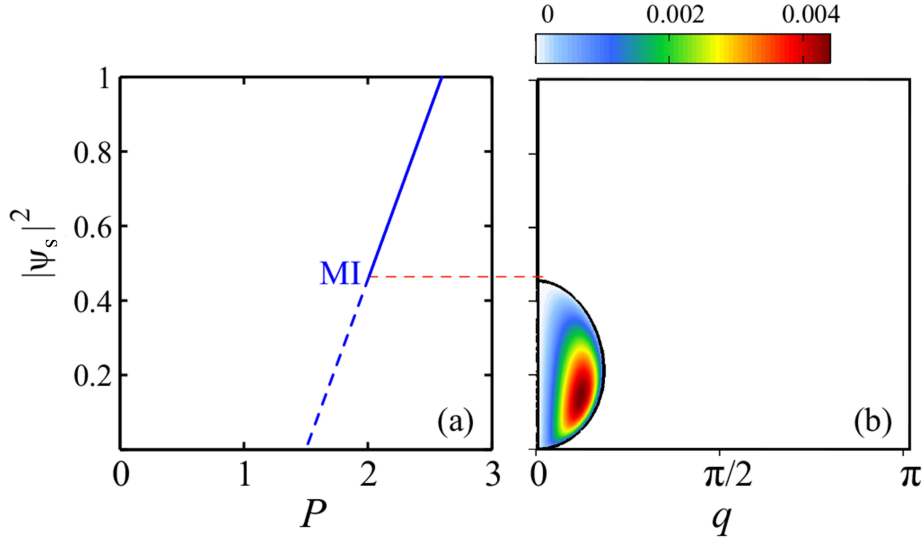

Fig. 5.12 (a) Dependence of polariton density on pump intensity for a steady-state homogeneous solution with zero phase difference $Q = 0$ between neighboring sites at $\sigma = 0.2$. The dashed line represents the modulationally unstable solution. (b) The growth rate of the unstable perturbations on the parameter plane of the polariton density and phase difference between neighboring sites q. From [200].

For stationary uniform solutions when the pump is homogeneous, $P_m = P$, we obtain the following relations

$$n_s = \gamma_1, \tag{5.44}$$

$$|\Psi_s|^2 = \frac{P - \gamma_1 \gamma_2}{\gamma_1 \beta}, \tag{5.45}$$

$$\omega = \alpha \gamma_1 + |\Psi_s|^2 + 2\sigma(1 - \cos Q). \tag{5.46}$$

In this model, we consider two cases for the value of Q, $Q = 0$ and $Q = \pi$. $Q = 0$ represents the case when the neighbouring sites have the same phase distribution, while $Q = \pi$ represents the neighbouring sites having a π phase difference. From Eq. (5.46), the chemical potential is a function of Q. For $Q = 0$, the eigenfrequency is given by

$$\omega_0 = \alpha \gamma_1 + |\Psi_s|^2, \tag{5.47}$$

and for $Q = \pi$,

$$\omega_\pi = \alpha \gamma_1 + |\Psi_s|^2 + 2\sigma. \tag{5.48}$$

The difference between ω_0 and ω_π becomes larger for stronger coupling strength σ. However, the density of condensates, $|\Psi_s|^2$, and the density of reservoir excitons, n_s, are independent of Q as presented in Eqs. (5.44) and (5.45). The dependence of condensate density on pumping rate is shown in Fig. 5.12(a).
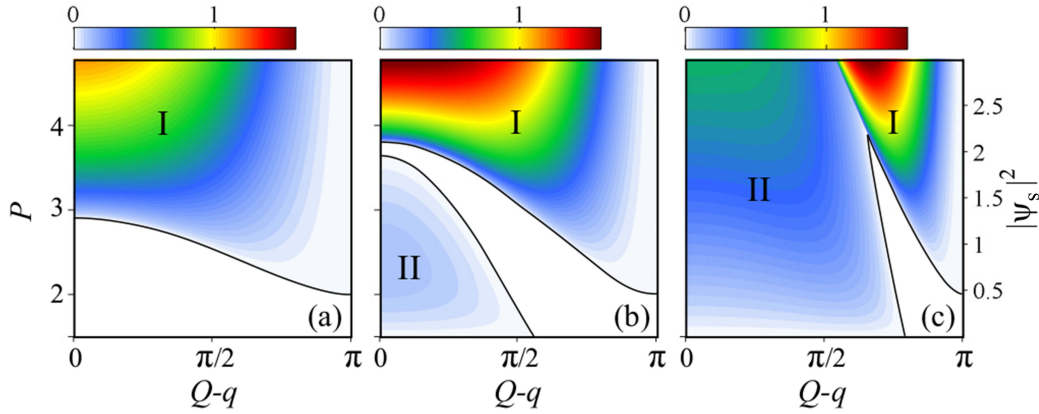

Fig. 5.13 Stability diagram for staggered solution ($Q = \pi$). The peak value of the growth rate on the parameter plane of the pump intensity and phase difference between neighboring sites for perturbation, $Q - q$, for (a) $\sigma = 0.2$, (b) $\sigma = 0.5$, and (c) $\sigma = 2.0$. Black curves correspond to the boundaries of the instability regions. From [200].

The stability of uniform solutions for both $Q = 0$ and $Q = \pi$ cases are shown in Figs. 5.12 and 5.13 for different coupling strength. For a weaker coupling strength, $\sigma = 0.2$, the uniform solutions for $Q = 0$ are stable when the pump intensity is larger [Fig. 5.12(a) and 5.12(b)], while close to the condensation threshold the uniform solutions becomes unstable. This result is opposite to that found in the case of $Q = \pi$. It shows clearly that in Fig. 5.13(a) the solutions are stable when the pump intensity is just above the condensation threshold. This means that when the pump intensity is smaller an unstable uniform solution with $Q = 0$ jumps to the stable uniform solution with $Q = \pi$. Similarly, an unstable solution with $Q = \pi$ jumps to the corresponding stable solution with $Q = 0$ under the larger pump intensity.

When the coupling strength between neighbouring sites is stronger, $\sigma = 0.5$ for instance, the uniform solutions with $Q = 0$ are always stable. The unstable region for $Q = \pi$ is shown in Fig. 5.13(b). There is an additional unstable region (region "II"), which leads to the whole existence region being unstable. However, there is a stable gap between the unstable regions in Fig. 5.13(b), which indicates that the uniform solutions can be stable for a certain phase difference, q, of the perturbation. For example, when $Q - q = 0$, there is a small gap between the unstable regions resulting in the solutions in this pump interval being stable. For more stronger coupling strength, the solutions for $Q = 0$ are still stable in the whole existence

domain. For $Q = \pi$ the unstable region "I" decreases, but the unstable region "II" increases so that in this case the stable region is very small [Fig. 5.13(c)].
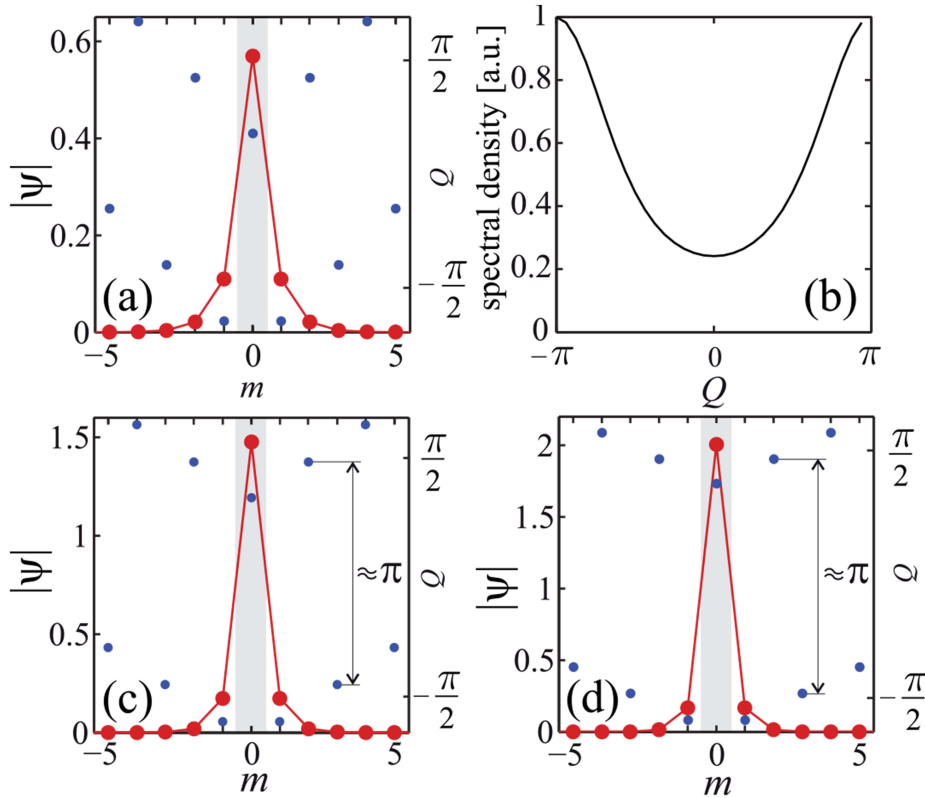
5.3.2 Localized solutions

Fig. 5.14 Distributions of the amplitudes (red circles) and the phases (blue dots) of the stationary solution when only one site is pumped with the pump intensity (a) $P = 2$, (c) $P = 4$, and (d) $P = 6$ at $\sigma = 0.5$. Gray shadows indicate the pump regions. (b) Spatial spectrum of the solution in (a). From [200].

In this part, we consider localized pumps for excitation. If a localized pump excites only one site, the phase difference, Q, is invalid in this case. The steady-state profiles are shown in Fig. 5.14 for different pump intensity. Although only one site is pumped, one can see that some neighbouring sites are still influenced with smaller density due to the coupling strength. It is worth noting that the stronger the pump intensity, the weaker the contrast between the main site and its neighbours. The reason is that as pump intensity increases only the main peak is enhanced, the tails are almost unchanged. This is an important consequence which plays a crucial role in the formation of the finite patterns. The phase difference between neighbouring sites in the tails are always close to π. Figure 5.14(b) shows a spatial spectrum

of the stationary solution in Fig. 5.14(a). It is clear that the maxima of the spectrum are at the boundaries of the Brillouin zone (the π state), which is quite similar to our results in the 1D chain lattices studied in Figs. 5.7 and 5.8.
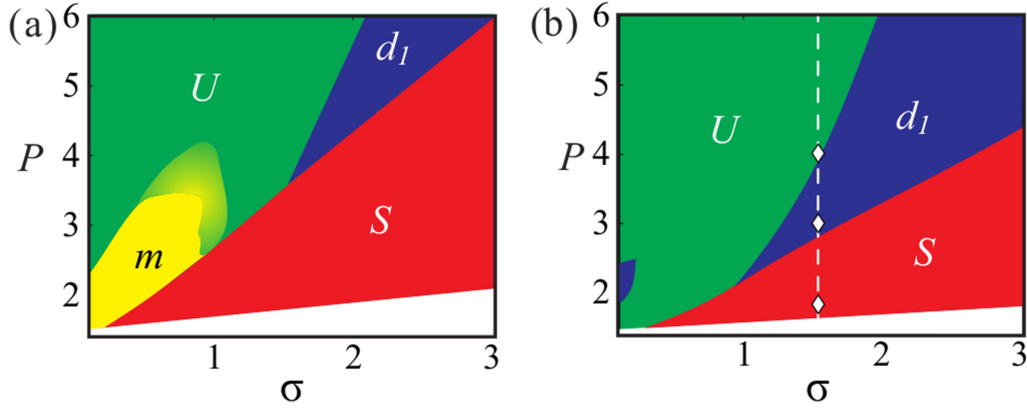

Fig. 5.15 Bifurcation diagrams for (a) two and (b) three pumped sites. The red area marked by S represents the existence of antisymmetric solutions. The green area marked by U represents the existence of symmetric solutions. The yellow area marked by m is the bistable state of antisymmetric and symmetric solutions. The dark blue area marked by d_1 is the existence of asymmetric oscillation solutions. The mixtures of yellow and green show the poorly defined border where a certain kind of solution dominates but the formation of the states of a different kind is sometimes observed in the numerical simulations. From [200].

For the excitation of more than one site, we still consider two phase differences, $Q = 0$ and $Q = \pi$, between the main sites. Figure 5.15 shows the existence regions for different solutions. The symbol "S" represents that the antisymmetric solutions for $Q = \pi$ are stable in this region, the symbol "U" represents that in this region there exists only stable solutions for $Q = 0$. The region "d_1" is an oscillation state where the solution profiles are asymmetric, and "m" in Fig. 5.15(a) indicates that both the solutions of $Q = 0$ and $Q = \pi$ are stable in this region.

Under two localized pumps, except stable S- and U- solutions, there is a bistable state where both these solutions are stable. The bistable solutions are shown in Figs. 5.16(a) and 5.16(b) with a large difference in density. In the tails of both solutions, however, the phase difference is close to π. For the S-solutions, the spectrum has maxima at the $\pm\pi$ states, the boundaries of the Brillouin zone [Fig. 5.16(c)]. In this case condensates occupy the upper state of the corresponding band. This solution always appears at lower pump intensity, which can explain the results in the previous section where the condensates are always excited to the Boundary of the first Brillouin zone in the 1D chain under smaller pump intensity. The stable region of the S-solution increases with the coupling strength. On the contrary, the maxima in the spectrum of the U-solution is in the center of the Brillouin zone, the lower

state of the corresponding band, and it appears at higher pump intensity. The stable region for the U-solution reduces as σ increases. An oscillation solution appears for stronger coupling strength in Fig. 5.15(a), which is a transition state of S- and U-solutions. In is region there are no stable steady-state solutions and the oscillation solutions are asymmetric, which is similar to the dynamics in Fig. 5.17(c) and 5.17(d).
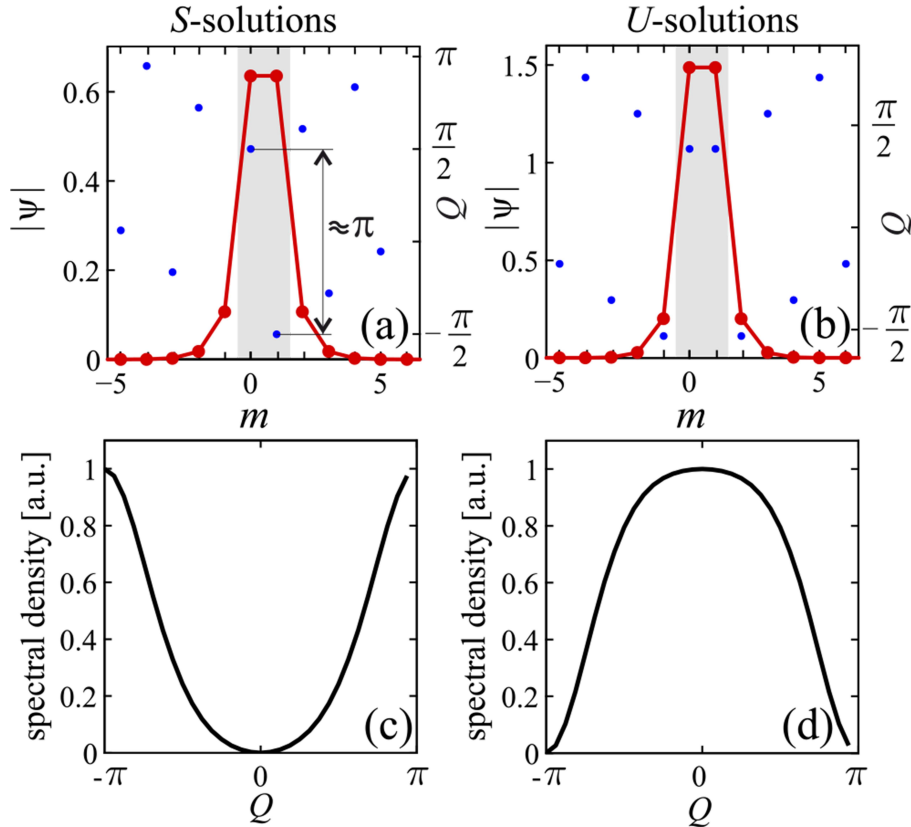

Fig. 5.16 Distributions of the amplitudes (red circles) and the phases (blue dots) of the stationary (a) S and (b) U solutions when two sites are pumped with $P = 2$ and $\sigma = 0.5$. (c), (d) The spatial spectra corresponding to the solutions in (a) and (b), respectively. From [200].

For three site pumping, as shown in Fig. 5.15(b), the bistable region disappears. The stable region for the U-solution is almost the same, while the stable region for the S-solution becomes smaller when compared to Fig. 5.15(a). In this case, a part of the S-solutions is replaced by the oscillation solutions. As we discussed above, the S-solution is stable when the pump intensity is slightly over the condensation threshold, which is also applicable when pumping multiple sites. For the S-solutions, it is clear that condensates are excited to the boundary of the Brillouin zone as shown in Fig. 5.17(b). Increasing the pump intensity, a fraction of the condensates shift to the lower energy states [Fig. 5.17(d)] forming an oscillation state due to the beating of the three energy states. One can see in Fig. 5.17(c)

that this oscillation profile is asymmetric. For much larger pump intensity, all condensates
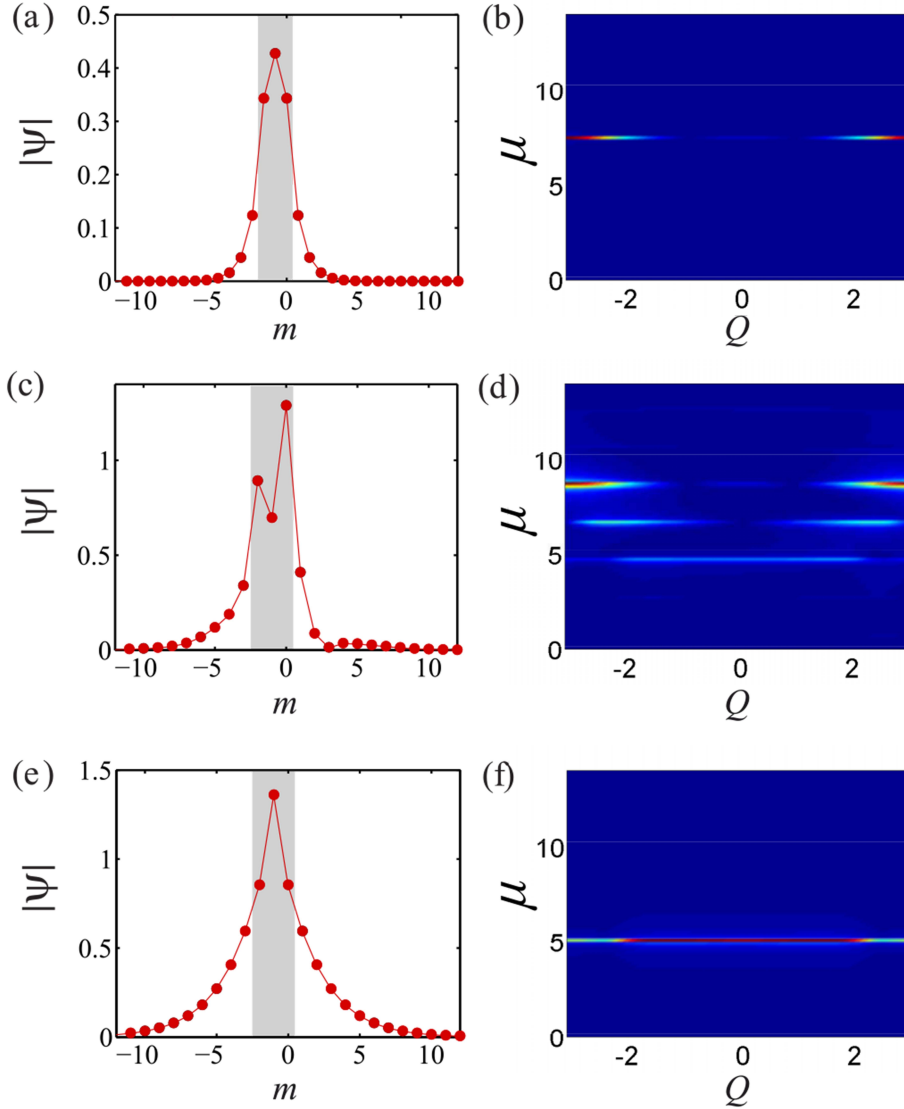
Fig. 5.17 Distributions of the (a,c,e) amplitudes and (b,d,f) the spectra for three pumped sites with relatively strong coupling $\sigma = 1.5$. (a,b) The S-solution at $P = 1.8$. (c,d) The oscillation solution at $P = 3$. (e,f) The U-solution at $P = 4$. These parameters correspond to the points in Fig. 5.15(b). From [200].

occupy the lowest energy state forming a symmetric U-solution. These excitation dynamics related to the pump intensity are in very good agreement with the dynamics of condensates loaded into the 1D chains. Figures 5.17(a) and 5.17(e) indicate that the stable U-solution at larger pump intensity process a longer tail than the stable S-solution at smaller pump intensity under the same coupling strength. This property is different from that under one site pumping in Fig. 5.14, where the tail becomes shorter at larger pump intensity. The reason is

that when more sites are pumped the surrounding density is lifted due to the continuity of a wavefunction. It is also different from that of two solutions in the bistable region under two site pumping in Figs. 5.16(a) and 5.16(b) in which their relative tails are very similar. It is demonstrated that the discrete model is useful for intuitive understanding of the relaxation dynamics of polariton condensates in tight-trapping potentials.

5.4   Chapter summary and concluding remarks

In this chapter we have investigated the nonlinear dynamics of polariton condensates in both weak-contrast and tight-trapping periodic potentials. In the weak-contrast 1D periodic potential considering only the first three spatial harmonics provides a simplified mean-field model. In this simplified model analytical expressions for the relevant eigenstates of the condensates are obtained. We have investigated robust oscillation between different eigenstates, and the numerical results are supported by the analytical analysis. The oscillation dynamics influenced by incoherent reservoir and potential depth were also discussed. It is shown that the simplified model is in good agreement with the full GP model.

In the tight-trapping 1D chain lattices, we studied the linear band structure and the relaxation dynamics of condensates. Under narrower pumps, only the fundamental modes can be formed at the boundary of the first Brillouin zone. These modes switch to the ground state at larger pump intensity. Under broader pumps, the higher modes (dipoles) are excited along and perpendicular with the chain array. Importantly, we find the Talbot effect in the 1D chain due to the interference of condensates leaking from the potential barriers.

To understand intuitively the excitation dynamics of condensates in the tight-binding model, we develop a discrete model. This model shows that low intensity pumping results in an excited state with spatial spectra having maxima at the edge of the Brillouin zone forming the staggered (antisymmetric) state. For larger pump intensity, antisymmetric solutions are unstable and the condensation continues towards the unstaggered ground (symmetric) state. The relaxation dynamics found in the discrete model agree very well with the dynamics of condensates loaded into the chain lattices when considering only the fundamental modes.

Chapter 6

Symbiotic solitons and vortices in binary condensates

In the previous chapters, we studied the nonlinear dynamics of polariton condensates in both uniform microcavities and microcavities with periodic modulation in the scalar case. In this chapter, we investigate the dynamics of polariton condensates considering the polarization (spin) effect. It is known that spinor condensates have not only intra-species repulsion resulting in the defocusing nonlinearity but also the inter-component cubic attraction introducing the focusing nonlinearity into the polariton system. The attractive interaction results from the Feshbach resonance which applies to the inter-component interaction in binary atomic condensates. This property suggests a new method for the creation of symbiotic solitons, supported solely by the attraction between two components in binary condensates if the attraction can overcome the intrinsic repulsion in each of them. The objective of the present chapter is to develop the concept of symbiotic solitons under both focusing and defocusing nonlinearities. To secure the stability of the 2D solitons against critical collapse, a lattice potential must be included into the system. The method for implementing a lattice potential was discussed in detail in Chapter 5.

In binary polariton condensates, we numerically investigate fundamental solitons and vortices, as well as self-trapped modes with hidden-vorticity (HV). The solution families include both gap solitons and regular solitons concerning the band-gap spectra of the linearized system. It is found that symbiotic fundamental solitons, both symmetric and asymmetric ones, are completely stable. The vortices can be stable when the cross-component attraction is stronger than the intra-species repulsion, while the HV modes may be stable in the opposite case. We also analytically investigate the existence, stability, and dynamics of solitons and vortices by means of a variational approximation (VA). It is found that the analytical VA results have a very good agreement with the numerical results.

6.1 The binary model and variational approximation

In Eqs. (2.29) and (2.30), the loss and gain play an important role in the relaxation dynamics of condensates. They may be neglected if the pumping gain approximately compensates the loss of condensates. As discussed above, considering the spin effect of polaritons the cross-species attraction contributes additional nonlinearity beyond the Hartree-Fock approximation. The attractive focusing nonlinearity has the opposite sign with the repulsive defocusing nonlinearity. The dynamics of coherent microcavity polariton condensates in the spinor case are then modeled by the symmetric pair of localized, coupled, nonlinear Schrödinger equations,

$$i\frac{\partial \phi}{\partial t} = -\nabla^2 \phi + |\phi|^2 \phi - g|\psi|^2 \phi + V(x,y)\phi, \tag{6.1}$$

$$i\frac{\partial \psi}{\partial t} = -\nabla^2 \psi + |\psi|^2 \psi - g|\phi|^2 \psi + V(x,y)\psi. \tag{6.2}$$

where $\phi(x,y,t)$ and $\psi(x,y,t)$ are the coherent wavefunctions of the two components. It is assumed that the self-interaction of each component is repulsive, while the cross-interaction is attractive, represented by $g > 0$. Here, g is a real parameter under the assumption that the loss of condensates is density-independent. There is a mechanism that may give rise to effective attraction in the polariton condensates was proposed in Ref. [158–160]. The lattice potential $V(x,y)$ is taken in the usual form

$$V = -\left[\cos\left(2\pi x/l\right) + \cos\left(2\pi y/l\right)\right], \tag{6.3}$$

where $l = 10$ is the spatial period. The depth of the potential, $V_{\max} - V_{\min} = 4$, is fixed by means of the remaining scaling invariance. At the origin, $x = y = 0$, where the center of the soliton will be placed, the lattice potential has a local minimum. It is worth noting that the shape of the lattice, for example, quadratic, hexagonal, radial, or anisotropic, adopted here will have no bearing on the results because they are used only for the control of solutions in case of collapse. Equal coefficients in front of the Laplacians in both equations imply that the spinor describes the two spin states of excitons in the polariton gas.

To analytically study the localized solutions of Eqs. (6.1) and (6.2), we seek the stationary solution in the form of

$$\phi(x,y,t) = e^{-i\lambda t}u(x,y), \tag{6.4}$$

$$\psi(x,y,t) = e^{-i\mu t}v(x,y), \tag{6.5}$$

with corresponding eigenfrequencies λ and μ. Following from Eqs. (6.1) and (6.2), the real wavefunctions u and v obey the stationary equations,

$$\lambda u = -\nabla^2 u + u^3 - gv^2 u - Vu, \tag{6.6}$$

$$\mu v = -\nabla^2 v + v^3 - gu^2 v - Vv. \tag{6.7}$$

For these equations, the corresponding phenomenological system Lagrangian can be defined as

$$2L = \int\int dxdy \left\{ (\nabla u)^2 + (\nabla v)^2 + \frac{1}{2}\left(u^4 + v^4\right) - gu^2 v^2 \right.$$
$$\left. - \left[\cos\left(\frac{2\pi x}{P}\right) + \cos\left(\frac{2\pi y}{P}\right)\right]\left(u^2 + v^2\right) - \left(\lambda u^2 + \mu v^2\right)\right\}. \tag{6.8}$$

In the following we apply a variational approach to solve Eqs. (6.6) and (6.7) for both fundamental solitons and vortices. For fundamental solitons, the simplest Gaussian ansatz is adopted, with amplitudes A, B and radial widths a, b:

$$u = A\exp\left(-\frac{x^2 + y^2}{2a^2}\right) \tag{6.9}$$

$$v = B\exp\left(-\frac{x^2 + y^2}{2b^2}\right). \tag{6.10}$$

According to the ansatz, the following norms in the two components are obtained:

$$M = \int\int u^2(x,y)\,dxdy = \pi A^2 a^2 \tag{6.11}$$

$$N = \int\int v^2(x,y)\,dxdy = \pi B^2 b^2. \tag{6.12}$$

The case $M = N$ corresponds to the symmetric solutions. If $M \neq N$, we define the asymmetry ratio $R = N/M$ and $0 < R \leq 1$. The substitution of ansatzes (6.9) and (6.10) into Lagrangian (6.8) and subsequent integration yields the following effective Lagrangian:

$$2L_{\text{eff}} = -\lambda M - \mu N - 2M\exp\left(-\frac{\pi^2 a^2}{P^2}\right) - 2N\exp\left(-\frac{\pi^2 b^2}{P^2}\right)$$
$$- \frac{g}{\pi}\frac{MN}{a^2 + b^2} + \frac{M^2}{4\pi a^2} + \frac{N^2}{4\pi b^2} + \frac{M}{a^2} + \frac{N}{b^2}. \tag{6.13}$$

The first pair of variational equations following from Eq. (6.13) make it possible to express a^2 and b^2 in terms of M and N: $\partial L_{\text{eff}}/\partial\left(a^2\right) = \partial L_{\text{eff}}/\partial\left(b^2\right) = 0$

$$\frac{2\pi^2}{P^2}\exp\left(-\frac{\pi^2 a^2}{P^2}\right) + \frac{g}{\pi}\frac{N}{(a^2+b^2)^2} = \frac{M+4\pi}{4\pi a^4}, \tag{6.14}$$

$$\frac{2\pi^2}{P^2}\exp\left(-\frac{\pi^2 b^2}{P^2}\right) + \frac{g}{\pi}\frac{M}{(a^2+b^2)^2} = \frac{N+4\pi}{4\pi b^4}. \tag{6.15}$$

For a given M and N, a^2 and b^2 can be found by means of a numerical solution of the algebraic system Eqs. (6.14) and (6.15). The chemical potentials, λ and μ, do not appear in Eqs. (6.14) and (6.15). They are produced by the second pair of the variational equations: $\partial L_{\text{eff}}/\partial M = \partial L_{\text{eff}}/\partial N = 0$

$$\lambda = -2\exp\left(-\frac{\pi^2 a^2}{P^2}\right) - \frac{g}{\pi}\frac{N}{a^2+b^2} + \frac{M+2\pi}{2\pi a^2}, \tag{6.16}$$

$$\mu = -2\exp\left(-\frac{\pi^2 b^2}{P^2}\right) - \frac{g}{\pi}\frac{M}{a^2+b^2} + \frac{N+2\pi}{2\pi b^2}. \tag{6.17}$$

For given g the first objective of the VA is to identify a region in the plane of (M,N) where the numerical solution of Eqs. (6.14) and (6.15) produce physically relevant solutions, with $a^2, b^2 > 0$. Of course, a^2 and b^2 must be substituted by the above mentioned numerical solution of Eqs. (6.14) and (6.15).

Similarly to the approach for the fundamental solitons outlined above, for vortices we adopt a natural generalization of the Gaussian ansatz:

$$u = A(x+iy)\exp\left(-\frac{x^2+y^2}{2a^2}\right), \tag{6.18}$$

$$v = B(x+iy)\exp\left(-\frac{x^2+y^2}{2b^2}\right). \tag{6.19}$$

The respective norms are obtained as

$$M = \int\int u^2(x,y)\,dxdy = \pi A^2 a^4 \tag{6.20}$$

$$N = \int\int v^2(x,y)\,dxdy = \pi B^2 b^4. \tag{6.21}$$

Substituting ansatzes (6.18) and (6.19) into Lagrangian (6.8), the following effective Lagrangian is obtained:

$$2L_{\text{eff}} = -\lambda M - \mu N - \frac{g}{\pi} \frac{2a^2 b^2 MN}{(a^2+b^2)^3} + \frac{M^2}{8\pi a^2} + \frac{N^2}{8\pi b^2} + \frac{2M}{a^2} + \frac{2N}{b^2}$$
$$- \frac{2M}{P^2}\left(P^2 - a^2\pi^2\right)\exp\left(-\frac{\pi^2 a^2}{P^2}\right) - \frac{2N}{P^2}\left(P^2 - b^2\pi^2\right)\exp\left(-\frac{\pi^2 b^2}{P^2}\right). \tag{6.22}$$

The variational equations for a^2 and b^2 are then produced as $\partial L_{\text{eff}}/\partial\left(a^2\right) = \partial L_{\text{eff}}/\partial\left(b^2\right) = 0$

$$\frac{2\pi^2\left(2P^2 - a^2\pi^2\right)}{P^4}\exp\left(-\frac{\pi^2 a^2}{P^2}\right) + \frac{g}{\pi}\frac{2b^2 N\left(2a^2 - b^2\right)}{(a^2+b^2)^4} = \frac{M + 16\pi}{8\pi a^4}, \tag{6.23}$$

$$\frac{2\pi^2\left(2P^2 - b^2\pi^2\right)}{P^4}\exp\left(-\frac{\pi^2 b^2}{P^2}\right) + \frac{g}{\pi}\frac{2a^2 M\left(2b^2 - a^2\right)}{(a^2+b^2)^4} = \frac{N + 16\pi}{8\pi b^4}. \tag{6.24}$$

Finally, the chemical potentials for the two components of the vortex are produced according by the remaining variational equations, $\partial L_{\text{eff}}/\partial M = \partial L_{\text{eff}}/\partial N = 0$

$$\lambda = \frac{2\left(a^2\pi^2 - P^2\right)}{P^2}\exp\left(-\frac{\pi^2 a^2}{P^2}\right) - \frac{g}{\pi}\frac{2a^2 b^2 N}{(a^2+b^2)^4} + \frac{M + 8\pi}{4\pi a^2}, \tag{6.25}$$

$$\mu = \frac{2\left(b^2\pi^2 - P^2\right)}{P^2}\exp\left(-\frac{\pi^2 b^2}{P^2}\right) - \frac{g}{\pi}\frac{2a^2 b^2 M}{(a^2+b^2)^4} + \frac{N + 8\pi}{4\pi b^2}. \tag{6.26}$$

Under the VA and the simplest ansatzes for fundamental solitons and vortices, the corresponding norm-dependent eigenfrequencies are obtained. These analytical results are compared to the numerical finding to validate the assumed ansatzes.

6.2   Symbiotic solitons

Numerical solutions are constructed on a finite-size grid that is sufficiently large to avoid influence of boundaries on the localized solutions. Stationary solutions are found starting from a localized input, using the imaginary-time propagation method. The stability of these stationary solution is then tested by simulation of perturbed evolution of Eqs. (6.1) and (6.2) in real time.

First, we look for symmetric fundamental modes with identical stationary wave functions u and v of the two components with equal norms, $M = N$. In the symmetric case, the overall nonlinearity presented in Eqs. (6.1) and (6.2) can be characterized by a single effective

coefficient $g - 1$. Thus, $g > 1$ results in the effective focusing nonlinearity due to self-attraction. For $g < 1$ the strength of the repulsive inter-component interaction is larger than the attractive cross-component interaction such that the net effect in this case is an overall defocusing nonlinearity. Note that the nonlinearity vanishes in the symmetric case for $g = 1$.
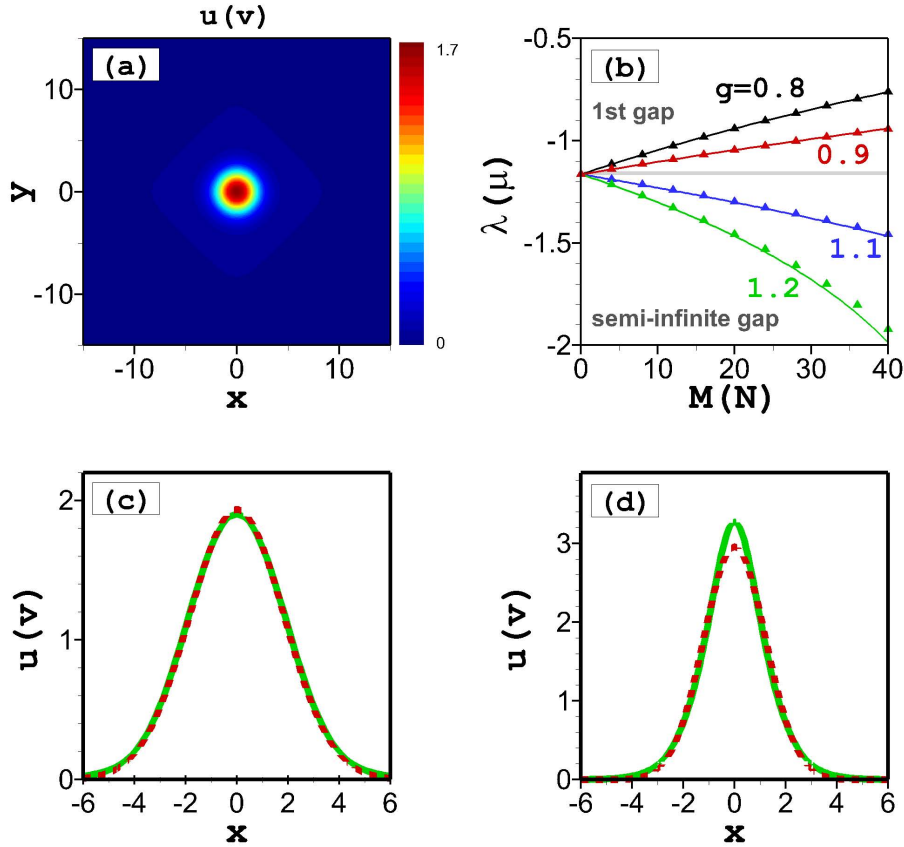

Fig. 6.1 Symmetric solitons. (a) Amplitude distribution of a stable symmetric fundamental soliton for $g = 1.1$ and $M = 20$. (b) Dependence of the norm ($M \equiv N$) on the eigenfrequencies ($\lambda \equiv \mu$) for the family of fundamental symmetric solitons at different values of the cross-attraction coefficient, g. Solid lines depict stable numerical solutions, while triangles represent the corresponding results produced by the VA of Eqs. (6.14)-(6.17). The gray region represents the first band of the lattice-potential spectrum. Comparison of numerical (solid lines) and VA-predicted (dashed lines) profiles of the fundamental symmetric solitons at (c) $g = 0.8$, $M = 40$ and (d) $g = 1.2$, $M = 40$. From [201].

Figure 6.1 shows the numerical results for symmetric fundamental solitons. It is found that the fundamental solitons located in the center of a lattice cell [Fig. 6.1(a)] are stable in their entire existence domain as shown in Fig. 6.1(b). These conclusions comply with the Vakhitov-Kolokolov (VK) criteria, that $dN/d\mu < 0$, for $g > 1$ and the anti-VK criteria, that

$dN/d\mu > 0$, for $g < 1$. The VK and anti-VK criteria are necessary, although not sufficient, stability conditions for solitons supported by focusing and defocusing nonlinearities. Due to the appearance of a periodic potential, a band-gap structure is obtained according to the Bloch's theorem which is introduced in Chapter 5. The very narrow first band of the periodic potential is presented in Fig. 6.1(b), which separates the solitons into two groups. The fundamental solitons found at $g < 1$ corresponding to the effective repulsive nonlinearity are gap solitons. It can be readily checked that values of $\lambda \equiv \mu$ in Fig. 6.1(b) for $g < 1$ fall into the first finite bandgap of the spectrum of the linearized symmetric (6.6) and (6.7), while the solitons found at $g > 1$, corresponding to the effective attractive nonlinearity, belong to the semi-infinite gap.

The analytical results provided by the VA can be seen in Figs. 6.1(b)-6.1(d). It is found that the analytical and numerical results of the VA agree extremely well with their numerical counterparts, especially for the solitons with small norms or under weaker effective nonlinearity [Fig. 6.1(c)]. For larger norms under stronger effective nonlinearity, however, their is a small deviation between these two results [Fig. 6.1(c)], and the main difference between them comes from the center of the solution around $x = 0$. The reason for this is that the solitons with larger norms are affected more strongly by the stabilizing lattice, which leads to the numerical solutions having sharper profiles as shown in Fig. 6.1(d).

Asymmetric solitons, with unequal u and v components, form an especially interesting class of modes in the present model. We start their consideration with the case of $g = 1$, in which symmetric solitons cannot exist. The results for this case are illustrated in Fig. 6.2. It is clear that the width of a profile with a larger norm [Fig. 6.2(a)] is larger than that of its counterpart [Fig. 6.2(b)] with a smaller norm. With $g = 1$ and the asymmetry ratio $0 < R < 1$, roughly speaking, $|\psi|^2 > |\phi|^2$, the model (6.1) and (6.2) then suggest that the defocusing and focusing nonlinearities dominate in the former and latter equations, respectively. This conclusion is also confirmed by the behavior of the eigenfrequencies λ and μ, comparing their behavior in Figs. 6.2(c) and 6.2(d) with that observed in Fig. 6.1(b) for $g < 1$ and $g > 1$, respectively. Thus, asymmetric solitons with $g = 1$ may be considered as bound states of gap solitons and regular ones. The respective chemical potentials, λ and μ, fall respectively, into the first finite gap and semi-infinite gap. Similar to their symmetric counterparts, it has been found that the asymmetric fundamental solitons are also stable in their entire existence region. Intuitively, this conclusion agrees with the fact that the $\lambda(M)$ and $\mu(M)$ dependencies in Figs. 6.2(c) and 6.2(d) satisfy the anti-VK and VK criteria, respectively.

The analytical results produced by the VA for these asymmetric modes are also found to be in excellent agreement with the numerical results, which can be seen from the comparison of the analytical and numerical results for varying eigenfrequencies λ and μ in Figs. 6.2(c)

and 6.2(d). A detailed comparison demonstrates that if the u component becomes broader as the asymmetry ratio R is decreased [Fig. 6.2(c)], this component is more strongly affected by the underlying lattice potential. Therefore, the results of the numerical modeling and the VA modeling diverge for stronger nonlinearity in the limit of $R \to 0$.
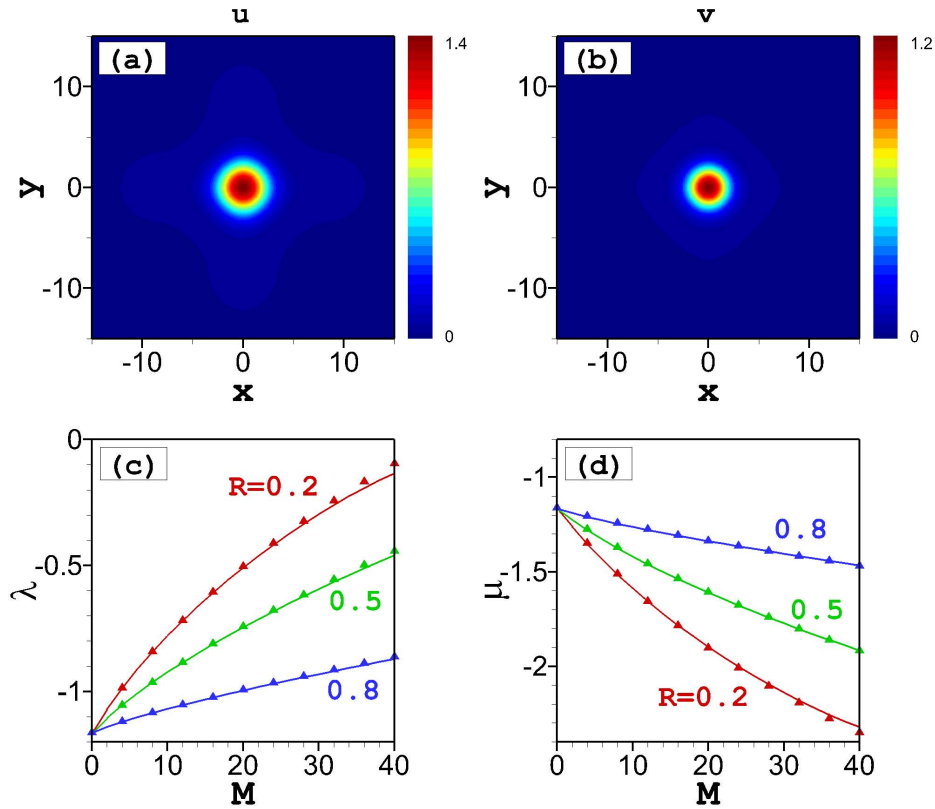

Fig. 6.2 Asymmetric solitons. Amplitude distributions of the (a) u and (b) v components of the stable asymmetric fundamental soliton with $g = 1$, $N = 10$, and $M = 20$ (the asymmetry ratio $R = 0.5$). Dependences between the larger norm (M) and the eigenfrequencies (c) λ and (d) μ for different values of the asymmetric ratio at $g = 1$. Solid lines represent stable numerical solutions, and triangles represents the VA-predicted analytical results from Eqs. (6.14)-(6.17). From [201].

6.3 Symbiotic vortices

A lattice potential can support vortex states with a complex structure. In this model, we consider that the vortices have only vorticity $S = \pm 1$. Unlike the fundamental solitons, the vortices [Figs. 6.3(a) and 6.3(b)] corresponding to $g > 1$ and $g < 1$ stay, respectively, in the

first and second finite bandgaps, which are separated by the narrow second band as shown in Fig. 6.3(c). The vortices are unstable for $g < 1$ when they belong to the second bandgap. Figure 6.3(c) demonstrates that families of the symmetric vortex solitons are stable at $g > 1$ in the first gap, in a finite interval of

$$N_{\min}(g) < N < N_{\max}(g), \tag{6.27}$$

where $N_{\max}$ decreases sharply with the increase of g, while $N_{\min}$ is almost unchanged as

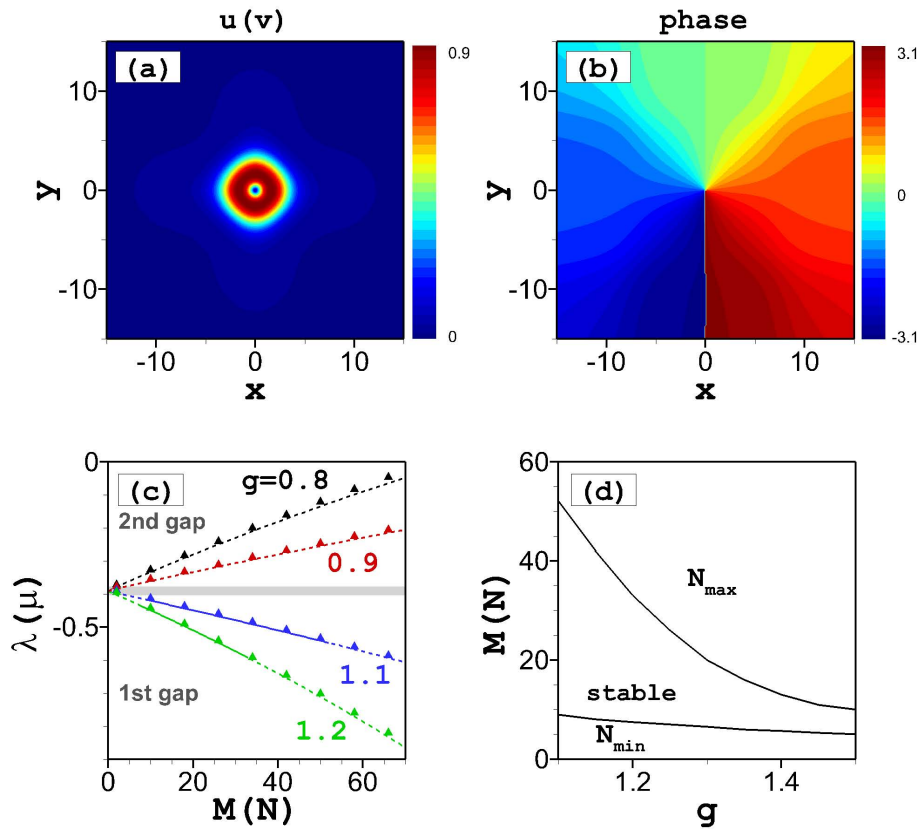

Fig. 6.3 Symmetric vortices. (a) Amplitude and (b) phase distributions of a numerical stable symmetric vortex solitons for $g = 1.1$ and $M = 20$. (c) Dependence of the norm ($M \equiv N$) on the eigenfrequency ($\lambda \equiv \mu$) of the vortex solitons for different values of g. Solid and dashed lines represent stable and unstable vortices, respectively, while triangles depict the corresponding VA results from Eqs. (6.23)-(6.26). The gray regions represents the second band of the lattice-potential spectrum. (d) Dependence of the stability boundaries of vortices, $N_{\max}$ and $N_{\min}$, on g. From [201].

presented in Fig. 6.3(d). This means that the stable region of symmetric vortices decreases as g increases. Direct simulations demonstrate that unstable vortices spontaneously evolve into

robust randomly vibrating single or multi-peak patterns, which are asymmetric with respect to the two components. It is usually assumed that gap solitons have a loosely bound shape, with many inner oscillations. As Fig. 6.3 shows, the version of the VA developed for the vortex solitons also provides a very good accuracy in comparison to the numerical findings.

For asymmetric vortices, the spatial profiles of the u and v components feature small differences as shown in Figs. 6.4(a) and 6.4(b), while the phase distributions are virtually identical in both components carrying the same vorticity, $S = +1$ or -1. Similar to what is shown above for the fundamental solitons in the case of $g = 1$, when the solutions are asymmetric ($M \neq N$), the repulsive and attractive interactions dominate in the different components, resulting in different dependence between the chemical potentials and the norms as illustrated in Fig. 6.4(c). One can see the blue shift of the eigenfrequency, λ, as the norm increases because of the domination of the repulsive interaction. When the attractive interaction dominates, the eigenfrequency, μ, shows the red shift as the norm increases.

The comparison of the VA and numerical results for asymmetric vortices is shown in Fig. 6.4(c). In the asymmetric case, the vortex component u with a larger norm is broader than its counterpart with a smaller norm v. Also in this case, due to the influence of the underlying lattice, the agreement of the exact numerical solution with the simplest vortex ansatzes (6.18) and (6.19), gets worse with increasing vortex size. Therefore, the agreement of the VA and numerical results for the v component with smaller size is better than those of the u component with larger size [Fig. 6.4(c)]. Generally, the size of the vortices is larger than that of the fundamental solitons, therefore the overall agreement of the VA and numerical results for asymmetric vortices in Fig. 6.4(c) is somewhat poorer than for the asymmetric fundamental solitons in Figs. 6.2(c) and 6.2(d).

Figure 6.4(d) shows the stability and instability regions of the asymmetric vortices, depending on the asymmetry ratio R, for $g = 1$. When $R \to 1$, the vortices become unstable because the nonlinearity effectively disappears when the solutions approach the symmetric case with $g = 1$. When $R \to 0$, the model reduces to a single-component system with a defocusing nonlinearity, in which the vortices are also unstable. The smallest norm for stable vortices is found around $R = 0.7$.

An example of the stability region of vortices for $g > 1$, $g = 1.1$ for instance, is shown in Fig. 6.4(e). Starting from the symmetric case with $R = 1$, the stability range slightly widens initially with the increase of the asymmetry (decrease of R). The stability region then gradually decreases with further decrease of R until all stable solutions disappear at $R < 0.6$. For $g = 1.2$, as shown in Fig. 6.4(f), the stability region decreases monotonically with increasing asymmetry, again shrinking to nothing at $R \approx 0.6$. At $g > 1$, smaller asymmetry ratio R implies domination of the attractive nonlinearity in (6.2), eventually leading to an
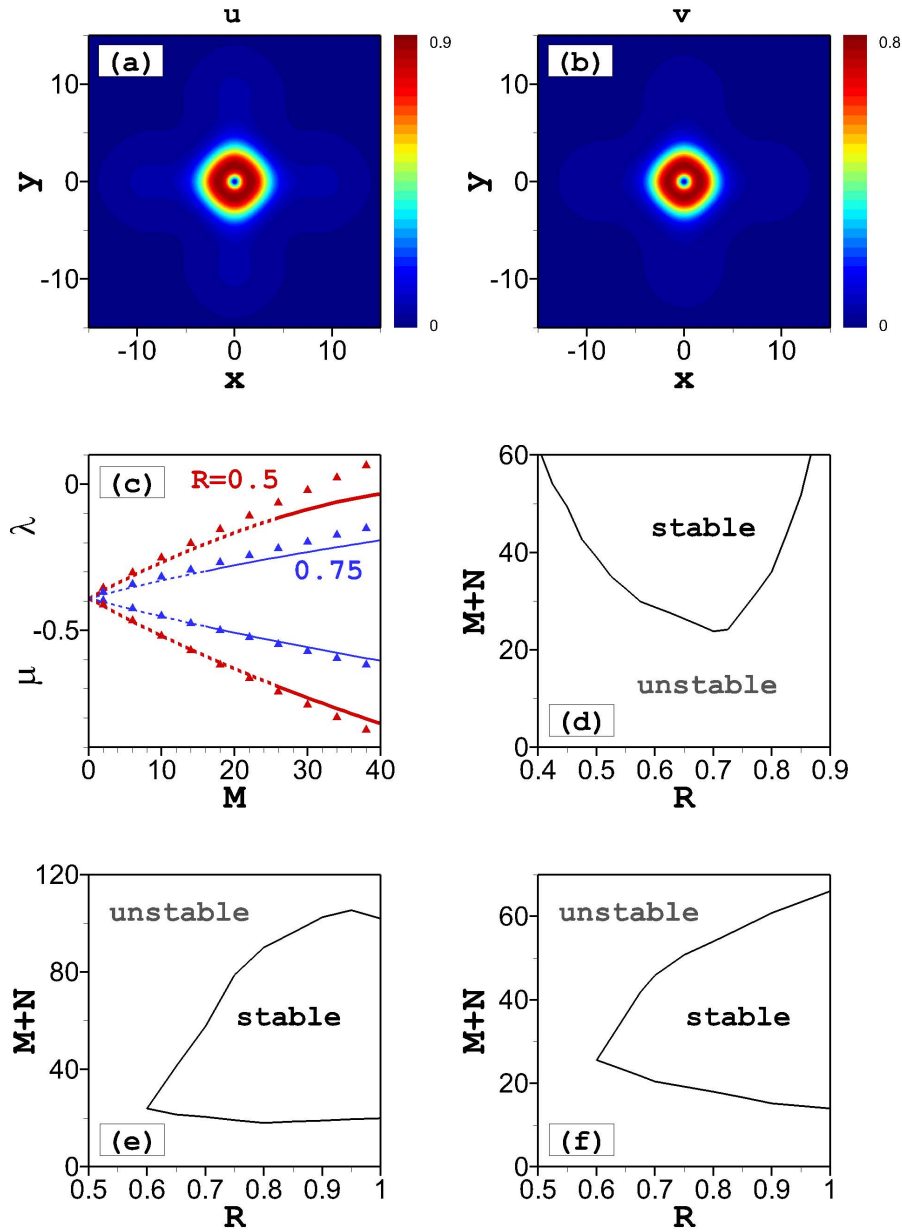
Fig. 6.4 Asymmetric vortices. Amplitude distributions of the (a) u and (b) v components of an asymmetric ($R = 0.5$) vortex soliton at $g = 1$ and $M = 20$. (c) Dependence of the norm (M) on the eigenfrequencies (μ and λ) of the two components of the vortex for different asymmetry ratios at $g = 1$. Solid and dashed lines denote stable and unstable solutions, respectively, while triangles represent the VA results from Eqs. (6.23)-(6.26). Stable and unstable regions of vortices for (d) $g = 1$, (e) $g = 1.1$, and (f) $g = 1.2$. From [201].

instability of the v component. It is worth noting that the fact that vortices are unstable for larger norms in Figs. 6.4(e) and 6.4(f) is in contrast to the results for $g = 1$ as shown in Fig. 6.4(d). Roughly speaking, the stability regions for $g > 1$ shown in Figs. 6.4(e) and 6.4(f) are rotated by 90° in comparison with their counterpart shown in Fig. 6.4(d) for $g = 1$. When $g < 1$, all asymmetric vortices are unstable, similar to the results in the symmetric case.

6.4   Hidden-vorticity modes
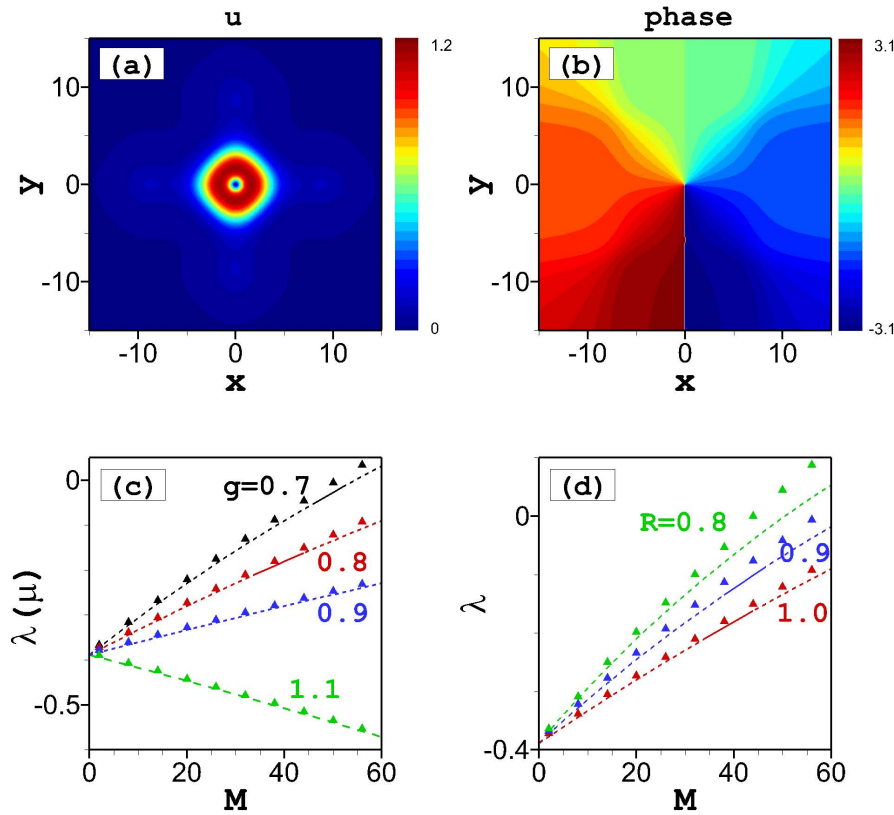
Fig. 6.5 Hidden vorticity modes. (a) Amplitude and (b) phase distributions of symmetric ($R = 1$) stationary solutions for the u-component of an vortex-antivortex pair at $g = 0.8$ and $M = 35$. Dependences of the norm (M) on the eigenfrequency (λ) of vortex-antivortex pairs for (c) different nonlinearity at $R = 1$ and (d) different asymmetric ratio at $g = 0.8$. Solid lines are stable numerical solutions, while dashed lines are unstable solutions. Triangles depict analytical results of Eqs. (6.23)-(6.26). From [201].

Besides the vortices having the same vorticity in two components for both symmetric and asymmetric solutions, in this section, we introduce a hidden-vorticity state as illustrated

in Fig. 6.5, where the vorticities of the two components have opposite vorticity. In the symmetric case ($M = N$), both components have the same spatial profiles, so that the whole solution carries zero angular momentum with $S = 0$, as shown in Fig. 6.5(a). It is found that the vortex-antivortex pairs are unstable when the focusing nonlinearity dominates with $g > 1$. However, they may be stable for the overall-defocusing system with $g < 1$ as shown in Fig. 6.5(c). This is quite different from the results of the state with explicit vorticity with $S = 1$ in both components as discussed in Fig. 6.3. The stable vortex-antivortex pairs are also found at $g < 1$ in the weakly asymmetric case with asymmetry ratios R slightly smaller than 1 as shown in Fig. 6.5(d). When the norm difference between the two components becomes larger, the profiles of vortex and antivortex are dismatched, so that they are destroyed by each other and become unstable.

The VA results of the vortex-antivortex pairs are also given by Eqs. (6.25) and (6.26). The analytical results are in very good agreement with the numerical solution in the symmetric case with $M = N$, as shown in Fig. 6.5(c). In the asymmetric case, $M \neq N$, the difference between the two results becomes more apparent [Fig. 6.5(d)] because the size of one component of the solution is larger and more strongly influenced by the stabilizing lattices.

6.5   Chapter summary and concluding remarks

In this chapter, we demonstrate the existence of stable symbiotic solitons and vortices in the two-component spinor system with intra-species repulsion and cross-component attraction in the presence of a stabilizing lattice potential. The fundamental solitons are always stable in both symmetric and asymmetric cases. Vortex solitons with the same vorticity in both components are stable when the attractive cross-component interaction is stronger than the intra-species repulsion. In contrast, the modes with opposite vorticities (HV modes), in the two components can be stable only when the repulsive interaction dominates. Analytical expressions are obtained based on the VA. It shows that the VA results agree very well with the numerical results for fundamental solitons and vortices, as well as HV modes in both symmetric and asymmetric cases.

Chapter 7

Conclusion and perspective

Conclusion

The dynamics of nonequilibrium exciton-polaritons has been extensively studied in the last decade. In this thesis we theoretically investigated the nonlinear dynamics of polariton condensates in semiconductor microcavities under homogeneous and localized excitations, as well as the relaxation dynamics of condensates loaded into periodic lattices based on the open-dissipative Gross-Pitaevskii model. The steady-state solutions, including solitons and vortices, of condensates and their stability analysis in homogeneous uniform samples, that is, without external potentials were addressed. Considering the periodic potential, we mainly studied the band-gap structure of polaritons and the transition dynamics of condensates between different energy states, as well as the oscillation dynamics due to the interaction of condensates between different energy states. The more detailed results we obtained in this thesis are summarized below.

The equations of motion of polaritons was derived and analyzed in detail in Chapter 2. We analytically introduced the eigenstates of polaritons in semiconductor microcavities in the strong coupling regime. The approximate derivation of the GPE was given, including relevant parameters according to the equations of motion. Based on the GP model, a series of investigations were under taken in the following chapters.

We started from the simplest case, namely, under homogeneous excitation, and found the steady-state solutions in Chapter 3. Under homogeneous excitation, we found turbulent patterns induced by modulational instability, which appear when the pump intensity is just above the condensation threshold. In addition to stable homogeneous solutions, in the stable region constant pumps also support the formation of vortices due to the initial phase defects. The phase defects can survive because of the feedback between coherent condensates and incoherent reservoirs (nonequilibrium nature). Therefore, massive turbulent vortices are

formed. The vortices with the same topological charge repel each other, while the vortices with opposite charges attract each other. The vortex size becomes larger as the pump intensity decreases. When the pump intensity is just above the MI region, it is difficult to distinguish each vortex due to the overlap of them, so that a spiralling wave, a vortex moving along a circle with a constant speed, can be generated in this case. The spiralling wave drives away the surrounding vortices making the background smooth again.

To stabilize the phase defects, periodic pumps were created by the interference of two (1D) or four (2D) coherent homogenous optical beams. It is found that in the 1D case a periodic pump supports both a pure periodic solution and stable phase defects, known as dark solitons. Under homogeneous excitation, dark solitons are unstable, while under periodic pumps phase defects can be fixed by the periodic reservoir resulting in the formation of stable dark solitons. Regarding the periodic solution as the background, a coherent narrow pulse can be used to create or annihilate a dark soliton in the pump valleys. The creation and annihilation dynamics of phase defects is not available in the 2D case, but one can use coherent pulses to manipulate the phase defects to desired positions. In the periodic background two kinds of vortices are generated with one in the pump valleys having a smaller size, and the other one having a larger size in the pump peaks. The two kinds of vortices are fixed in their own lattices when the pump intensity is not too large. In this condition, a coherent pulse can move a vortex to one of its neighbouring lattices. The vortices also can be incoherently manipulated by switching the 2D pump between lattices and stripes.

In Chapter 4, we studied the formation of crater-shaped vortices under ring-shaped pumps. It is known that a localized pump creates a localized reservoir which can be regarded as an optically induced potential. The shape of the reservoir is similar to that of the pump. The ring-shaped pump creates a similar shaped reservoir which limits massive polariton condensates inside the ring region forming a crater-shaped vortex. Through the stationary solution, we found that the topological charge of vortices depends on the radius of the ring-shaped pump and it, which is a integer, grows with the increase of the pump radius. It is found that the vortices are more unstable when the pump radius is larger, therefore, the topological charge is larger. Due to the symmetry of the system, vortices excited from initial noise can have different charges under the same pump. To control the sign of the topological charge, we found two simple methods. One is that an elliptically incoherent pump can be used to break the radial symmetry of the system leading to the later formed vortex having a specified topological charge. The other one is that when vortices are close to each other phase-locked vortices are formed. Based on the locked phase, vortices can be easily controlled by their neighbours, known as vortex-vortex control.

Apart from the optically induced potentials, we also investigated the dynamics of condensates loaded into external periodic potentials including both weak-contrast and tight-binding lattices, as studied in Chapter 5. In the weak-contrast periodic potentials, we developed a simplified mean-field model, in which we considered only the first three spatial harmonics, and found analytical expressions for the relevant eigenstates of condensates. Under the simplified model we investigated the relaxation dynamics of condensates in the center and at the boundaries of the Brillouin zone. Next, we numerically studied the excitation and oscillation dynamics of condensates under the full GP model. Note that the oscillation at π states happens when the potential is weaker, when the potential is stronger stable oscillation at zero states remains. By comparing these two results, we found that at the π states the oscillation results from the simplified model fully agree with the full GP model, especially at lower pump intensity. For the oscillations at the zero states, the results of the simplified model agree qualitatively with the full GP model due to the stronger potential depth. The simplified model is more accurate when the value of the modulation depth is smaller.

In the stronger periodic (tight-trapping) potentials, we numerically studied the loading of polaritons into 1D chain lattices. We observed the clear band-gap structure in this case and the transition of polaritons from an incoherent state into coherent condensates. When the pump intensity is just above the condensation threshold, polaritons condensate to the excited state of the first band, where only the fundamental modes are excited under narrow pump spots. As pump intensity increases, condensates undergo further transitions toward the lower energy states. When the pump intensity is very large, almost all condensates occupy the ground state. Under broader pump spots, dipoles are excited in each trap. For an elliptical pump covering several traps of the lattices, condensates are excited out of the traps and propagate perpendicularly to the lattice array forming the Talbot pattern. By comparing with the experiments, we found that our theoretical model can perfectly describe the dynamics of condensates in the periodic potentials.

To intuitively understand the building up of condensates trapped in tight-trapping lattices, we developed a discrete model. In this model, we investigated the excitation dynamics of condensates under uniform and localized pumping, when neglecting the higher modes in each trap. The phase difference between the neighbouring potential traps can be 0 or π, corresponding to the ground and excited states, respectively. Under uniform pumping, there is a modulational instability reigion close to the condensation threshold when the neighbouring traps have the same phase and weaker coupling strength. For stronger coupling strength the homogeneous solutions are always stable. Under localized pumping, the solutions with π phase difference, antisymmetric solutions, can be stable when the pump intensity is just above the condensation threshold. When the pump intensity is larger, the solutions with

the same phase, symmetric solutions, are stable. These results can be used to explain the phenomena obtained in recent experiments.

In the scalar case, polaritons show only the repulsive interaction, which results in the nonlinearity of the system being defocusing. In Chapter 6, we considered the spin effect of condensates. In the spinor case, the Feshbach resonance leads to attractive interaction between inter-components in binary condensates, thereby developing a focusing nonlinearity in the polariton system. Under both focusing and defocusing nonlinearities, we numerically demonstrated the existence of stable symbiotic solitons and vortices in the presence of a stabilizing lattice. The fundamental solitons were shown to be stable in their entire existence domain. The vortex can be stable only when the focusing nonlinearity dominates. Moreover, the stable region decreases as the focusing nonlinearity becomes stronger. We also found the stable HV modes when the system is more defocusing. The analytical results, which have a very good agreement with the numerical findings, of fundamental solitons, vortices, and HV modes were analytically obtained under the VA.

Perspective

Besides the results we obtained about the nonlinear dynamics of condensates, there is still some open problem which should be addressed from my point of view. For example, we found stable dark solitons under the periodic excitation in Chapter 3, it is also worth investigating whether bright solitons can exist in polariton condensates under periodic excitation. We found stable vortices in Chapter 4. It would be interesting to find out whether there still exist another type of stable solution without angular momentum, that is, a rotating and nonrotating bistable state due to the nonlinear effect. One can also try to fabricate different external potentials as introduced in Chapter 5 to develop more interesting properties such as a superlattice containing two different periods and a ring-shaped potential for the investigation of potential-supported vortices, which will be helpful for the design of polaritonic devices. We developed the symbiotic solitons and vortices in binary condensates in Chapter 6. Another question that arises is whether these symbiotic states are still stable if considering the spin-orbit coupling effect of condensates.

Polaritons show very novel properties in the previous investigation, which makes them a promising candidate in the fields of all-optical circuits, logic gate operations, information processing, and quantum simulators. Therefore, in my opinion, further investigation into polaritions, including coherent and incoherent excitation and both scalar and spinor models, is highly warranted.

Acknowledgements

A good environment always improves the researching ability of scientists and encourages the spirit of innovation. I was lucky to be in two such groups, with amazing support of so many persons. I do believe that there is no way I would have finished my thesis without their help. In this section, I would like to thank all the people who helped me during my time as a PhD student.

First I would like to give my sincere gratitude to Prof. Stefan Schumacher who gave me the opportunity to write this thesis in the Department of Physics in the University of Paderborn. Prof. Schumacher has a strong background in solid state physics which helped me a lot in the study of semiconductor physics. By working with him, I learnt not only useful knowledge in physics, but also the serious attitude on scientific research, as well as the rich experience of scientific collaboration. His kind supervision gave me strong confidence in my work, which makes me more interested in scientific research. I have greatly enjoyed working with him.

Next, I gratefully acknowledge Dr. Oleg Egorov in the Institute of Condensed Matter Theory and Solid State Optics (IFTO) in the Friedrich-Schiller-Universität Jena. Dr. Egorov gave me the opportunity to start my doctoral study in Jena and led me into the field of exciton-polaritons in semiconductor microcavities. He guided me patiently and inspired me to innovate boldly in my work. His rich experience in nonlinear dynamics and international collaboration helped me a lot.

I am extremely grateful for the supervision of Prof. Falk Lederer in the IFTO in the Friedrich-Schiller-Universität Jena. Prof. Lederer is a world famous scientist in the field of nonlinear phenomena. I was really honored being his student.

My deepest gratitude goes to Szilvia Mammel who is the secretary in the Abbe Center of Photonics in the Friedrich-Schiller-Universität Jena. Szilvia helped me a lot especially at the beginning of my life in Germany. She solved all the problems I met in Jena and organized everything for me in my previous group. My deepest gratitude also goes to Simone Lange who is the secretary in the Department of Physics in the University of Paderborn for her patience with me and her efficient methods for solving work and daily life problems in

List of Publications

All publications in peer reviewed journals that are directly relevant for this thesis will appear in **bold** letters in the following.

Peer reviewed journals

1. H. Sigurdsson, O. A. Egorov, <u>X. Ma</u>, I. A. Shelykh, and T. C. H. Liew, Information processing with topologically protected vortex memories in exciton-polariton condensates, *Phys. Rev. B* **90**, 014504 (2014).

2. **T. C. H. Liew, O. A. Egorov, M. Matuszewski, O. Kyriienko, <u>X. Ma</u>, and E. A. Ostrovskaya, Instability-induced formation and nonequilibrium dynamics of phase defects in polariton condensates, *Phys. Rev. B* 91, 085413 (2015).**

3. **<u>X. Ma</u>, I.Yu. Chestnov, M.V. Charukhchyan, A.P. Alodjants, and O.A. Egorov, Oscillatory dynamics of nonequilibrium dissipative exciton-polariton condensates in weak-contrast lattices, *Phys. Rev. B* 91, 214301 (2015).**

4. **<u>Xuekai Ma</u>, Ulf Peschel, and Oleg A. Egorov, Incoherent control of topological charges in nonequilibrium polariton condensates, *Phys. Rev. B* 93, 035315 (2016).**

5. **K. Winkler, O. A. Egorov, I. G. Savenko, <u>X. Ma</u>, E. Estrecho, T. Gao, S. Müller, M. Kamp, T. C. H. Liew, E. A. Ostrovskaya, S. Höfling, and C. Schneider, Collective state transitions of exciton-polaritons loaded into a periodic potential, *Phys. Rev. B* 93, 121303(R) (2016).**

6. **A. V. Yulin, I. Yu. Chestnov, <u>X. Ma</u>, S. Schumacher, U. Peschel, and O. A. Egorov, Dynamics of exciton-polaritons in discrete lattices under incoherent localized pumping, *Phys. Rev. B* 94, 054312 (2016).**

7. **T. Gao, E. Estrecho, G. Li, O. A. Egorov, <u>X. Ma</u>, K. Winkler, M. Kamp, C. Schneider, S. Höfling, A. G. Truscott, and E. A. Ostrovskaya, Talbot Effect for Exciton Polaritons,** *Phys. Rev. Lett.* **117, 097403 (2016).**

8. **<u>Xuekai Ma</u>, Rodislav Driben, Boris A. Malomed, Torsten Meier, and Stefan Schumacher, Two-dimensional symbiotic solitons and vortices in binary condensates with attractive crossspecies interaction,** *Scientific Reports* **6, 34847 (2016).**

9. **<u>Xuekai Ma</u>, Oleg A. Egorov, and Stefan Schumacher, Creation and Manipulation of Stable Dark Solitons and Vortices in Microcavity Polariton Condensates,** *Phys. Rev. Lett.* **118, 157401 (2017).**

10. **<u>Xuekai Ma</u> and Stefan Schumacher, Vortex chain memory in polariton condensates,** *arXiv:1703.04378* **(2017).**

Conference contributions

1. *Information processing with topologically protected vortex memories in exciton-polariton condensates*, H. Sigurdsson, O. A. Egorov, <u>X. Ma</u>, I. A. Shelykh, and T. C. H. Liew, **META15 2015**, New York, USA.

2. *Dynamics of exciton-polariton condensates in semiconductor microcavities with periodic potentials*, <u>Xuekai Ma</u>, Stefan Schumacher, and Oleg Egorov, **DPG Spring Meetings 2016**, Regensburg, Germany.

3. *Nonlinear dynamics of nonequilibrium exciton-polaritons in a periodic potential*, M. V. Charukhchyan, I. Yu. Chestnov, A. P. Alodjants, <u>X. Ma</u>, and O. A. Egorov, **Saint Petersburg OPEN 2016**, Saint Petersburg, Russia.

4. *Manipulation of dark solitons and vortices of exciton-polariton condensates in semiconductor microcavities*, <u>Xuekai Ma</u>, Oleg Egorov, and Stefan Schumacher, **NOEKS 13 2016**, Dortmund, Germany.

5. *Talbot effect for quantum light-matter waves*, T. Gao, E. Estrecho, G. Li, O. A. Egorov, <u>X. Ma</u>, K. Winkler, M. Kamp, C. Schneider, S. Höfling, A. G. Truscott, E. A. Ostrovskaya, **APPC-AIP 2016**, Brisbane, Australia.

Short Curriculum Vitae

Personal Data

Name:	Xuekai Ma
Date of birth:	06.03.1986
Place of birth:	Hebei, China
Nationality:	Chinese
E-mail:	xuekai.ma@gmail.com
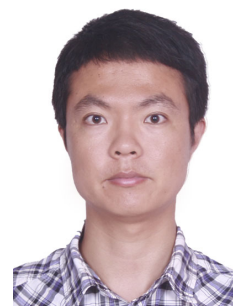
Academic Experience

2009.09-2012.06	Master student at South China Normal University, China (supervised by **Prof. Wei Hu**)
2012.10-2015.10	Scientific employee at Institute of Condensed Matter Theory and Solid State Optics (IFTO), Friedrich-Schiller-Universität Jena, Germany. (supervised by **Dr. Oleg Egorov** and **Prof. Falk Lederer**)
2015.11-present	Scientific employee at Department of Physics, Universiät Paderborn, Germany (supervised by **Prof. Stefan Schumacher**)
2017.04	Submission of PhD thesis

Education

2005.09-2009.06	Hebei Normal University, China B.S. Physics
2009.09-2012.06	South China Normal University, China M.S. Optics
2012.10-present	Friedrich-Schiller-Universität Jena and Universiät Paderborn, Germany Ph.D. Physics

Declaration

I hereby declare that this thesis has been composed and written completely by myself. The theoretical work is almost entirely my own work; the collaborative contributions have been indicated clearly and acknowledged. Due references have been provided on all supporting literatures and resources. This thesis contains no material that has been submitted previously, in whole or in part, for the award of any other academic degree or diploma or is being published elsewhere.

Paderborn, April 19, 2017

———————————————
Xuekai Ma

Bibliography

[1] J Frenkel. On the solid body model of heavy nuclei. *Phys. Z. Soviet Union*, 9:158, 1936.

[2] VM Agranovich. The influence of reabsorption upon the duration of the fluorescence of molecular crystals, 1957.

[3] Jack L Jewell, JP Harbison, Axel Scherer, YH Lee, and LT Florez. Vertical-cavity surface-emitting lasers: design, growth, fabrication, characterization. *IEEE Journal of Quantum Electronics*, 27(6):1332–1346, 1991.

[4] Vincenzo Savona, Carlo Piermarocchi, Antonio Quattropani, Paolo Schwendimann, and Francesco Tassone. Optical properties of microcavity polaritons. *Phase transitions*, 68(1):169–279, 1999.

[5] A Kavokin and G Malpuech. Cavity polaritons, thin films and nanostructures, vol. 32, 2003.

[6] A Kavokin, JJ Baumberg, G Malpuech, and FP Laussy. Microcavities oxford university press. *New York*, 2007.

[7] Benoit Deveaud. *The physics of semiconductor microcavities*. John Wiley & Sons, 2007.

[8] Claude Weisbuch, Mr Nishioka, A Ishikawa, and Y Arakawa. Observation of the coupled exciton-photon mode splitting in a semiconductor quantum microcavity. *Physical Review Letters*, 69(23):3314, 1992.

[9] Hui Deng, Gregor Weihs, David Snoke, Jacqueline Bloch, and Yoshihisa Yamamoto. Polariton lasing vs. photon lasing in a semiconductor microcavity. *Proceedings of the National Academy of Sciences*, 100(26):15318–15323, 2003.

[10] APD Love, DN Krizhanovskii, DM Whittaker, R Bouchekioua, D Sanvitto, S Al Rizeiqi, R Bradley, MS Skolnick, PR Eastham, R André, et al. Intrinsic decoherence mechanisms in the microcavity polariton condensate. *Physical review letters*, 101(6):067404, 2008.

[11] Esther Wertz, Lydie Ferrier, DD Solnyshkov, Robert Johne, Daniele Sanvitto, Aristide Lemaître, Isabelle Sagnes, Roger Grousson, Alexey V Kavokin, Pascale Senellart, et al. Spontaneous formation and optical manipulation of extended polariton condensates. *Nature physics*, 6(11):860–864, 2010.

[12] Bryan Nelsen, Gangqiang Liu, Mark Steger, David W Snoke, Ryan Balili, Ken West, and Loren Pfeiffer. Dissipationless flow and sharp threshold of a polariton condensate with long lifetime. *Physical Review X*, 3(4):041015, 2013.

[13] Mark Steger, Gangqiang Liu, Bryan Nelsen, Chitra Gautham, David W Snoke, Ryan Balili, Loren Pfeiffer, and Ken West. Long-range ballistic motion and coherent flow of long-lifetime polaritons. *Physical Review B*, 88(23):235314, 2013.

[14] Mark Steger, Chitra Gautham, David W Snoke, Loren Pfeiffer, and Ken West. Slow reflection and two-photon generation of microcavity exciton–polaritons. *Optica*, 2(1):1–5, 2015.

[15] Yongbao Sun, Patrick Wen, Yoseob Yoon, Gangqiang Liu, Mark Steger, Loren N Pfeiffer, Ken West, David W Snoke, and Keith A Nelson. Bose-einstein condensation of long-lifetime polaritons in thermal equilibrium. *Physical Review Letters*, 118(1):016602, 2017.

[16] Hui Deng, David Press, Stephan Götzinger, Glenn S Solomon, Rudolf Hey, Klaus H Ploog, and Yoshihisa Yamamoto. Quantum degenerate exciton-polaritons in thermal equilibrium. *Physical review letters*, 97(14):146402, 2006.

[17] Makoto Kuwata-Gonokami, Shin Inouye, Hidekatsu Suzuura, Masayuki Shirane, Ryo Shimano, Takao Someya, and Hiroyuki Sakaki. Parametric scattering of cavity polaritons. *Physical review letters*, 79(7):1341, 1997.

[18] Mi Saba, C Ciuti, J Bloch, V Thierry-Mieg, R André, Le Si Dang, S Kundermann, A Mura, G Bongiovanni, JL Staehli, et al. High-temperature ultrafast polariton parametric amplification in semiconductor microcavities. *Nature*, 414(6865):731–735, 2001.

[19] C Ciuti, P Schwendimann, and A Quattropani. Theory of polariton parametric interactions in semiconductor microcavities. *Semiconductor science and technology*, 18(10):S279, 2003.

[20] S Kundermann, M Saba, C Ciuti, T Guillet, U Oesterle, JL Staehli, and B Deveaud. Coherent control of polariton parametric scattering in semiconductor microcavities. *Physical review letters*, 91(10):107402, 2003.

[21] Carole Diederichs, Jérôme Tignon, Gregor Dasbach, Cristiano Ciuti, Aristide Lemaitre, Jacqueline Bloch, Ph Roussignol, and Claude Delalande. Parametric oscillation in vertical triple microcavities. *Nature*, 440(7086):904–907, 2006.

[22] Alessandro Tredicucci, Yong Chen, Vittorio Pellegrini, Marco Börger, and Franco Bassani. Optical bistability of semiconductor microcavities in the strong-coupling regime. *Physical Review A*, 54(4):3493, 1996.

[23] Augustin Baas, J Ph Karr, H Eleuch, and E Giacobino. Optical bistability in semiconductor microcavities. *Physical Review A*, 69(2):023809, 2004.

[24] NA Gippius, SG Tikhodeev, VD Kulakovskii, DN Krizhanovskii, and AI Tartakovskii. Nonlinear dynamics of polariton scattering in semiconductor microcavity: Bistability vs. stimulated scattering. *EPL (Europhysics Letters)*, 67(6):997, 2004.

[25] NA Gippius, IA Shelykh, DD Solnyshkov, SS Gavrilov, Yuri G Rubo, AV Kavokin, SG Tikhodeev, and G Malpuech. Polarization multistability of cavity polaritons. *Physical review letters*, 98(23):236401, 2007.

[26] Daniele Bajoni, Elizaveta Semenova, Aristide Lemaître, Sophie Bouchoule, Esther Wertz, Pascale Senellart, Sylvain Barbay, Robert Kuszelewicz, and Jacqueline Bloch. Optical bistability in a gaas-based polariton diode. *Physical review letters*, 101(26):266402, 2008.

[27] Iacopo Carusotto and Cristiano Ciuti. Probing microcavity polariton superfluidity through resonant rayleigh scattering. *Physical review letters*, 93(16):166401, 2004.

[28] Alberto Amo, Jérôme Lefrère, Simon Pigeon, Claire Adrados, Cristiano Ciuti, Iacopo Carusotto, Romuald Houdré, Elisabeth Giacobino, and Alberto Bramati. Superfluidity of polaritons in semiconductor microcavities. *Nature Physics*, 5(11):805–810, 2009.

[29] A Amo, D Sanvitto, FP Laussy, D Ballarini, E Del Valle, MD Martin, A Lemaitre, J Bloch, DN Krizhanovskii, MS Skolnick, et al. Collective fluid dynamics of a polariton condensate in a semiconductor microcavity. *Nature*, 457(7227):291–295, 2009.

[30] D Sanvitto, FM Marchetti, MH Szymańska, G Tosi, M Baudisch, FP Laussy, D-N Krizhanovskii, MS Skolnick, L Marrucci, A Lemaitre, et al. Persistent currents and quantized vortices in a polariton superfluid. *Nature Physics*, 6(7):527–533, 2010.

[31] FM Marchetti, MH Szymańska, C Tejedor, and DM Whittaker. Spontaneous and triggered vortices in polariton optical-parametric-oscillator superfluids. *Physical review letters*, 105(6):063902, 2010.

[32] Konstantinos G Lagoudakis, Francesco Manni, Barbara Pietka, Michiel Wouters, Timothy Chi Hin Liew, Vincenzo Savona, Alexey V Kavokin, Régis André, and Benoît Deveaud-Plédran. Probing the dynamics of spontaneous quantum vortices in polariton superfluids. *Physical review letters*, 106(11):115301, 2011.

[33] Simon Pigeon, Iacopo Carusotto, and Cristiano Ciuti. Hydrodynamic nucleation of vortices and solitons in a resonantly excited polariton superfluid. *Physical Review B*, 83(14):144513, 2011.

[34] G Tosi, G Christmann, NG Berloff, P Tsotsis, T Gao, Z Hatzopoulos, PG Savvidis, and JJ Baumberg. Geometrically locked vortex lattices in semiconductor quantum fluids. *Nature communications*, 3:1243, 2012.

[35] AV Yulin, OA Egorov, F Lederer, and DV Skryabin. Dark polariton solitons in semiconductor microcavities. *Physical Review A*, 78(6):061801, 2008.

[36] OA Egorov, Dmitry V Skryabin, AV Yulin, and F Lederer. Bright cavity polariton solitons. *Physical review letters*, 102(15):153904, 2009.

[37] OA Egorov, Andriy V Gorbach, F Lederer, and Dmitry V Skryabin. Two-dimensional localization of exciton polaritons in microcavities. *Physical review letters*, 105(7):073903, 2010.

[38] OA Egorov, Dmitry V Skryabin, and F Lederer. Polariton solitons due to saturation of the exciton-photon coupling. *Physical Review B*, 82(16):165326, 2010.

[39] Alberto Amo, S Pigeon, D Sanvitto, VG Sala, R Hivet, Iacopo Carusotto, F Pisanello, G Leménager, R Houdré, E Giacobino, et al. Polariton superfluids reveal quantum hydrodynamic solitons. *Science*, 332(6034):1167–1170, 2011.

[40] M Sich, DN Krizhanovskii, MS Skolnick, Andriy V Gorbach, Robin Hartley, Dmitry V Skryabin, EA Cerda-Méndez, K Biermann, R Hey, and PV Santos. Observation of bright polariton solitons in a semiconductor microcavity. *Nature photonics*, 6(1):50–55, 2012.

[41] R Hivet, H Flayac, DD Solnyshkov, D Tanese, T Boulier, D Andreoli, E Giacobino, J Bloch, A Bramati, G Malpuech, et al. Half-solitons in a polariton quantum fluid behave like magnetic monopoles. *Nature Physics*, 8(10):724–728, 2012.

[42] Akira Hasegawa. Optical solitons in fibers. In *Optical Solitons in Fibers*, pages 1–74. Springer, 1989.

[43] JS Aitchison, AM Weiner, Y Silberberg, MK Oliver, JL Jackel, DE Leaird, EM Vogel, and PWE Smith. Observation of spatial optical solitons in a nonlinear glass waveguide. *Optics letters*, 15(9):471–473, 1990.

[44] F Kh Abdullaev. *Optical solitons*. World Scientific, 1991.

[45] HS Eisenberg, Ya Silberberg, R Morandotti, AR Boyd, and JS Aitchison. Discrete spatial optical solitons in waveguide arrays. *Physical Review Letters*, 81(16):3383, 1998.

[46] Yuri S Kivshar and Govind Agrawal. *Optical solitons: from fibers to photonic crystals*. Academic press, 2003.

[47] Claudio Conti, Marco Peccianti, and Gaetano Assanto. Observation of optical spatial solitons in a highly nonlocal medium. *Physical review letters*, 92(11):113902, 2004.

[48] ZH Musslimani, Konstantinos G Makris, Ramy El-Ganainy, and Demetrios N Christodoulides. Optical solitons in p t periodic potentials. *Physical Review Letters*, 100(3):030402, 2008.

[49] Stefan Burger, K Bongs, S Dettmer, W Ertmer, K Sengstock, A Sanpera, GV Shlyapnikov, and M Lewenstein. Dark solitons in bose-einstein condensates. *Physical Review Letters*, 83(25):5198, 1999.

[50] Th Busch and JR Anglin. Motion of dark solitons in trapped bose-einstein condensates. *Physical Review Letters*, 84(11):2298, 2000.

[51] J Denschlag, JE Simsarian, DL Feder, Charles W Clark, LA Collins, J Cubizolles, Lu Deng, Edward W Hagley, K Helmerson, William P Reinhardt, et al. Generating solitons by phase engineering of a bose-einstein condensate. *Science*, 287(5450):97–101, 2000.

[52] Andrea Trombettoni and Augusto Smerzi. Discrete solitons and breathers with dilute bose-einstein condensates. *Physical Review Letters*, 86(11):2353, 2001.

[53] Kevin E Strecker, Guthrie B Partridge, Andrew G Truscott, and Randall G Hulet. Formation and propagation of matter-wave soliton trains. *Nature*, 417(6885):150–153, 2002.

[54] Hiroki Saito and Masahito Ueda. Dynamically stabilized bright solitons in a two-dimensional bose-einstein condensate. *Physical review letters*, 90(4):040403, 2003.

[55] ZX Liang, ZD Zhang, and WM Liu. Dynamics of a bright soliton in bose-einstein condensates with time-dependent atomic scattering length in an expulsive parabolic potential. *Physical review letters*, 94(5):050402, 2005.

[56] Steven A Kivelson, Daniel S Rokhsar, and James P Sethna. Topology of the resonating valence-bond state: Solitons and high-t c superconductivity. *Physical Review B*, 35(16):8865, 1987.

[57] PCE Stamp, L Forro, and C Ayache. Kosterlitz-thouless transition of fluxless solitons in superconducting y ba 2 cu 3 o 7- δ single crystals. *Physical Review B*, 38(4):2847, 1988.

[58] Y Tanaka. Soliton in two-band superconductor. *Physical review letters*, 88(1):017002, 2001.

[59] A Gurevich and VM Vinokur. Interband phase modes and nonequilibrium soliton structures in two-gap superconductors. *Physical review letters*, 90(4):047004, 2003.

[60] Arnol'd Markovich Kosevich, BA Ivanov, and AS Kovalev. Magnetic solitons. *Physics Reports*, 194(3-4):117–238, 1990.

[61] Reinhard Richter and IV Barashenkov. Two-dimensional solitons on the surface of magnetic fluids. *Physical review letters*, 94(18):184503, 2005.

[62] Norman J Zabusky and Martin D Kruskal. Interaction of" solitons" in a collisionless plasma and the recurrence of initial states. *Physical review letters*, 15(6):240, 1965.

[63] Derek A Tidman and Nicholas A Krall. *Shock waves in collisionless plasmas*. Wiley-Interscience New York, 1971.

[64] GO Ludwig, JL Ferreira, and Y Nakamura. Observation of ion-acoustic rarefaction solitons in a multicomponent plasma with negative ions. *Physical review letters*, 52(4):275, 1984.

[65] PK Kaw, A Sen, and T Katsouleas. Nonlinear 1d laser pulse solitons in a plasma. *Physical review letters*, 68(21):3172, 1992.

[66] Aleksandr Sergeevich Davydov. Solitons in molecular systems. In *Nonlinear and Turbulent Processes in Physics*, volume 1, page 731, 1984.

[67] PD Drummond, KV Kheruntsyan, and H He. Coherent molecular solitons in bose-einstein condensates. *Physical review letters*, 81(15):3055, 1998.

[68] Ying Wu and Xiaoxue Yang. Giant kerr nonlinearities and solitons in a crystal of molecular magnets. *Applied Physics Letters*, 91(9):094104, 2007.

[69] Albrecht Werner, Oleg A Egorov, and Falk Lederer. Exciton-polariton patterns in coherently pumped semiconductor microcavities. *Physical Review B*, 89(24):245307, 2014.

[70] Albrecht Werner, Oleg A Egorov, and Falk Lederer. Pseudospin dynamics of exciton-polariton patterns in a coherently driven semiconductor microcavity. *Physical Review B*, 90(16):165308, 2014.

[71] Hui Deng, Gregor Weihs, Charles Santori, Jacqueline Bloch, and Yoshihisa Yamamoto. Condensation of semiconductor microcavity exciton polaritons. *Science*, 298(5591):199–202, 2002.

[72] Jacek Kasprzak, M Richard, S Kundermann, A Baas, P Jeambrun, JMJ Keeling, FM Marchetti, MH Szymańska, R Andre, JL Staehli, et al. Bose–einstein condensation of exciton polaritons. *Nature*, 443(7110):409–414, 2006.

[73] R Balili, V Hartwell, D Snoke, L Pfeiffer, and K West. Bose-einstein condensation of microcavity polaritons in a trap. *Science*, 316(5827):1007–1010, 2007.

[74] Hui Deng, Hartmut Haug, and Yoshihisa Yamamoto. Exciton-polariton bose-einstein condensation. *Reviews of Modern Physics*, 82(2):1489, 2010.

[75] R Houdré, RP Stanley, U Oesterle, M Ilegems, and C Weisbuch. Room-temperature cavity polaritons in a semiconductor microcavity. *Physical Review B*, 49(23):16761, 1994.

[76] DG Lidzey, DDC Bradley, T Virgili, A Armitage, MS Skolnick, and S Walker. Room temperature polariton emission from strongly coupled organic semiconductor microcavities. *Physical review letters*, 82(16):3316, 1999.

[77] Guillaume Malpuech, Aldo Di Carlo, Alexey Kavokin, Jeremy J Baumberg, Marian Zamfirescu, and Paolo Lugli. Room-temperature polariton lasers based on gan microcavities. *Applied physics letters*, 81(3):412–414, 2002.

[78] S Christopoulos, G Baldassarri Höger Von Högersthal, AJD Grundy, PG Lagoudakis, AV Kavokin, JJ Baumberg, G Christmann, R Butté, E Feltin, J-F Carlin, et al. Room-temperature polariton lasing in semiconductor microcavities. *Physical review letters*, 98(12):126405, 2007.

[79] Gabriel Christmann, Raphaël Butté, Eric Feltin, Jean-François Carlin, and Nicolas Grandjean. Room temperature polariton lasing in a gan/ algan multiple quantum well microcavity. *Applied Physics Letters*, 93(5):051102, 2008.

[80] SI Tsintzos, NT Pelekanos, G Konstantinidis, Z Hatzopoulos, and PG Savvidis. A gaas polariton light-emitting diode operating near room temperature. *Nature*, 453(7193):372–375, 2008.

[81] JJ Baumberg, AV Kavokin, S Christopoulos, AJD Grundy, R Butté, G Christmann, DD Solnyshkov, G Malpuech, G Baldassarri Höger von Högersthal, El Feltin, et al. Spontaneous polarization buildup in a room-temperature polariton laser. *Physical review letters*, 101(13):136409, 2008.

[82] S Kéna-Cohen and SR Forrest. Room-temperature polariton lasing in an organic single-crystal microcavity. *Nature Photonics*, 4(6):371–375, 2010.

[83] Johannes D Plumhof, Thilo Stöferle, Lijian Mai, Ullrich Scherf, and Rainer F Mahrt. Room-temperature bose–einstein condensation of cavity exciton–polaritons in a polymer. *Nature materials*, 13(3):247–252, 2014.

[84] Thierry Guillet, Meletios Mexis, J Levrat, G Rossbach, Christelle Brimont, Thierry Bretagnon, Bernard Gil, R Butté, N Grandjean, Laurent Orosz, et al. Polariton lasing in a hybrid bulk zno microcavity. *Applied Physics Letters*, 99(16):161104, 2011.

[85] A Imamog, RJ Ram, S Pau, Y Yamamoto, et al. Nonequilibrium condensates and lasers without inversion: Exciton-polariton lasers. *Physical Review A*, 53(6):4250, 1996.

[86] Daniele Bajoni, Pascale Senellart, Esther Wertz, Isabelle Sagnes, Audrey Miard, Aristide Lemaître, and Jacqueline Bloch. Polariton laser using single micropillar gaas-gaalas semiconductor cavities. *Physical review letters*, 100(4):047401, 2008.

[87] Christian Schneider, Arash Rahimi-Iman, Na Young Kim, Julian Fischer, Ivan G Savenko, Matthias Amthor, Matthias Lermer, Adriana Wolf, Lukas Worschech, Vladimir D Kulakovskii, et al. An electrically pumped polariton laser. *Nature*, 497(7449):348–352, 2013.

[88] Tim Byrnes, Na Young Kim, and Yoshihisa Yamamoto. Exciton-polariton condensates. *Nature Physics*, 10(11):803–813, 2014.

[89] Elena A Ostrovskaya, Jasur Abdullaev, Anton S Desyatnikov, Michael D Fraser, and Yuri S Kivshar. Dissipative solitons and vortices in polariton bose-einstein condensates. *Physical Review A*, 86(1):013636, 2012.

[90] G Tosi, G Christmann, NG Berloff, P Tsotsis, T Gao, Z Hatzopoulos, PG Savvidis, and JJ Baumberg. Sculpting oscillators with light within a nonlinear quantum fluid. *Nature Physics*, 8(3):190–194, 2012.

[91] H Ohadi, RL Gregory, T Freegarde, YG Rubo, AV Kavokin, NG Berloff, and PG Lagoudakis. Nontrivial phase coupling in polariton multiplets. *Physical Review X*, 6(3):031032, 2016.

[92] Natalia G Berloff, Kirill Kalinin, Matteo Silva, Wolfgang Langbein, and Pavlos G Lagoudakis. Realizing the *xy* hamiltonian in polariton simulators. *arXiv preprint arXiv:1607.06065*, 2016.

[93] P Cristofolini, A Dreismann, G Christmann, G Franchetti, NG Berloff, P Tsotsis, Z Hatzopoulos, PG Savvidis, and JJ Baumberg. Optical superfluid phase transitions and trapping of polariton condensates. *Physical review letters*, 110(18):186403, 2013.

[94] A Askitopoulos, H Ohadi, AV Kavokin, Z Hatzopoulos, PG Savvidis, and PG Lagoudakis. Polariton condensation in an optically induced two-dimensional potential. *Physical Review B*, 88(4):041308, 2013.

[95] Johannes Schmutzler, Przemyslaw Lewandowski, Marc Aßmann, Dominik Niemietz, Stefan Schumacher, Martin Kamp, Christian Schneider, Sven Höfling, and Manfred Bayer. All-optical flow control of a polariton condensate using nonresonant excitation. *Physical Review B*, 91(19):195308, 2015.

[96] John Bardeen and MJ Stephen. Theory of the motion of vortices in superconductors. *Physical Review*, 140(4A):A1197, 1965.

[97] Kazunori Miyahara, Masashi Mukaida, and Kohji Hohkawa. Abrikosov vortex memory. *Applied physics letters*, 47(7):754–756, 1985.

[98] Gianni Blatter, Mikhail V Feigel'man, Vadim B Geshkenbein, Anatoly I Larkin, and Valerii M Vinokur. Vortices in high-temperature superconductors. *Reviews of Modern Physics*, 66(4):1125, 1994.

[99] K Harada, O Kamimura, H Kasai, T Matsuda, et al. Direct observation of vortex dynamics in superconducting films with regular arrays of defects. *Science*, 274(5290):1167, 1996.

[100] Dimitri Roditchev, Christophe Brun, Lise Serrier-Garcia, Juan Carlos Cuevas, Vagner Henrique Loiola Bessa, Milorad Vlado Milošević, François Debontridder, Vasily Stolyarov, and Tristan Cren. Direct observation of josephson vortex cores. *Nature Physics*, 11(4):332–337, 2015.

[101] T Shinjo, T Okuno, R Hassdorf, K Shigeto, and T Ono. Magnetic vortex core observation in circular dots of permalloy. *Science*, 289(5481):930–932, 2000.

[102] Bartel Van Waeyenberge, A Puzic, H Stoll, KW Chou, T Tyliszczak, R Hertel, M Fähnle, H Brückl, Karsten Rott, Günter Reiss, et al. Magnetic vortex core reversal by excitation with short bursts of an alternating field. *Nature*, 444(7118):461–464, 2006.

[103] VS Pribiag, IN Krivorotov, GD Fuchs, PM Braganca, O Ozatay, JC Sankey, DC Ralph, and RA Buhrman. Magnetic vortex oscillator driven by dc spin-polarized current. *Nature Physics*, 3(7):498–503, 2007.

[104] Russell P Cowburn. Spintronics: Change of direction. *Nature materials*, 6(4):255–256, 2007.

[105] Sang-Koog Kim, Ki-Suk Lee, Young-Sang Yu, and Youn-Seok Choi. Reliable low-power control of ultrafast vortex-core switching with the selectivity in an array of vortex states by in-plane circular-rotational magnetic fields and spin-polarized currents. *Applied Physics Letters*, 92(2):022509, 2008.

[106] R Dum, JI Cirac, M Lewenstein, and P Zoller. Creation of dark solitons and vortices in bose-einstein condensates. *Physical Review Letters*, 80(14):2972, 1998.

[107] Michael Robin Matthews, Brian P Anderson, PC Haljan, DS Hall, CE Wieman, and EA Cornell. Vortices in a bose-einstein condensate. *Physical Review Letters*, 83(13):2498, 1999.

[108] KW Madison, F Chevy, W Wohlleben, and Jl Dalibard. Vortex formation in a stirred bose-einstein condensate. *Physical Review Letters*, 84(5):806, 2000.

[109] Tomoya Isoshima, Mikio Nakahara, Tetsuo Ohmi, and Kazushige Machida. Creation of a persistent current and vortex in a bose-einstein condensate of alkali-metal atoms. *Physical Review A*, 61(6):063610, 2000.

[110] Chad N Weiler, Tyler W Neely, David R Scherer, Ashton S Bradley, Matthew J Davis, and Brian P Anderson. Spontaneous vortices in the formation of bose–einstein condensates. *Nature*, 455(7215):948–951, 2008.

[111] GA Swartzlander Jr, DR Andersen, JJ Regan, H Yin, and AE Kaplan. Spatial dark-soliton stripes and grids in self-defocusing materials. *Physical review letters*, 66(12):1583, 1991.

[112] Grover A Swartzlander Jr and Chiu T Law. Optical vortex solitons observed in kerr nonlinear media. *Physical Review Letters*, 69(17):2503, 1992.

[113] Yuri S Kivshar. Dark solitons in nonlinear optics. *IEEE Journal of Quantum Electronics*, 29(1):250–264, 1993.

[114] Tristram J Alexander, Andrey A Sukhorukov, and Yuri S Kivshar. Asymmetric vortex solitons in nonlinear periodic lattices. *Physical review letters*, 93(6):063901, 2004.

[115] Albert Ferrando, Mario Zacarés, Pedro Fernández de Córdoba, Daniele Binosi, and Juan A Monsoriu. Vortex solitons in photonic crystal fibers. *Optics express*, 12(5):817–822, 2004.

[116] Dahliyani Briedis, Dan E Petersen, Darran Edmundson, Wieslaw Krolikowski, and Ole Bang. Ring vortex solitons in nonlocal nonlinear media. *Optics Express*, 13(2):435–443, 2005.

[117] Alexander Dreischuh, Dragomir N Neshev, Dan E Petersen, Ole Bang, and Wieslaw Krolikowski. Observation of attraction between dark solitons. *Physical review letters*, 96(4):043901, 2006.

[118] KG Lagoudakis, T Ostatnickỳ, AV Kavokin, Yuri G Rubo, Régis André, and Benoit Deveaud-Plédran. Observation of half-quantum vortices in an exciton-polariton condensate. *Science*, 326(5955):974–976, 2009.

[119] Georgios Roumpos, Michael D Fraser, Andreas Löffler, Sven Höfling, Alfred Forchel, and Yoshihisa Yamamoto. Single vortex-antivortex pair in an exciton-polariton condensate. *Nature Physics*, 7(2):129–133, 2011.

[120] F Manni, KG Lagoudakis, TC H Liew, Régis André, V Savona, and B Deveaud. Dissociation dynamics of singly charged vortices into half-quantum vortex pairs. *Nature communications*, 3:1309, 2012.

[121] Jonathan Keeling and Natalia G Berloff. Spontaneous rotating vortex lattices in a pumped decaying condensate. *Physical review letters*, 100(25):250401, 2008.

[122] Konstantinos G Lagoudakis, Michiel Wouters, Maxime Richard, Augustin Baas, Iacopo Carusotto, Regis André, Le Si Dang, and B Deveaud-Plédran. Quantized vortices in an exciton–polariton condensate. *Nature Physics*, 4(9):706–710, 2008.

[123] H Sigurdsson, OA Egorov, X Ma, IA Shelykh, and TCH Liew. Information processing with topologically protected vortex memories in exciton-polariton condensates. *Physical Review B*, 90(1):014504, 2014.

[124] Robert Dall, Michael D Fraser, Anton S Desyatnikov, Guangyao Li, Sebastian Brodbeck, Martin Kamp, Christian Schneider, Sven Höfling, and Elena A Ostrovskaya. Creation of orbital angular momentum states with chiral polaritonic lenses. *Physical review letters*, 113(20):200404, 2014.

[125] Yan Xue and Michał Matuszewski. Creation and abrupt decay of a quasistationary dark soliton in a polariton condensate. *Physical Review Letters*, 112(21):216401, 2014.

[126] Lev A Smirnov, Daria A Smirnova, Elena A Ostrovskaya, and Yuri S Kivshar. Dynamics and stability of dark solitons in exciton-polariton condensates. *Physical Review B*, 89(23):235310, 2014.

[127] Kirstine Berg-Sørensen and Klaus Mølmer. Bose-einstein condensates in spatially periodic potentials. *Physical Review A*, 58(2):1480, 1998.

[128] Jared C Bronski, Lincoln D Carr, Bernard Deconinck, and J Nathan Kutz. Bose-einstein condensates in standing waves: The cubic nonlinear schrödinger equation with a periodic potential. *Physical Review Letters*, 86(8):1402, 2001.

[129] S Burger, FS Cataliotti, C Fort, F Minardi, M Inguscio, ML Chiofalo, and MP Tosi. Superfluid and dissipative dynamics of a bose-einstein condensate in a periodic optical potential. *Physical Review Letters*, 86(20):4447, 2001.

[130] Jared C Bronski, Lincoln D Carr, Bernard Deconinck, J Nathan Kutz, and Keith Promislow. Stability of repulsive bose-einstein condensates in a periodic potential. *Physical Review E*, 63(3):036612, 2001.

[131] M Machholm, CJ Pethick, and Henrik Smith. Band structure, elementary excitations, and stability of a bose-einstein condensate in a periodic potential. *Physical Review A*, 67(5):053613, 2003.

[132] R Idrissi Kaitouni, Ounsi El Daïf, Augustin Baas, Maxime Richard, Taofiq Paraiso, Pierre Lugan, Thierry Guillet, Francois Morier-Genoud, JD Ganiere, JL Staehli, et al. Engineering the spatial confinement of exciton polaritons in semiconductors. *Physical Review B*, 74(15):155311, 2006.

[133] CW Lai, NY Kim, S Utsunomiya, G Roumpos, H Deng, MD Fraser, T Byrnes, P Recher, N Kumada, T Fujisawa, et al. Coherent zero-state and π-state in an exciton–polariton condensate array. *Nature*, 450(7169):529–532, 2007.

[134] Na Young Kim, Kenichiro Kusudo, Andreas Löffler, Sven Höfling, Alfred Forchel, and Yoshihisa Yamamoto. Exciton–polariton condensates near the dirac point in a triangular lattice. *New Journal of Physics*, 15(3):035032, 2013.

[135] Na Young Kim, Kenichiro Kusudo, Congjun Wu, Naoyuki Masumoto, Andreas Löffler, Sven Höfling, Norio Kumada, Lukas Worschech, Alfred Forchel, and Yoshihisa Yamamoto. Dynamical d-wave condensation of exciton-polaritons in a two-dimensional square-lattice potential. *Nature Physics*, 7(9):681–686, 2011.

[136] EA Cerda-Méndez, DN Krizhanovskii, M Wouters, R Bradley, K Biermann, K Guda, R Hey, PV Santos, D Sarkar, and MS Skolnick. Polariton condensation in dynamic acoustic lattices. *Physical review letters*, 105(11):116402, 2010.

[137] EA Cerda-Méndez, D Sarkar, DN Krizhanovskii, SS Gavrilov, K Biermann, MS Skolnick, and PV Santos. Exciton-polariton gap solitons in two-dimensional lattices. *Physical review letters*, 111(14):146401, 2013.

[138] Thibaut Jacqmin, Iacopo Carusotto, Isabelle Sagnes, Marco Abbarchi, DD Solnyshkov, Guillaume Malpuech, Elisabeth Galopin, Aristide Lemaître, Jacqueline Bloch, and Alberto Amo. Direct observation of dirac cones and a flatband in a honeycomb lattice for polaritons. *Physical review letters*, 112(11):116402, 2014.

[139] Long Zhang, Wei Xie, Jian Wang, Alexander Poddubny, Jian Lu, Yinglei Wang, Jie Gu, Wenhui Liu, Dan Xu, Xuechu Shen, et al. Weak lasing in one-dimensional polariton superlattices. *Proceedings of the National Academy of Sciences*, 112(13):E1516–E1519, 2015.

[140] Karol Winkler, Julian Fischer, Anne Schade, Matthias Amthor, Robert Dall, Jonas Geßler, Monika Emmerling, Elena A Ostrovskaya, Martin Kamp, Christian Schneider, et al. A polariton condensate in a photonic crystal potential landscape. *New Journal of Physics*, 17(2):023001, 2015.

[141] Naoyuki Masumoto, Na Young Kim, Tim Byrnes, Kenichiro Kusudo, Andreas Löffler, Sven Höfling, Alfred Forchel, and Yoshihisa Yamamoto. Exciton–polariton condensates with flat bands in a two-dimensional kagome lattice. *New Journal of Physics*, 14(6):065002, 2012.

[142] D Tanese, H Flayac, D Solnyshkov, A Amo, A Lemaître, E Galopin, R Braive, P Senellart, I Sagnes, G Malpuech, et al. Polariton condensation in solitonic gap states in a one-dimensional periodic potential. *Nature communications*, 4:1749, 2013.

[143] EA Ostrovskaya, Jasur Abdullaev, MD Fraser, AS Desyatnikov, and Yu S Kivshar. Self-localization of polariton condensates in periodic potentials. *Physical review letters*, 110(17):170407, 2013.

[144] Scott E Pollack, D Dries, Mark Junker, YP Chen, TA Corcovilos, and RG Hulet. Extreme tunability of interactions in a li 7 bose-einstein condensate. *Physical Review Letters*, 102(9):090402, 2009.

[145] Cheng Chin, Rudolf Grimm, Paul Julienne, and Eite Tiesinga. Feshbach resonances in ultracold gases. *Reviews of Modern Physics*, 82(2):1225, 2010.

[146] Rekishu Yamazaki, Shintaro Taie, Seiji Sugawa, and Yoshiro Takahashi. Submicron spatial modulation of an interatomic interaction in a bose-einstein condensate. *Physical review letters*, 105(5):050405, 2010.

[147] Mi Yan, BJ DeSalvo, B Ramachandhran, H Pu, and TC Killian. Controlling condensate collapse and expansion with an optical feshbach resonance. *Physical review letters*, 110(12):123201, 2013.

[148] Peng Zhang, Pascal Naidon, and Masahito Ueda. Independent control of scattering lengths in multicomponent quantum gases. *Physical review letters*, 103(13):133202, 2009.

[149] L de Forges de Parny, Valy G Rousseau, and Tommaso Roscilde. Feshbach-stabilized insulator of bosons in optical lattices. *Physical review letters*, 114(19):195302, 2015.

[150] Victor M Perez-Garcia and Juan Belmonte Beitia. Symbiotic solitons in heteronuclear multicomponent bose-einstein condensates. *Physical Review A*, 72(3):033620, 2005.

[151] Sadhan K Adhikari. Bright solitons in coupled defocusing nls equation supported by coupling: application to bose–einstein condensation. *Physics Letters A*, 346(1):179–185, 2005.

[152] PG Lagoudakis, PG Savvidis, JJ Baumberg, DM Whittaker, PR Eastham, MS Skolnick, and JS Roberts. Stimulated spin dynamics of polaritons in semiconductor microcavities. *Physical Review B*, 65(16):161310, 2002.

[153] MD Martin, G Aichmayr, L Viña, and R André. Polarization control of the nonlinear emission of semiconductor microcavities. *Physical review letters*, 89(7):077402, 2002.

[154] KV Kavokin, IA Shelykh, AV Kavokin, Guillaume Malpuech, and Pierre Bigenwald. Quantum theory of spin dynamics of exciton-polaritons in microcavities. *Physical review letters*, 92(1):017401, 2004.

[155] Charles Leyder, Marco Romanelli, J Ph Karr, Elisabeth Giacobino, Tim CH Liew, Mikhail M Glazov, Alexey V Kavokin, Guillaume Malpuech, and Alberto Bramati. Observation of the optical spin hall effect. *Nature Physics*, 3(9):628–631, 2007.

[156] Elena Kammann, Timothy Chi Hin Liew, Hamid Ohadi, Pasquale Cilibrizzi, Panayiotis Tsotsis, Zacharias Hatzopoulos, Pavlos G Savvidis, Alexey V Kavokin, and Pavlos G Lagoudakis. Nonlinear optical spin hall effect and long-range spin transport in polariton lasers. *Physical review letters*, 109(3):036404, 2012.

[157] A Amo, TCH Liew, C Adrados, R Houdré, E Giacobino, AV Kavokin, and A Bramati. Exciton–polariton spin switches. *Nature Photonics*, 4(6):361–366, 2010.

[158] NH Kwong, R Takayama, I Rumyantsev, M Kuwata-Gonokami, and R Binder. Third-order exciton-correlation and nonlinear cavity-polariton effects in semiconductor microcavities. *Physical Review B*, 64(4):045316, 2001.

[159] S Schumacher, Nai-Hang Kwong, and Rudolf Binder. Influence of exciton-exciton correlations on the polarization characteristics of polariton amplification in semiconductor microcavities. *Physical Review B*, 76(24):245324, 2007.

[160] Naotomo Takemura, Stéphane Trebaol, Michiel Wouters, Marcia T Portella-Oberli, and Benoît Deveaud. Polaritonic feshbach resonance. *Nature Physics*, 10(7):500–504, 2014.

[161] Michiel Wouters and Iacopo Carusotto. Excitations in a nonequilibrium bose-einstein condensate of exciton polaritons. *Physical review letters*, 99(14):140402, 2007.

[162] Iacopo Carusotto and Cristiano Ciuti. Quantum fluids of light. *Reviews of Modern Physics*, 85(1):299, 2013.

[163] Pasquale Cilibrizzi, Helgi Sigurdsson, Tim CH Liew, Hamid Ohadi, Alexis Askitopoulos, Sebastian Brodbeck, Christian Schneider, Ivan A Shelykh, Sven Höfling, Janne Ruostekoski, et al. Half-skyrmion spin textures in polariton microcavities. *Physical Review B*, 94(4):045315, 2016.

[164] MH Luk, YC Tse, Nai-Hang Kwong, PT Leung, Przemyslaw Lewandowski, Rudolf Binder, and Stefan Schumacher. Transverse optical instability patterns in semiconductor microcavities: polariton scattering and low-intensity all-optical switching. *Physical Review B*, 87(20):205307, 2013.

[165] Stefan Schumacher, NH Kwong, R Binder, and Arthur L Smirl. Low intensity directional switching of light in semiconductor microcavities. *physica status solidi (RRL)-Rapid Research Letters*, 3(1):10–12, 2009.

[166] Andrew MC Dawes, Daniel J Gauthier, Stefan Schumacher, NH Kwong, R Binder, and Arthur L Smirl. Transverse optical patterns for ultra-low-light-level all-optical switching. *Laser & Photonics Reviews*, 4(2):221–243, 2010.

[167] R Takayama, NH Kwong, I Rumyantsev, M Kuwata-Gonokami, and R Binder. T-matrix analysis of biexcitonic correlations in the nonlinear optical response of semiconductor quantum wells. *The European Physical Journal B-Condensed Matter and Complex Systems*, 25(4):445–462, 2002.

[168] NH Kwong and R Binder. Green's function approach to the dynamics-controlled truncation formalism: Derivation of the χ (3) equations of motion. *Physical Review B*, 61(12):8341, 2000.

[169] TCH Liew, IA Shelykh, and G Malpuech. Polaritonic devices. *Physica E: Low-dimensional Systems and Nanostructures*, 43(9):1543–1568, 2011.

[170] JJ Hopfield. Theory of the contribution of excitons to the complex dielectric constant of crystals. *Physical Review*, 112(5):1555, 1958.

[171] K Winkler, OA Egorov, IG Savenko, X Ma, E Estrecho, T Gao, S Müller, M Kamp, TCH Liew, EA Ostrovskaya, et al. Collective state transitions of exciton-polaritons loaded into a periodic potential. *Physical Review B*, 93(12):121303, 2016.

[172] Hiroki Saito and Masahito Ueda. Intermittent implosion and pattern formation of trapped bose-einstein condensates with an attractive interaction. *Physical review letters*, 86(8):1406, 2001.

[173] UHTC Al Khawaja, HTC Stoof, RG Hulet, KE Strecker, and GB Partridge. Bright soliton trains of trapped bose-einstein condensates. *Physical review letters*, 89(20):200404, 2002.

[174] L Salasnich, A Parola, and L Reatto. Modulational instability and complex dynamics of confined matter-wave solitons. *Physical review letters*, 91(8):080405, 2003.

[175] LD Carr and J Brand. Spontaneous soliton formation and modulational instability in bose-einstein condensates. *Physical review letters*, 92(4):040401, 2004.

[176] Timothy Chi Hin Liew, OA Egorov, M Matuszewski, Oleksandr Kyriienko, X Ma, and EA Ostrovskaya. Instability-induced formation and nonequilibrium dynamics of phase defects in polariton condensates. *Physical Review B*, 91(8):085413, 2015.

[177] Bakhtiyor B Baizakov, Boris A Malomed, and Mario Salerno. Multidimensional solitons in periodic potentials. *EPL (Europhysics Letters)*, 63(5):642, 2003.

[178] Jianke Yang and Ziad H Musslimani. Fundamental and vortex solitons in a two-dimensional optical lattice. *Optics letters*, 28(21):2094–2096, 2003.

[179] Bakhtiyor B Baizakov, Boris A Malomed, and Mario Salerno. Multidimensional solitons in a low-dimensional periodic potential. *Physical Review A*, 70(5):053613, 2004.

[180] D Mihalache, D Mazilu, F Lederer, YV Kartashov, L-C Crasovan, and L Torner. Stable three-dimensional spatiotemporal solitons in a two-dimensional photonic lattice. *Physical Review E*, 70(5):055603, 2004.

[181] Yaroslav V Kartashov, Victor A Vysloukh, and Lluis Torner. Rotary solitons in bessel optical lattices. *Physical review letters*, 93(9):093904, 2004.

[182] Yaroslav V Kartashov, Victor A Vysloukh, and Lluis Torner. Stable ring-profile vortex solitons in bessel optical lattices. *Physical review letters*, 94(4):043902, 2005.

[183] Bakhtiyor B Baizakov, Boris A Malomed, and Mario Salerno. Matter-wave solitons in radially periodic potentials. *Physical Review E*, 74(6):066615, 2006.

[184] Rodislav Driben, Boris A Malomed, Arthur Gubeskys, and Joseph Zyss. Cubic-quintic solitons in the checkerboard potential. *Physical Review E*, 76(6):066604, 2007.

[185] Xuekai Ma, Oleg A Egorov, and Stefan Schumacher. Creation and manipulation of stable dark solitons and vortices in microcavity polariton condensates. *Physical Review Letters*, 118(15):157401, 2017.

[186] L Dominici, M Petrov, M Matuszewski, D Ballarini, M De Giorgi, D Colas, E Cancellieri, B Silva Fernández, A Bramati, G Gigli, et al. Real-space collapse of a polariton condensate. *arXiv preprint arXiv:1309.3083*, 2013.

[187] Manjun Ma, R Carretero-González, PG Kevrekidis, DJ Frantzeskakis, and BA Malomed. Controlling the transverse instability of dark solitons and nucleation of vortices by a potential barrier. *Physical Review A*, 82(2):023621, 2010.

[188] Francesco Manni, Konstantinos G Lagoudakis, Timothy CH Liew, Régis André, and Benoît Deveaud-Plédran. Spontaneous pattern formation in a polariton condensate. *Physical review letters*, 107(10):106401, 2011.

[189] Xuekai Ma, Ulf Peschel, and Oleg A Egorov. Incoherent control of topological charges in nonequilibrium polariton condensates. *Physical Review B*, 93(3):035315, 2016.

[190] Alexis Askitopoulos, Timothy Chi Hin Liew, Hamid Ohadi, Z Hatzopoulos, PG Savvidis, and PG Lagoudakis. Robust platform for engineering pure-quantum-state transitions in polariton condensates. *Physical Review B*, 92(3):035305, 2015.

[191] Xuekai Ma and Stefan Schumacher. Vortex chain memory in polariton condensates. *arXiv preprint arXiv:1703.04378*, 2017.

[192] X Ma, I Yu Chestnov, MV Charukhchyan, AP Alodjants, and OA Egorov. Oscillatory dynamics of nonequilibrium dissipative exciton-polariton condensates in weak-contrast lattices. *Physical Review B*, 91(21):214301, 2015.

[193] Kestutis Staliunas, Ramon Herrero, and Germán J de Valcárcel. Subdiffractive band-edge solitons in bose-einstein condensates in periodic potentials. *Physical Review E*, 73(6):065603, 2006.

[194] OA Egorov, F Lederer, and K Staliunas. Theory of bloch cavity solitons. *Physical Review A*, 82(4):043830, 2010.

[195] DN Krizhanovskii, EA Cerda-Méndez, S Gavrilov, D Sarkar, K Guda, R Bradley, PV Santos, R Hey, K Biermann, M Sich, et al. Effect of polariton-polariton interactions on the excitation spectrum of a nonequilibrium condensate in a periodic potential. *Physical Review B*, 87(15):155423, 2013.

[196] OA Egorov and F Lederer. Lattice-cavity solitons in a degenerate optical parametric oscillator. *Physical Review A*, 76(5):053816, 2007.

[197] KG Lagoudakis, B Pietka, M Wouters, Régis André, and Benoit Deveaud-Plédran. Coherent oscillations in an exciton-polariton josephson junction. *Physical review letters*, 105(12):120403, 2010.

[198] Stephen M Jensen. The nonlinear coherent coupler. *IEEE Transactions on Microwave Theory and Techniques*, 30(10):1568–1571, 1982.

[199] Tingge Gao, Eliezer Estrecho, G Li, OA Egorov, X Ma, K Winkler, M Kamp, C Schneider, Sven Hoefling, AG Truscott, et al. Talbot effect for exciton polaritons. *Physical Review Letters*, 117(9):097403, 2016.

[200] AV Yulin, I Yu Chestnov, X Ma, S Schumacher, U Peschel, and OA Egorov. Dynamics of exciton-polaritons in discrete lattices under incoherent localized pumping. *Physical Review B*, 94(5):054312, 2016.

[201] Xuekai Ma, Rodislav Driben, Boris A Malomed, Torsten Meier, and Stefan Schumacher. Two-dimensional symbiotic solitons and vortices in binary condensates with attractive cross-species interaction. *Scientific Reports*, 6, 2016.